MEMS-Based Thermal and Mass-Transport Control for Microfluidic Biochemical Reagent Mixing and 2-D Gas Chromatography

by

Sung Jin Kim

A dissertation submitted in partial fulfillment
of the requirements for the degree of
Doctor of Philosophy
(Mechanical Engineering)
in The University of Michigan
2010

Doctoral Committee:

Associate Professor Katsuo Kurabayashi, Chair

Professor Edward T. Zellers

Assistant Professor Kevin Patrick Pipe

Assistant Professor Pramod Sangi Reddy

To my family

ACKNOWLEDGEMENTS

It is with many supports and friendships that helped me in reaching this point. Each of the following individuals listed have helped me learn and grow by inspiring me through at least some parts of my PhD life.

First of all, I would like to thank my advisor Prof. Katsuo Kurabayashi for offering me the great opportunity and the environment to create this thesis work. He always encouraged me and was generous even at my faults. Also, I would like to thank my committee members — Prof. Edward Zellers, Prof. Kevin Pipe, and Prof. Pramod Reddy — for their advice and help in finishing this PhD thesis.

Many thanks should go to Prof. Mark Burns, Prof. Nikos Chronis, Prof Kensall Wise, and Dr. Bruce Block for providing the equipment for performing many experiments presented in this thesis work. I am also grateful to Fang Wang in Prof. Mark Burns' group, and Trushal Choski and Anurag Tripathi in Prof. Nikos Chronis' group for their generous help in my experiments.

A special thank you should go to past and current group members in our lab for their friendship and support: Steven Truxel, Steve Schrader, Jung Hwan Seo, Nien-Tsu (Joe) Huang, and Matthew Stites.

Also, I can't thank enough the members in Friday Tennis Club. I was always looking forward to be on Friday just to play tennis with them. My life here would be very boring without them. Especially, I would like to thank Youngshin Kim, Chulhun Park, Sungick

Kim, Kyeongmin Kim, and Irully Jeong for their small and great help in managing the club.

In no particular order, I wish to thank many people whom I have met here at the University of Michigan for generating many good memories that I will be keeping for the rest of my life: Joosup Lim, Kukhyun Ahn, Bongsu Han, Jeong-Hoon Ryu, Chung-Ho Rhee, Changsun Ahn, Dongkyoung Lee, Joongdon Cho, Sangmin Lee, Sungmin Lee, Kyungho Ahn, Seungcheol Yang, Seungcheol Lee, Gisuk Hwang, Dahye Min, Jonggirl Ok, Seunghwan Lee, Juil Yum, Yongseob Lim, Daewoo Park and Gwangjae Lee.

Also, my very good old friends and seniors since SNU, KAIST, or ETRI days whose inspirations and friendship have kept me going until this day: Chun Kyu Kwon, Yongjin Seong, Kyrung Lee, Sang-Hee Yoon, Young-Ho Seo, Hasik Yang, Kyuwon Kim, and Yongtaik Lim.

With tremendous gratitude, I would like to acknowledge my family for their love and support. You have always been there for me and believed me. Without your support and encouragement, I would not be able to venture this far.

The greatest thing that happened here is to have met my wife, Yoenju Park. I have to thank you for your love and for always being there for me. Your smile has always encouraged me!

TABLE OF CONTENTS

LIST OF FIGURES

LIST OF TABLES

LIST OF APPENDICES

ABSTRACT

This research demonstrates the use of microelectromechanical systems (MEMS) technology to control microscale heat and mass transfer for lab-on-a-chip biochemical assays and the analysis of complex vapor mixtures. Toward this goal, we have developed two microdevices, namely (1) a micromixer and (2) a microthermal modulator. The micromixer uses natural convection to greatly simplify the micromixing process in a microfluidic network, whereas the microthermal modulator utilizes forced convection to manipulate vapor samples in a fast, low-power consuming manner within a comprehensive 2-D gas chromatography system.

In a microfluidic network, micromixing is a crucial step for biochemical analysis. A critical challenge is that the microfluidic systems need numerous chambers and channels not only for mixing but also for biochemical reactions and detections. Thus, a simple and compatible design of the micromixer element for the system is essential. Here, we demonstrate a simple, yet effective, scheme that enables micromixing and biochemical reaction in a single chamber without using any mechanical components. We accomplish this process by using natural convection in conjunction with two alternating heaters for micromixing. As a model application, we demonstrate PCR and its reagent mixing in a single microfluidic chamber. Our results will significantly simplify the micromixing and subsequent biochemical reactions.

In comprehensive two-dimensional gas chromatography (GC×GC), a modulator is placed at the juncture between two separation columns to focus and re-inject eluting mixture components, thereby enhancing the resolution and the sensitivity of the analysis. Here, we present the design, fabrication, thermal operation, and initial testing of a two-stage microscale thermal modulator (μTM). The μTM contains two sequential serpentine Pyrex-on-Si microchannels (stages) that cryogenically trap analytes eluting from the first-dimension column and thermally inject them into the second-dimension column in a rapid, programmable manner with low thermal crosstalk between the two stages. A lumped heat transfer model is used to analyze the device design with respect to the rates of heating and cooling, power dissipation, and inter-stage thermal. Preliminary tests using a conventional capillary column interfaced to the μTM demonstrate the modulation of a mixture of alkanes.

CHAPTER I

INTRODUCTION

1.1 Background in Microscale Thermal Control

Scaling effects are critically important for heat transfer phenomena in microelectromechanical systems (MEMS) and have received a significant amount of attention from the MEMS research community [1]. The small size of MEMS devices enables fast thermal response: when we define the characteristic length as L, the rate of heat transfer ($\dot{E}_{\text{trans}}$) scales with the surface area (L^2) while the rate of heat storage ($\dot{E}_{\text{storage}}$) scales with the volume (L^3) [2]. Thus, the ratio $\dot{E}_{\text{trans}}$ / $\dot{E}_{\text{storage}}$ is inversely proportional to L, i.e. $\dot{E}_{\text{trans}}$ / $\dot{E}_{\text{storage}} \propto L^{-1}$. As a result, the significance of scaling issues becomes evident as the length scale of the components shrinks to microns with heat transfer dominating over thermal energy storage. This characteristic leads to small time constants for heat and mass transfer with small thermal mass, making thermal MEMS devices highly advantageous.

Similar to the macroscale devices, heat transfer in MEMS has three modes: (1) conduction, where heat transfer occurs across a stationary medium or an interface such as solids and narrow length scales of fluids; (2) convection, where heat transfer occurs between a surface and a moving fluid; and (3) radiation, where surfaces emit thermal

energy in the form of electromagnetic waves. Although radiation is important in extremely high temperature or electromagnetic wave applications that require no media, it is not within the scope of this study.

When we design thermal MEMS devices for biological and chemical applications, both conduction and convection should be carefully considered. Conduction is of particular importance as heat is generated solid MEMS devices and is transferred to biochemical solutions inside these devices. Thus, sophisticated controls of conduction mode in thermal MEMS devices are necessary for manipulating biological and chemical solutions using heat transfer. Operation of these devices requires the following three conditions: (1) high heating and cooling rates, (2) good thermal isolation from the environment, and (3) uniform temperature distributions at a desired region.

Although thermal MEMS devices have high surface-to-volume ratios and relatively small volumes, the devices may fail to achieve a target performance when the three conditions are not fully met. The three conditions in the conduction mode, however, are closely related and adjusting the parameters is nontrivial. For high heating and cooling rates, it is necessary to have good thermal isolation from the heat sources or sinks proximal to a thermal element because of the thermal mass of such sources. Thermal isolation to remove such sources close to a thermal element is often achieved through optimal device design and proper selection of materials. Thermally isolated suspended microsturctures can be constructed out of single-crystal silicon by bulk micromachining of a silicon substrate from its front or back side, or alternatively by surface micromachining of a thin film sacrificial layer from underneath the thermal element in conjunction with selection and combination of materials that have proper thermal

conductivities. For uniform temperature distributions, selection of a material that has high thermal conductivity is essential. However, this selection often contradicts with the need for thermal isolation between microstructures and adds complexities and costs to the thermal management of the device.

A representative process that simultaneously requires fast thermal response, isolation, and uniformity is polymerase chain reaction (PCR), which is a DNA amplification process. The PCR process involves three thermal steps in each cycle, typically 95°C for denaturation of double-stranded DNA molecules, 50–60°C for annealing, and 72°C for extension to form a new set of double-stranded molecules. The number of replicated DNA strands is greatly amplified with 20–40 cycles per reaction. Because the transient response time between the sequential thermal steps is long in macro devices, MEMS devices for the PCR application focused on reducing the transient response time [3-5]. For achieving the fast transient response, thermal isolation from a bulk silicon substrate, which acts as a heat sink is required. This high thermal isolation results in non-uniform temperature inside the reaction region when the device is not properly designed. However, the reaction region needs to be maintained at high temperature uniformity for a good yield in the PCR process; the polymerase enzyme, primer annealing, and denaturation of DNA only work within a correct temperature range.

In the convection mode, the heat transfer mechanism is based on conduction from a heating surface into a fluid layer adjacent to it. The inherently high surface-to-volume ratio of thermal MEMS devices provides advantages for heat exchange and mass transport due to convection. The convection mode can be classified into (1) natural convection and (2) forced convection. When fluid motion is caused by buoyancy

resulting from a temperature gradient in a fluid, the process is termed natural convection. In contrast, the process is called forced convection when fluid motion caused by an external means such as a pump, during heat exchange.

In this study, we use conduction heat-transfer to control natural and forced convection in two thermal MEMS devices. Micromixer controls natural convection for microfludic mixing, and microthermal modulator regulates forced convection for modulating vapor species. The applications of micromixer and microthermal modulator are for clinical diagnosis and comprehensive 2-D gas chromatography, respectively.

1.2 Motivation for Research

1.2.1 Micromixer

The development of rapid clinical diagnostic techniques in a portable, low-cost format is an active research area [6]. Employing integrated analysis systems based on MEMS technology is a promising approach for achieving automated sample preparation and detection for clinical laboratories or point-of-care settings. A critical challenge is that the system needs numerous chambers and channels not only for the detection of target DNA and proteins but also for sample-preparation processes such as cell lysis, DNA extraction and PCR, protein purification and concentration. These chambers and channels form sample and reagent storage reservoirs, microfluidic controlling valves, micromixers, and biochemical reaction sites. Thus, employing a simple and compatible design for each component is crucial to maintain the system less complex. As for

micromixing, however, conventional mixers employ complex geometries. This makes these devices cumbersome and even incompatible for routine use and system integration.

Natural convection offers an attractive way to overcome the limitation of conventional micromixing schemes. By applying a temperature gradient across an appropriately designed reactor geometry, a continuous circulatory flow can be initiated for repeated transport of solutions. This approach is highly advantageous because the need for the complex geometry is eliminated, which greatly simplifies the device design. Furthermore, many biochemical reactions require heating; thus micromixing and the reaction can be achieved using a common temperature controlling structure in a single chamber. Despite this promise, the development of a natural convection-driven mixer has been limited because convection by buoyancy is weak in general and shows relatively simple flow trajectories, not enabling efficient mixing inside the chamber. A new device for natural convection-based micromixing is developed in this thesis work.

1.2.2 Microthermal modulator

The National Aeronautics and Space Administration (NASA) astrobiology program has a goal to search and to classify organic compounds on extraterrestrial bodies within the solar system. When coupled with the requirement for separation of organics generated from a spacecraft and the need to distinguish biotic and antibiotic synthesis, organic classification is a formidable task. Comprehensive two-dimensional gas chromatography (GC×GC) can be a powerful analytical tool for separating the complex mixture of volatile organic compounds [7]. The system uses two serial columns to efficiently separate organic compounds. A critical component at the interface between

the two columns is a thermal modulator. A thermal modulator increases the amplitude of the chemical signal and facilitates its transmission through the second column of the system, similar to the way that a frequency modulator transmits radio waves.

However, conventional thermal modulators targeting bench-top applications use high electrical power for heating and a large amount of cryogenic materials for cooling, which makes them unsuitable for integration in a spacecraft. Moreover, they occupy a relatively large space. Because of the limited resources in a spacecraft, a more desirable thermal modulator would use less power for heating, require no coolants for cooling, and be compact in size, but would not sacrifice fast thermal response.

When we use a MEMS-based thermal modulator with a proper thermal design, we can implement low power heating because of the small thermal mass. Moreover, when used with a solid state thermoelectric cooler, the thermal modulator can be cooled with a relatively low power without using coolants. This thesis describes a new MEMS device that overcomes the aforementioned limitations of conventional thermal modulators for use in an environment of limited resources that meets the needs of the NASA astrobiology program mission for an analyzer of complex mixtures of volatile organic compounds.

1.3 Thesis Objectives

This research had four main goals motivated by the technological promise that thermal MEMS devices hold and by the need to address shortcomings of existing technologies for (1) microfluidic mixing and (2) gas chromatographic thermal modulation.

In our microfluidic mixing study, the first objective was to develop a scheme for using natural convection for efficient micromixing. The development of this scheme is the initial step towards simplifying microfluidic networks for micromixing and biochemical reactions. The second objective was to achieve micromixing and biochemical reaction in a single microfluidic chamber; here, we perform polymerase chain reaction (PCR) as our model application of biochemical reaction. In our gas chromatographic thermal modulation study, the first objective was to implement a MEMS thermal modulator that requires low power for heating and no coolants for cooling, without sacrificing the speed of thermal response. The second objective was to demonstrate the modulation of the mass transport of organic vapor species carried by a convective flow of an inert gas using the MEMS device.

1.4 Thesis Outline

This thesis study addressing the aforementioned research objectives comprises four subsequent technical chapters. The outline of this thesis is summarized as follows:

Chapter II – Review of Related Studies: This chapter reviews other research related to the project and includes work that provides a foundation for this project as well as a summary of competing technologies with similar applications. The review is divided into two main categories: (1) microfluidic mixers and (2) microthermal modulators. These two categories cover the microscale thermal control using our MEMS devices for

applications in a microfluidic network and 2-D comprehensive gas chromatography, respectively.

Chapter III – Micromixer: This chapter demonstrates a simple, yet effective, scheme that enables micromixing and a biochemical reaction in a single microfluidic chamber. This process is accomplished by using natural convection in conjunction with alternating heating of two heaters for efficient micromixing. As a model application, we demonstrate micromixing and subsequent PCR for an influenza viral DNA fragment. This process is achieved on a platform of a microfluidic cartridge and a microfabricated heating-instrument with a fast thermal response. Also, fabrication process and experimental methods are described in detail.

Chapter IV – Micro Thermal Modulator: This chapter presents the design, fabrication, thermal operation, and initial testing of a two-stage microscale thermal modulator. The heating and cooling processes are achieved by integrated resistive microheaters and a solid-state thermoelectric cooler placed within a few tens of micrometers of the device. For the heating-cooling of the device, experimental methods and device structures are presented in detail. Also, a lumped heat transfer model is used to analyze the device design with respect to the rates of heating and cooling, power dissipation, and inter-stage thermal crosstalk as a function of the Pyrex-membrane thickness, air-gap depth, and stage separation distance. Experimental results are compared and analyzed with theoretical values. Finally, forced convection process is shown in the context of the application in two-dimensional gas chromatography. The result demonstrates the vapor-modulation capability of the μTM using a mixture of alkanes.

Chapter V – Conclusions and Future Work: The final chapter summarizes the impact of the presented research and discusses future potential research using the micromixer and the μTM. The potential work using the micromixer includes (1) an integrated DNA analysis system that requires cell lysis, DNA hybridization system as well as PCR, and (2) biosynthesis. The future work in μTM is extended to two branches: (1) in-depth study of the separation of volatile organic compounds using our μTM and (2) integration of our μTM into a micro gas chromatography system.

CHAPTER II

REVIEW OF RELATED STUDIES

This chapter reviews previous studies related to this thesis research. These studies give insight into the motivations and applications of our research as well as an overview of competing technologies. Our work aims to make impact on (1) microfluidic networks for biochemical applications by using a natural convection-driven micromixer that implements mixing and biochemical reaction in a single chamber and (2) two-dimensional gas chromatography for separating volatile organic compounds (VOCs) by using a microthermal modulator.

2.1 Micromixer

In the process of shrinking laboratory instrumentation using microfluidics (i.e. developing microfluidic lab-on-a-chip technologies), some significant physical phenomena affecting conventional chemical processes are observed. One of these phenomena originates from small channel dimensions that make the flow laminar. The slow diffusion of biological molecules in laminar flow makes microfluidic mixing very challenging. This problem was first reported by Yager's group [8] while observing

laminar flow and characterizing diffusion in a microchannel. Yager and coworkers took advantage of the differences in diffusion rates between large and small molecules in two confluent streams and used these differences to perform simple filtration and extraction on a chip. Simultaneously, they used diffusive mixing between the two confluent streams to quantify biochemical reaction. They soon realized that complete mixing by simple diffusion along a microchannel would be unexpectedly slow, resulting in the requirement of either an extremely low flow rate or a prohibitively long microchannel.

Rapid homogeneous mixing becomes increasingly important when the time scale of mixing is larger than or of the same order as the time scale of chemical reaction in a microfluidic system. Many biochemical applications such as immunoassays, DNA hybridization, PCR, and general molecular interactions in a cell require rapid mixing. However, the diffusion processes in biochemical solutions used in these techniques is often slow relative to biochemical reaction processes. For example, the diffusion time of a globular protein ($D = 8\times10^{-5}$ mm^2/s) across the chamber of width w = 1 mm is calculated as $t = w^2/(2D)$ = 104 min, and the diffusion time of a 4 kbp DNA ($D = 2\times10^{-4}$ mm^2/s) is 83 min. In contrast, a biochemical reaction such as PCR is usually less than one hour in microfluidic devices. To overcome the shortcoming of this relatively slow diffusion process, extensive studies have been done for a decade to enhance mixing at the micrometer scale [9].

In most cases, micromixers can be classified as either an active or a passive type. Passive micromixers require no external energy source except for driving fluid flow, whereas active micromixers need external energies for both mixing and driving fluid flow. Passive micromixers use engineered channel geometries to mix continuous flows, where

the channel geometries help to increase the interfacial area between the solutions to be mixed. Manz's group [10] presented a continuous flow mixer based on separating a liquid into narrower channels and reunifying the channels to allow for faster molecular diffusion. Other passive lamination-based micromixers, where a fluid is split into parallel or serial flows, have also been demonstrated [11-13]. Others have created plumes to increase the surface area for mixing [14]. In addition, chaotic mixing by geometrical perturbation has been proposed, where helical flow is perturbed by a herringbone structure on the bottom of the channel [15] or by a 3-D serpentine channel [16].

Active micromixers include a simple channel system where side channels introduce pressure perturbations or time-dependent dielectrophoretic forces [17]. Kim's group presented a mixer based on merged droplets which are moved by electrowetting on dielectric. In this device, the interface between liquids is distorted by a velocity gradient in the droplet, which finally results in mixing of the two droplets [18]. Acoustic transducers have also been used to produce chaotic advection [19]. Santiago's group used electrokinetic instability to stir fluid stream with the rapid stretching and folding of pathlines [20]. It is commonly perceived that active micromixers are more disadvantageous than the passive micromixers in that it is more difficult to fabricate, operate, and integrate.

A desirable micromixing process in a microfluidic network is simple and compatible with system integration while maintaining the ability to homogenize different solutions in a proper time scale prior to biochemical reactions. Numerous studies [9], however, focus solely on the performance of micromixing and have paid relatively little attention to achieving simplicity for the topological structure, fabrication process, and off-chip setup

of their micromixers. Many of the micromixing processes in these studies were based on a passive mechanism where inherent stationary structures of microchannels were used. Although there have been significant advances in passive-mixer designs, they still have drawbacks when it comes to their integration in a microfluidic network. One passive mixer design (Figure 2.1) incorporates a microchannel with groove-patterns to enhance efficient micromixing [15]. Due to its 3-D shape, the construction of the mixer needs relatively laborious two-step microfabrication for the microchannel.

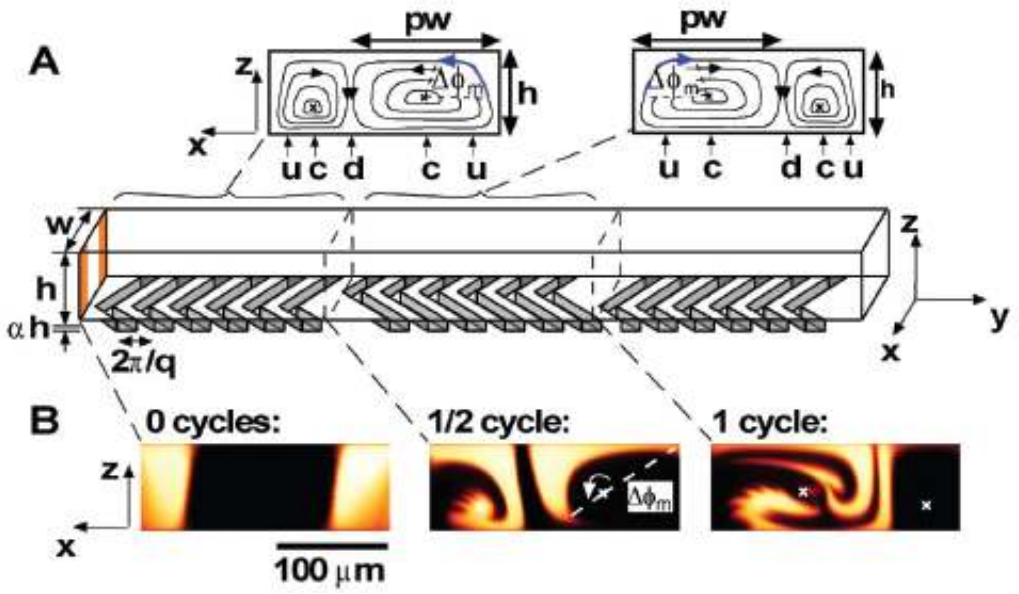

Figure 2.1. Staggered herringbone mixer. **(A)** Schematic diagram of one-and-a-half cycles of the micomixer. **(B)** Confocal micrographs showing cross sections of the channel [15].

In another design (Figure 2.2), a curved microchannel with a greatly simple 2-D shape harnessed micromixing [21]. Although the mixing scheme was elegant, the process turned out to be only effective at a relatively high Reynolds number of ~10. Moreover, these passive methods, including even those using simple micromixers [22], could not function without external pumps, often resulting in an enormous system volume especially when the micromixers are integrated in a microfluidic network. Also, they often require separate chambers for subsequent biochemical reactions, thus adding more complexity to the microfluidic network. For portable or point-of-care testing devices [23], a simple design is essential.

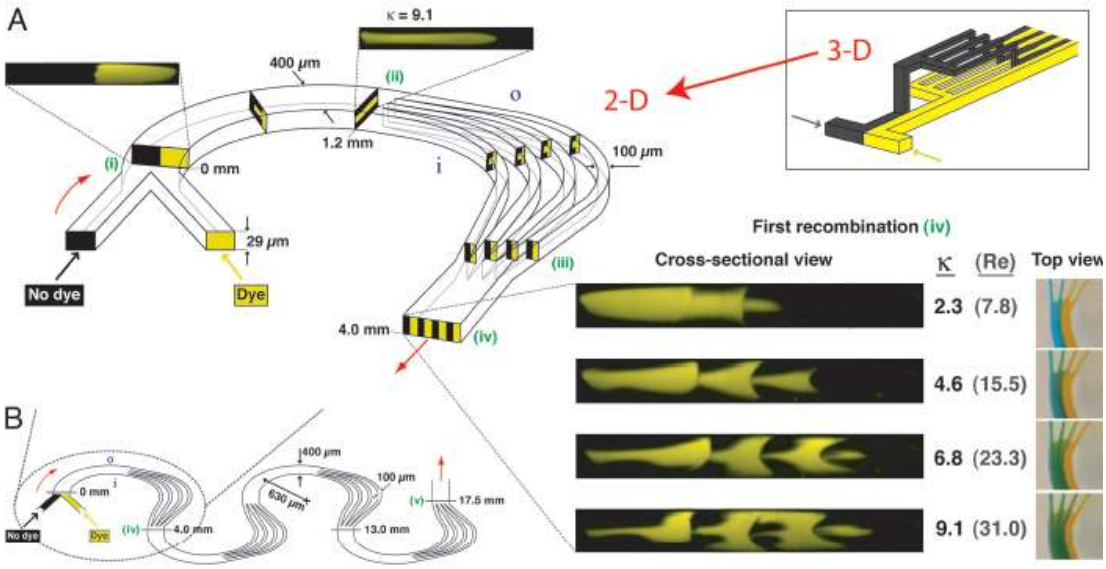

Figure 2.2. Multivortex micromixer. **(A)** Planar 2-D geometry capable of using centrifugal effects and multiple laminations. **(B)** Schematic of microchannel incorporating a series of successive mixing elements [21].

A few studies demonstrated integration of micromixers in a microfluidic network. However, these micromixers typically had limited performance. To compare mixing performance, we define a required mixing time to mix one microliter of solution (s/μL). For instance, a fully-integrated system for the DNA purification [23] used a rotary micromixer incorporating three peristaltic valves, but the mixing took several minutes even for one nanoliter sample volume (Figure 2.3). Another example is a cell-

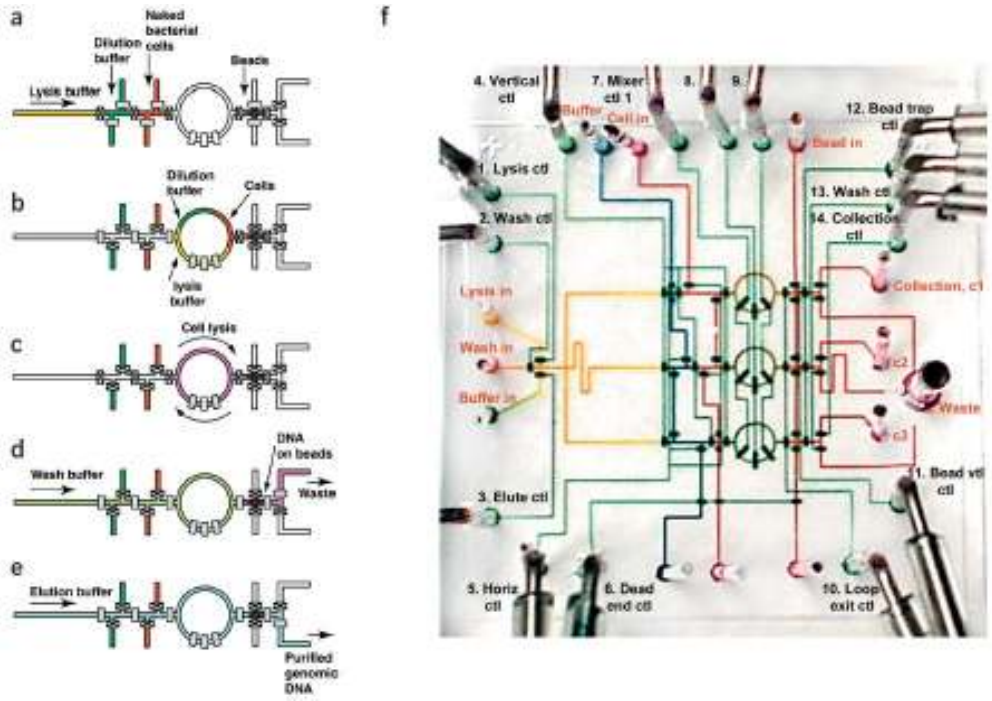

Figure 2.3. DNA purification chip and schematic diagram of DNA isolation process (Open valve, rectangle; closed valve, x in rectangle). **(a)** Introduction of Bacterial cell culture and buffers. **(b)** Micromixing of cell sample, dilution buffer, and lysis buffer. **(c)** Completion of micromixing and subsequent cell lysis. **(d)** Washing and capturing of DNA using affinity column. **(e)** Recovery of DNA using elution buffer. **(f)** Integrated bioprocessor chip with parallel architecture [23].

culture system [24] that used versatile Braille pins for micromixing, pumping, and valving; although the mixing rate was not explicitly reported, the maximum pumping rate of a solution was approximately 0.6 μL/min, meaning that mixing performance is > 100 s/μL. Even when a passive mixer with 3-D groove-patterns [15] was used in a DNA hybridization system (Figure 2.4), the mixing rate was more than 8 min per 5 μL (i.e. > 96 s/μL) because the integrated peristaltic pumps did not provide a sufficient pumping-rate [25]. As described in this paragraph, mixers used in microfluidic networks have suffered from insufficient mixing performance.

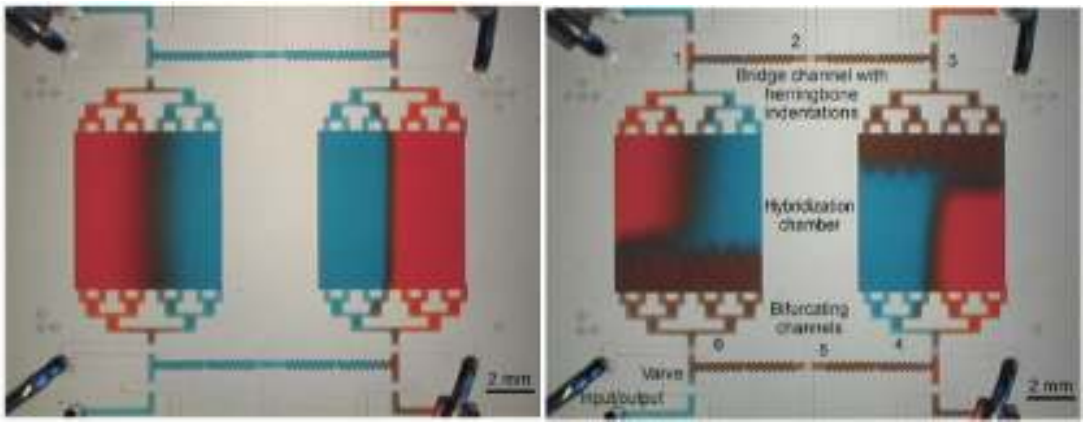

Figure 2.4. DNA hybridization chip and its micromixing process. The peristaltic pumps (1–3 and 4–6) circulated the solutions and the herringbone protrusions produced chaotic mixing [25].

2.2 Thermal Modulator

Comprehensive two-dimensional gas chromatography (GC×GC) is an analytical technique used to separate and detect the components of complex mixtures of volatile organic compounds [27, 28]. To understand the principle of the technique, we review the concept of (1) a separation *dimension* and (2) *comprehensive* separation. According to Giddings [29], the dimensionality of a separation method can be viewed as the number of different separation mechanisms to which the sample is subjected. The best results are obtained when the separation mechanism in each dimension is independent. Two-dimensional separation provides a means to substantially increase the peak capacity (i.e., the number of compounds that can be separated in a given analysis), because the sample is firstly separated by the first-dimension column and then subsequently separated by the second-dimension column. Ideally, two-dimensional separations provide a large number of chromatographic peaks of $n1 \times n2$, where $n1$ and $n2$ are the peak capacities of the first and the second dimension, respectively. The concept of comprehensive separation is simply that the entire sample is subjected to separation [27]. In other words, when only a small fraction of the first-dimension elute is transferred to the second dimension, it is not the comprehensive separation. Therefore, GC×GC means the entire sample is separated on two different dimensions, and no information gained during the first separation is lost during the second one [28].

Typically, a long narrow tube coated with a thin layer (stationary phase) is used as a separation dimension, called column (Figure 2.5A). However, even though the entire sample is used in the separation, the information loss is inevitable when the separation in

the second dimension does not preserve the separation order achieved in the first dimension. Because the two columns use different stationary phases that have distinct separation mechanisms based primarily on either volatility or polarity, the mobility of each compound in a sample mixture may greatly change in the next dimension column. Figure 2.5B shows the possible scenario that may happen in the separation process: the two kinds of samples (rectangle and circle) which are firstly separated in the first-dimension column may recombine in the second-dimension column and even change their elution order if the mobility of the rectangular samples is higher in the second-dimension column due to their lower polarity. This instrumental setup therefore destroys the separation order achieved from the first-dimension column, making the analysis much more difficult.

To preserve the separation order, an extra component, namely a modulator, is necessary. Figure 2.5C shows how modulator works at the interface of the two columns. To explain the modulation process, samples with different shapes (rectangle and circle) and colors (blue and red) are assumed to elute from the first-dimension column (step 1 in Figure 2.5C); here, the different shape and color correspond to the samples with different volatility and polarity, respectively. With the addition of the modulator, the elution order on the first-dimension column can be varied with the elute entering the second-dimension column. The modulator traps and focuses a small amount of circular samples (step 2 in Figure 2.5C), and then injects it into the second-dimension column while collecting the remaining circular samples in the interface (step 3). During the collection process in the modulator, the reintroduced circular samples in the second-dimension column are further

separated based primarily on their different polarity. The modulator traps and focuses the remaining circular samples until the previously injected samples in the

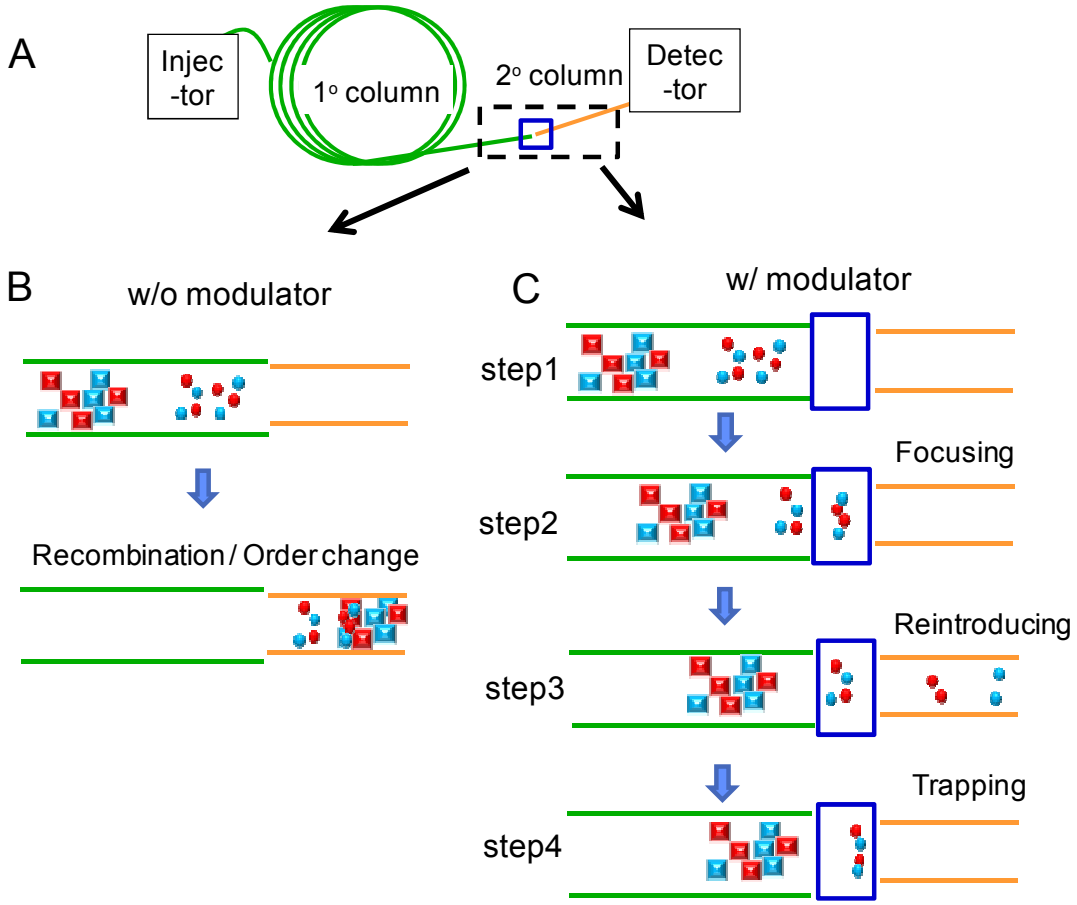

Figure 2.5. Need for the GC×GC interface. **(A)** GC×GC system. **(B)** Recombination or order change without modulator interface. The process illustrates how bands separated on one column can recombine or change the elution order on the second-dimension column without a modulator. **(C)** Preservation of separation order with modulator. The process illustrates how the modulator (interface) traps samples from the first-dimension column, and then allows discrete bands to pass through the second dimension column while trapping other fractions [27].

second-dimension column have eluted completely (step 4 in Figure 2.5C). Thus, modulation period (Trapping, focusing, and reintroducing cycles) should be at least longer than the elution-time at the second-dimension column, thereby maintaining elution order of the first-column effluents. In this way, components separated on the first-dimension column are parsed into several segments, each of which is eluted through the second-dimension column by repeating this modulation in rapid succession.

Because the great enhancement of peak capacity in GC×GC is only enabled by preserving the separation order and generating sharp peaks through a modulator, the modulator can be considered as the heart of a GC×GC system. Accordingly, much effort was devoted to the development of a simple, robust modulator with a wide application range [28]. A pneumatic [30, 31] or thermal [32–40] modulator is used at the interface between the two columns, with the latter generally providing a greater degree of sensitivity enhancement. In the volatile and semi-volatile samples, the mobility of the samples in the column or the thermal modulator is dependent on the temperature. When the thermal modulator cools down, the sample moves slowly or stops inside the modulator column (or channel). The sample moves fast when the thermal modulator heats up.

Thermal modulators (TMs) are classified into three types, which are used in conventional bench-scale GC×GC systems: (1) heat, (2) cryogenic, and (3) jet-pulsed modulators. In a heat modulator, the sample is trapped by a thick stationary-phase film in the modulator channel to increase the retention time of the samples beyond the modulation period. Philip and Liu first showed the thermal modulator using the thick stationary phase [32]. In their modulator, a heat pulse is applied, and the samples are

then released to the second-dimension column. Although it was the seminal work, the interface had many weaknesses, mainly due to the fact that the modulator channels and the paint coating for heater were not robust. Also it was difficult to uniformly coat the stationary phase inside the modulator channels because of the thickness. The first reliable heat modulator (Figure 2.6) was also developed by Philip and coworkers [33, 34]. The rotating thermal modulator periodically passes along a segment of thick-film channel. Although the modulator performed well for many applications, the modulator was potentially susceptible to mechanical damage because of the moving parts.

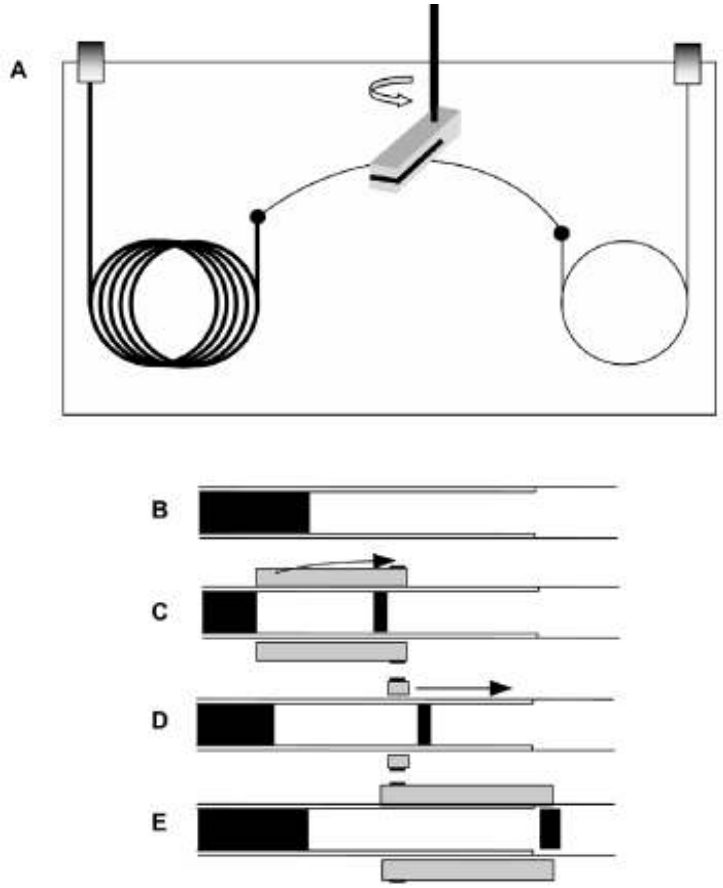

Figure 2.6. Example of heat modulator. **(A)** Schematic of rotating type. **(B–E)** Modulation sequence [33].

In a cryogenic modulator, trapping is achieved with a cryogenic zone placed over the modulator channel (Figure 2.7). The sample portions are released onto the second-dimension column when the cryogenic zone is removed from the modulator tube, and the samples resume motion because the oven temperature is reestablished over the modulator tube [35–37].

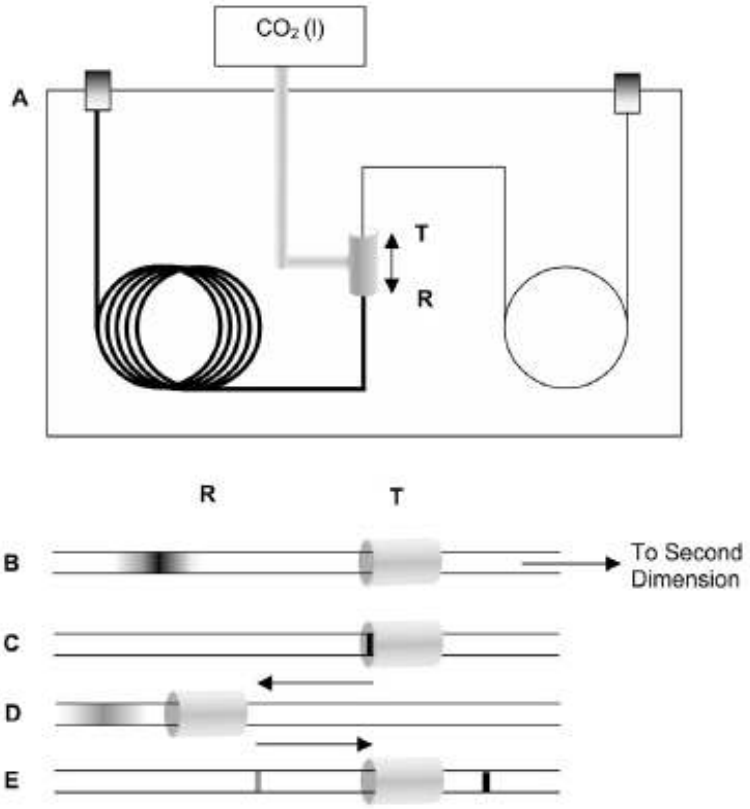

Figure 2.7. Example of cryogenic modulator. **(A)** Schematic of longitudinally modulated cryogenic system. T and R represent the trap and release positions of the cryotrap as it moves along the column. **(B–E)** Modulation sequence [35].

One advantage that cryogenic modulation offers over heated modulation is that the temperature of the modulator only needs to be raised to the oven temperature for desorption, not to a temperature above that of the oven. This allows for higher oven temperatures to be used in the analysis compared to heated modulators. The weakness of this approach is that with the moving trap, damage to the columns may easily occur. Another drawback of this modulator comes from the use of liquid CO_2, which can only cool to approximately −30°C. This temperature is not sufficiently low to trap more volatile samples.

In a jet-pulsed modulator, trapping and releasing are actively produced by synchronized pulsing of a set of hot and cold jet nozzles [38–40]. The simplified version in Figure 2.8 was developed by Beens et al [40]. The modulator uses only two cryojets for trapping, allowing the GC oven to provide warm air for heating the trapping zones. This removed the two warm jets from the previous jet design while maintaining good performance of the modulator. However, liquid CO_2 cannot cool sufficiently to trap some very volatile samples. Although liquid nitrogen can be an alternative to provide sufficiently low temperature, disadvantages of using liquid nitrogen include the complex design of the delivery system and the large amount of consumption of cryojets.

Overall, the three types of modulators commonly use conductive or convective heating techniques to rapidly raise the temperature of the modulator. However, those macro-scale TMs relying on cryogenically cooled fluids are resource intensive [35–40] and/or demand a large amount of refrigeration work (e.g., ~10 kJ for a cooling cycle of ~5 s) [41]. Furthermore, power dissipation for typical heating devices can be on the order of 1 kW [32–34, 41]. These high power and large amount of consumption in gas

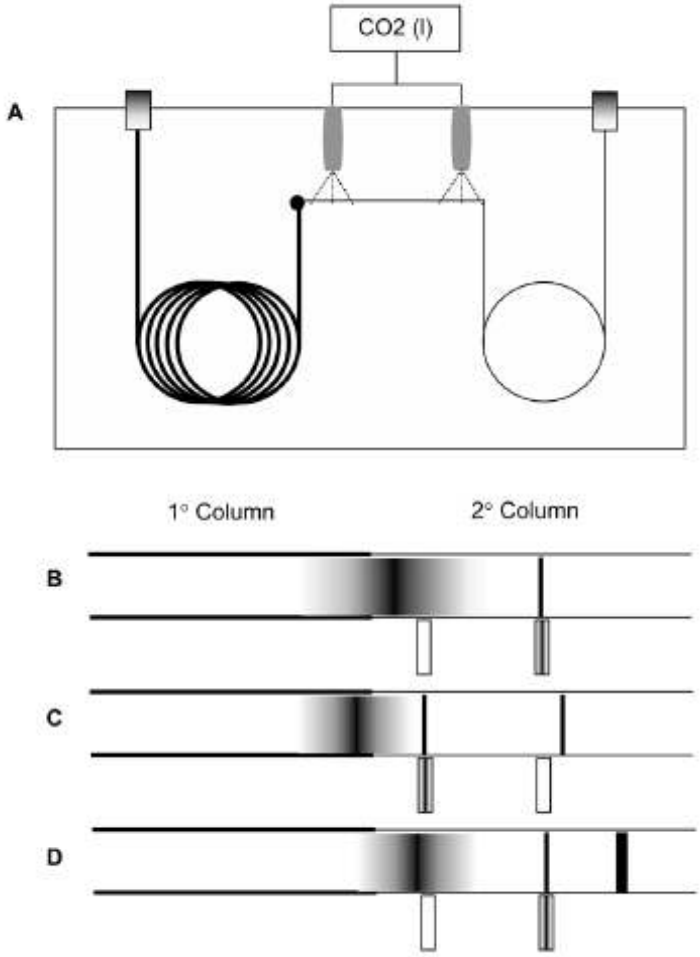

Figure 2.8. Example of cryojet modulator [40]. **(A)** Schematic of dual cryojet system. **(B–E)** Modulation sequence.

and cryogenic materials is unsuitable to be integrated in a spacecraft that lacks sufficient sources. Moreover, the size of the modulator should be as small as possible to be integrated in the spacecraft, and there should be no moving parts for mechanical strength.

Numerous efforts have been made to develop GC prototypes containing microfabricated components (μGC) [42–54]. These miniaturized systems [43–47] and their components [48–54] can operate at relatively low power; however, the lengths of

the columns employed are inherently limited (Figure 2.9), with typical columns ranging in length from 0.5 to 3 meter [47–53]. This places an inherent limit on the peak capacity. A μGC system incorporating two-dimensional gas chromatography (i.e., μGC×μGC) is a promising approach to overcome this limitation. Although a preliminary report has recently been described on the use of pneumatic modulation in a μGC×μGC system [55], there has yet to be a report on a microfabricated TM (μTM) for μGC×μGC applications. To be effective, the μTM must span a broad range of temperature (e.g. -50 to 250 ^{o}C) at a very high rate (> 1000 ^{o}C s^{-1}, ideally during both heating and cooling).

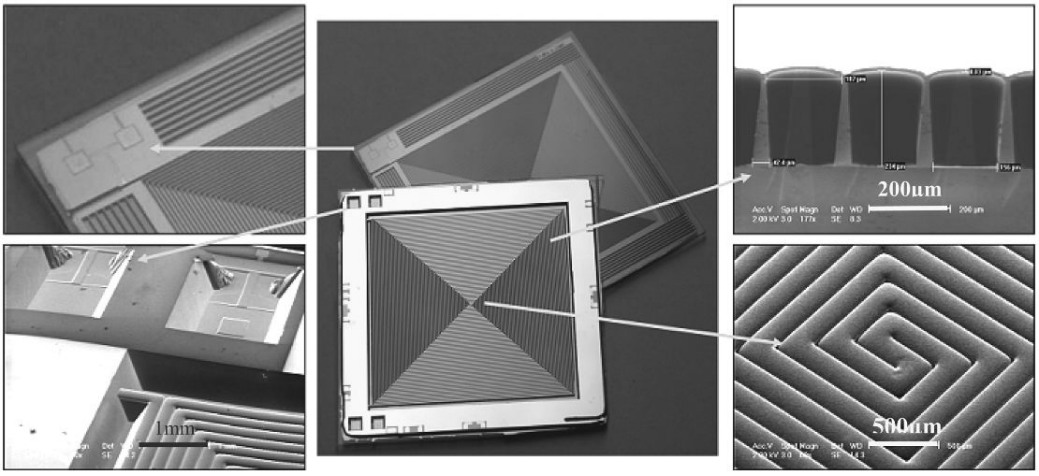

Figure 2.9. Photographs of microfabricated 3-m long separation column [51].

CHAPTER III

MICROMIXER

3.1 Concept

Micromixing is a crucial step for biochemical reactions in microfluidic networks. A critical challenge is that the system containing micromixers needs numerous pumps, chambers, and channels not only for the micromixing but also for the biochemical reactions and detections. Thus, a simple and compatible design of the micromixer element for the system is essential.

Here, we present how temperature-programmed natural convection leads to significant mixing in the microfluidic regime [56]. Most important, this study enables micromixing and a subsequent biochemical reaction in a single microfluidic chamber, within a simple pumpless platform (Figure 3.1). As a model application, we sequentially show micromixing and PCR in a single chamber, while maintaining a fast thermal response. Our system consists of two separate subunits with distinct functions: (a) a microfluidic cartridge and (b) a microfabricated heating-instrument. The microfluidic cartridge has

simple 2-D microchannels and a chamber. In contrast to previous methods, our microfluidic cartridge uses capillarity to control the merging of two streams and their

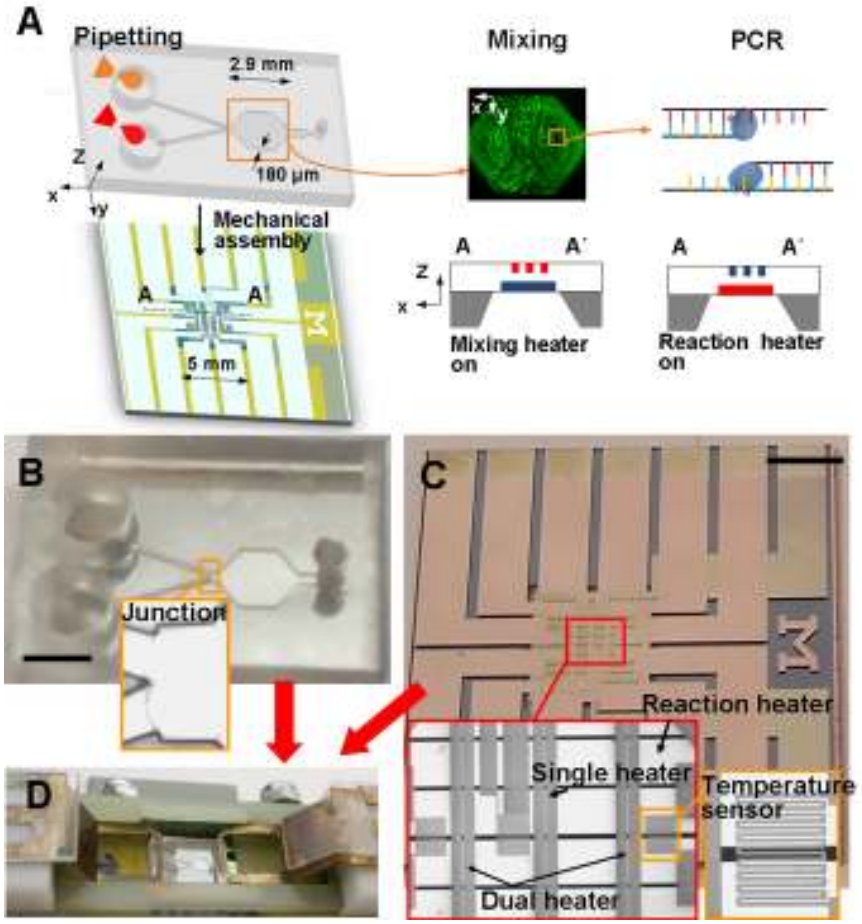

Figure 3.1. Single-chamber micromixing and PCR. (**A**) Sequential process of pipetting, micromixing, and PCR. After injecting solutions, their streams fill the chamber by capillarity. Upper- and lower-level heaters embedded in a membrane are used for micromixing and PCR, respectively. Natural convection induces micromixing. (**B**) Microfluidic cartridge. The microfluidic cartridge is a disposable component, which has simple 2-D shape microchannels and a chamber where the height is 180 μm. Sample transport is driven by capillarity in the microfluidic cartridge. The PDMS cartridge slab is coated with parylene for preventing evaporation of solutions. A stainless-steel film of 8 μm thickness is used as the sealing membrane at the bottom of the chamber. (**C**) Microfabricated heating-instrument. The microfabricated heating-instrument is a component for repeated use that incorporates temperature sensors and heaters within the membrane. The single and dual heaters are for micromixing, and the reaction heater is for PCR. (**D**) Assembly of heating instrument and microfluidic cartridge components. Scale bars, 3 mm.

filling of the chamber; this step is an autonomous process without any external pumps. Also, solutions can be injected into inlets simply by pipettes, thus removing interfacing-tubes for external pumps. The microfabricated heating-instrument incorporates mixing and reaction heaters (Figure 3.1C). The mixing heaters, composed of single and dual heaters, induce natural convection for homogenizing the different solutions within the microfluidic chamber. Afterwards, the reaction heaters are used to implement the PCR process. By programming the heaters with a time sequence of applied voltages, the sample transport, micromixing, and PCR are all autonomously performed in a seamless sequence.

3.2 Thermal Modeling

3.2.1 Scale analysis for flow behavior

To design a micromixer device with desired performance, we consider flow behavior inside a vertical enclosure where its side wall is heated. Consider a two-dimensional enclosure of height H and horizontal length L, where two vertical walls are heated and cooled at different temperatures, respectively (Figure 3.2A). It should be noted that the flow behavior is strongly dependant on the size and the aspect ratio (H/L) of the enclosure. The temperature gradient ΔT between the two walls in conjunction with the gravity g makes buoyancy, thus generating flow motion inside the vertical enclosure. The flow bordering each sidewall grows initially and reaches a steady state. At the final stage, the flow forms a thermal boundary-layer along each wall in a steady state. Inside

the thermal boundary-layer significant temperature-gradient exits, but outside the layer temperature is relatively uniform. Because fluidic boundary layer scales with thermal boundary layer, there is a dominant flow only inside/near the thermal boundary layer but fluid is nearly stagnant outside the thermal boundary layer. Thus, the thermal boundary-layer thickness δ_T is an important parameter that allows us to predict the flow behavior for micromixing driven by natural convection. If δ_T along the vertical wall is smaller than the enclosure length L, then the thermal layer is prominent only near the vertical wall, making the core region stationary. This condition is expressed as follows [57]:

$$\frac{H}{L} < \mathrm{Ra}_H^{1/4} \tag{3.1}$$

where Rayleigh number, which is the ratio of buoyant flow-driving forces to diffusive flow-resisting forces, is $\mathrm{Ra}_H = g\beta\Delta T H^3/(\alpha\nu)$; and β, α, and ν are the thermal expansion coefficient, thermal diffusivity, and kinematic viscosity of the fluid, respectively. To derive Equation 3.1, the conservation of energy equation is first considered as:

$$\frac{\partial T}{\partial t} + u\frac{\partial T}{\partial x} + v\frac{\partial T}{\partial y} = \alpha\left(\frac{\partial^2 T}{\partial x^2} + \frac{\partial^2 T}{\partial y^2}\right) \tag{3.2}$$

Initially, the fluid bordering each side wall is nearly motionless; thus, Equation 3.2 expresses a balance between thermal inertia and conduction normal to the side wall, thereby leading to

$$\frac{\Delta T}{t} \sim \alpha \frac{\Delta T}{\delta_T{}^2} \tag{3.3}$$

By rearranging Equation 3.3, we have the following relation for the thermal boundary layer:

$$\delta_T \sim (\alpha t)^{1/2} \tag{3.4}$$

To analyze the motion of the thermal boundary layer, we use the conservation of momentum equations as:

$$\frac{\partial u}{\partial t} + u\frac{\partial u}{\partial x} + v\frac{\partial u}{\partial y} = -\frac{1}{\rho}\frac{\partial P}{\partial x} + \nu\left(\frac{\partial^2 u}{\partial x^2} + \frac{\partial^2 u}{\partial y^2}\right) \tag{3.5}$$

$$\frac{\partial v}{\partial t} + u\frac{\partial v}{\partial x} + v\frac{\partial v}{\partial y} = -\frac{1}{\rho}\frac{\partial P}{\partial y} + \nu\left(\frac{\partial^2 v}{\partial x^2} + \frac{\partial^2 v}{\partial y^2}\right) - g\left[1 - \beta(T - T_0)\right] \tag{3.6}$$

where u, v, and P are the horizontal velocity, the vertical velocity, and the pressure, respectively. The velocity scale of the upward motion is easier to see if we eliminate the pressure P in Equations 3.5 and 3.6 as:

$$\begin{aligned} &\frac{\partial}{\partial x}\left(\frac{\partial v}{\partial t} + u\frac{\partial v}{\partial x} + v\frac{\partial v}{\partial y}\right) - \frac{\partial}{\partial y}\left(\frac{\partial u}{\partial t} + u\frac{\partial u}{\partial x} + v\frac{\partial u}{\partial y}\right) \\ &= \nu\left[\frac{\partial}{\partial x}\left(\frac{\partial^2 v}{\partial x^2} + \frac{\partial^2 v}{\partial y^2}\right) - \frac{\partial}{\partial y}\left(\frac{\partial^2 u}{\partial x^2} + \frac{\partial^2 u}{\partial y^2}\right)\right] + g\beta\frac{\partial T}{\partial y} \end{aligned} \tag{3.7}$$

This equation contains three basic groups — inertia terms on the left-hand side and four viscous diffusion terms plus the buoyancy term on the right-hand side. In Equation 3.7, it can be shown that the friction term is balanced by buoyancy through scale analysis, and based on the analysis initial vertical velocity-scale can be obtained as follows:

$$v \sim \frac{g\beta\Delta T\alpha t}{\nu} \tag{3.8}$$

This velocity scale is valid for fluids where Prantdl number Pr is >1. So far, we have obtained the relation between the flow motion and the thermal boundary layer at the initial stage. As the time increases, the convection effect becomes more important while the thermal inertia effect becomes minor in the energy equation (Eq. 3.2). From Equation 3.2, the final time t_f is determined when the enthalpy carried away vertically by the buoyant layer balances with the heat conducted from the wall as:

$$v\frac{\Delta T}{H} \sim \alpha\frac{\Delta T}{\delta_T{}^2} \tag{3.9}$$

In conjunction with Equation 3.4 and 3.8, Equation 3.9 yields:

$$t_f \sim \left(\frac{vH}{g\beta\Delta T\alpha}\right)^{1/2} \tag{3.10}$$

At this time, the thermal boundary layer thickness is:

$$\delta_T \sim (\alpha t_f)^{1/2} \sim H\mathrm{Ra}_H^{-1/4} \tag{3.11}$$

Equation 3.11 finally gives us Equation 3.1 by comparison of *L*.

Also, the stream along the horizontal wall is dominant only near the wall while the stream is stationary where it is away from the wall when the following condition is met:

$$\frac{H}{L} > \mathrm{Ra}_H^{-1/4} \tag{3.12}$$

Equation 3.12 is obtained by the scaling analysis using enthalpy of the horizontal stream and vertical thermal conduction [57] as we did for Equation 3.1. Based on the equations 3.1 and 3.12, the flow inside the enclosure is categorized into three regimes (Figure 3.2B and 3.2C): (I) Tall enclosure limit regime, (II) Boundary layer regime, and (III) Shallow enclosure limit regime. In regime (I), the thermal boundary layer thickness along the side walls is greater than *L*. Thus vertical flow is dominant across the enclosure but horizontal flow exists only inside/near the thermal boundary-layer. In regime (II), the thicknesses of thermal boundary layer along the vertical and horizontal walls are smaller than *L* and *H*, respectively. Thus the core region is dominated by a nearly stagnant fluid. In regime (III), the thermal boundary layer thickness along the top and bottom walls is greater than *H*. Thus horizontal flow is dominant across the enclosure but vertical flow exits only inside/near the thermal boundary layer.

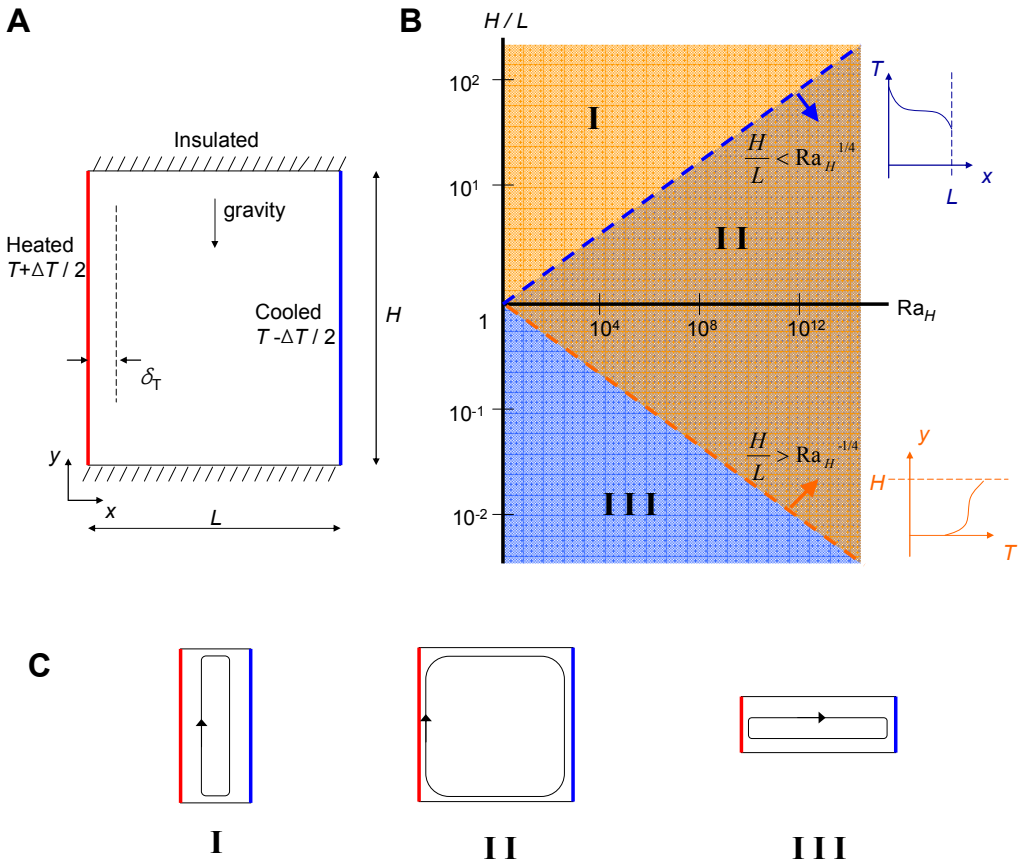

Figure 3.2. Natural convection in vertical enclosure. (**A**) The boundary conditions in two-dimensional rectangular enclosure. H and L are the height and the length of the enclosure, respectively. (**B**) The three heat transfer regimes (Regimes I, II, and III). In the blue region characterized by $H/L < \mathrm{Ra}_H^{1/4}$ (Regime II and III), the thickness of thermal boundary layer along side wall is smaller than L. In the orange region characterized by $H/L > \mathrm{Ra}_H^{-1/4}$ (Regime I and II), the thickness of thermal boundary layer along top and bottom walls is smaller than H. When $\mathrm{Ra}_H < 1$, there is no natural convection because conduction is dominant. (**C**) The flow patterns associated with regimes in (B) [57].

In our device, the Rayleigh number Ra_H is calculated to be in the order of 10^3, and aspect ratio H/L is in the range of 2–5. In this case, the thermal boundary layer approximately covers the entire region in the microfluidic chamber, thus eliminating relatively stagnant flows. This thermal boundary condition ensures effective

micromixing. Besides the flow pattern, the flow speed V can be expressed as follows [58]:

$$V = (\beta \Delta T / \nu) H^3 \mathrm{f}(x, y) \tag{3.13}$$

where f(x,y) is the function of position. Because ΔT and β are proportional to temperature but ν is inversely proportional to temperature, V increases rapidly as temperature increases. Also, the equation shows that V increases rapidly as H increases. However, as we have explained, the flow becomes more prominent only near the walls as the size of the chamber becomes larger. In our design, we set the H as ~ 2 mm. This value provides a thermal boundary layer that has several hundreds of micron thickness, thus eliminating a stationary flow region generated at L < 1 mm.

3.2.2 Computational Simulation for Temperature Gradient

A temperature gradient is an important parameter that determines vortex patterns. To generate multiple vortices, multiple hot and cold regions with high temperature gradient are necessary. This temperature condition can be achieved by proper design of the heater and proper selection of the membrane material. Our computational simulation shows that a high temperature gradient can be obtained when a membrane with relatively low thermal conductivity (i.e., stainless steel, 13 W/Km) is used (Figure 3.3A and 3.3B). In contrast, a membrane with higher thermal conductivity (e.g., aluminum, 237 W/Km) yields a small thermal gradient (Figure 3.3C); because of the heat spreading effect, the

temperature of the chamber becomes much lower than the one incorporating the stainless-steel membrane at the same heating condition.

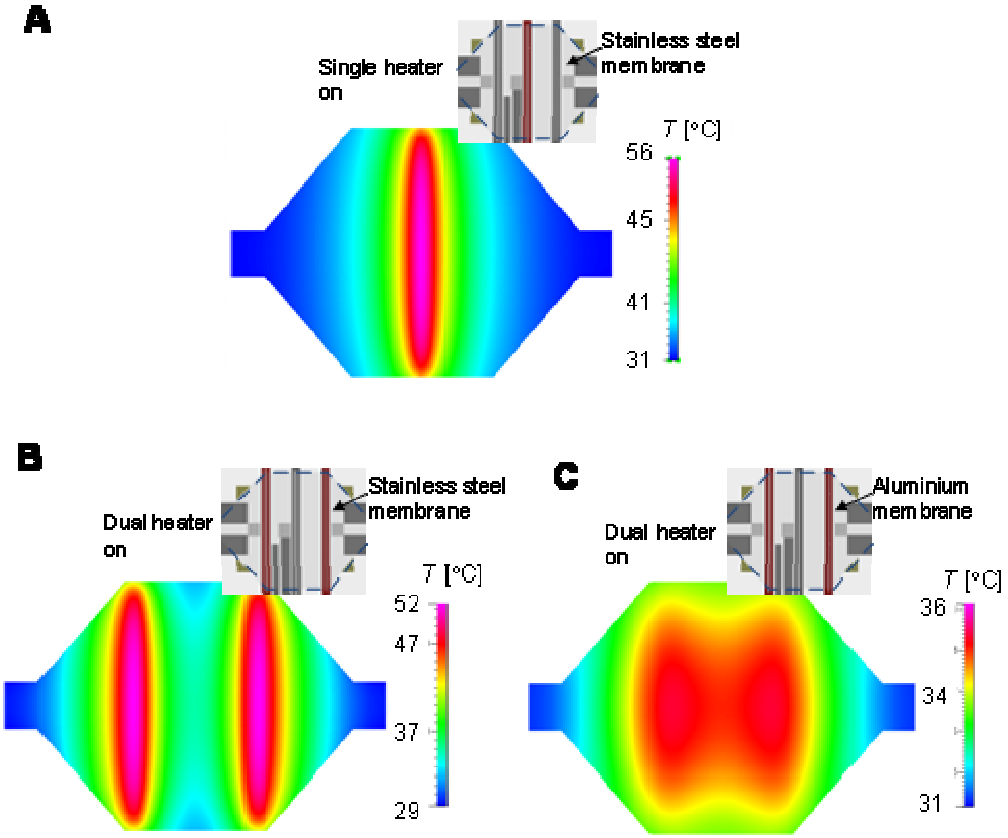

Figure 3.3. Computational simulation of temperature distribution. (**A**) The single heater is on at a heat flux of 250 kW/m^2. Stainless steel is used as the membrane material. (**B** and **C**) The dual heater is on at a heat flux of 180 kW/m^2. For comparison, the simulations assume stainless steel and aluminum as the membrane material in (B) and (C), respectively. The thickness of the membranes is 8 μm. The simulations with a 3-D heat-flow domain were performed using commercial software (CFD-ACE+, CFD research). The control volume used in the analysis includes water filling the PDMS chamber, the membrane, and the air gap between the membrane and the thermoelectric cooler.

3.3 Materials and Methods

This chapter discusses the fabrication and experimental methods for the designed device. The device fabrication was performed at the University of Michigan Lurie Nanofabrication Facility. Experimental methods include calibration of resistive-type temperature sensors, measurement of mixing, and PCR.

3.3.1. Microfabrication of the Microfluidic Cartridge

The microfluidic cartridge (Figure 3.4) is composed of a polydimethylsiloxane (PDMS, Sylgard 184, Ellswoth Adhesive) slab and a 8 μm-thick stainless-steel film (SUS304, Nilaco). The microfluidic channels and the chamber in the PDMS were fabricated using soft lithography [59]. The mold for the soft lithography was a 4-inch Si wafer, which was patterned by deep reactive ion etch, and the surface of the mold was rendered hydrophobic by CF_x gas. The precursor of PDMS was cured on the mold at room temperature and then was released from the mold. Then inlet and outlet holes were punched by using

biopsy punches. To prevent the vapor evaporation during the mixing and PCR processes, a 3 μm-thick parylene layer was deposited on the replica-molded PDMS slab [60]. A SU-8 (SU-8 5, Microchem) glue layer was used for the bonding of the PDMS slab and the stainless-steel film as follows: first, a 3 μm-thick film of SU-8 was spin-coated on a silicon wafer and transferred to the PDMS slab by a contact printing method. Then the

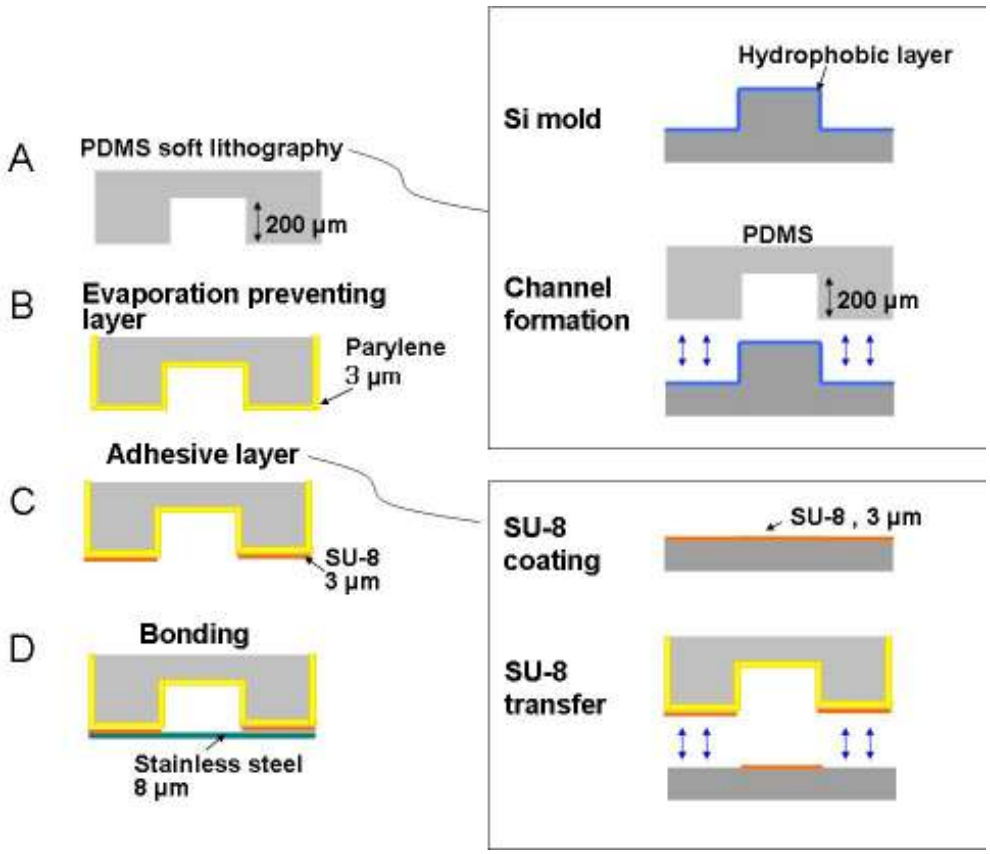

Figure 3.4. Microfabrication process of the microfluidic cartridge. (**A**) The mold for the soft lithography was fabricated on a 4-inch Si wafer using deep reactive ion etch, and the surface of the mold was hydrophobically treated by CF_x gas. The precursor of PDMS was cured on the mold at room temperature and then was released from the mold. Then inlet and outlet holes were punched using biopsy punches. (**B**) To prevent vapor evaporation during the mixing and PCR processes, a 3 µm-thick parylene layer was deposited on the surface of the replica-molded PDMS slab. (**C**) SU-8 (SU-8 5, Microchem) was used as a glue material for the bonding of the PDMS slab and the stainless-steel film; SU-8 was spin-coated on a silicon wafer to form a layer of 3 µm thickness and was transferred to the PDMS slab by contact printing. (**D**) The PDMS slab and the stainless-steel film were finally bonded together by a mild pressure followed by UV exposure and curing at 80^{o}C for 2 min.

PDMS slab and the stainless-steel film were bonded together at a mild pressure followed by UV exposure and curing at 80^{o}C for 2 min. This method is similar to the adhesive bonding process by Wu *et al* [61].

3.3.2. Microfabrication of the Heating Instrument

The heating instrument was built by the conventional microfabrication process (Figure 3.5). The starting substrate was a 4-inch silicon wafer of 450-μm thickness. One micrometer oxide was thermally grown on the both sides of the wafer. Then the backside of the wafer was photolithographically patterned. The substrate was dipped in buffered hydrofluoric acid solution; simultaneously, the oxide on the front side of the wafer was removed for anodic bonding and the one on the backside of the wafer was patterned to serve as the etch mask of silicon. A glass wafer (Pyrex 7740, Sensors Prep Services, 100 μm in thickness) was anodically bonded to the silicon wafer. Reaction heaters were fabricated on the glass layer by lift-off of a Ti/Pt (20 nm/100 nm in thickness) layer in an acetone solution. Then, a 4 μm-thick oxynitride layer was deposited by a PECVD process for electrical passivation. Next, mixing heaters and temperature sensors, also made with Ti/Pt (20 nm/100 nm in thickness) layers, were formed by a lift-off process. An oxynitride layer (1 μm in thickness) was deposited again for electrical passivation. The silicon under the glass was removed by an ethylene-diamine-pyrocatechol solution. Finally, the wafer was diced into individual chips, followed by the etching of the glass layer in a hydrofluoric acid solution (49% concentration). The final membrane thickness combining the glass and oxynitride layers was approximately 15 μm in total.

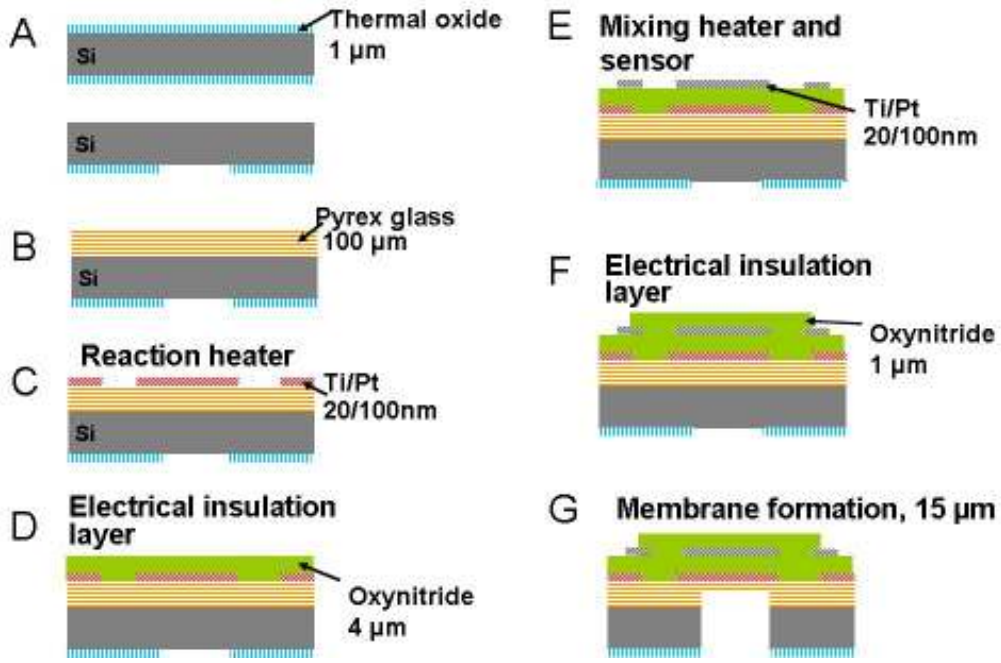

Figure 3.5. Microfabrication process of the heating instrument. (**A**) The process was started with a silicon wafer of 4 inches in diameter and 450 µm in thickness. We thermally grew a 1-µm oxide layer on the both sides of the wafer. Then the backside of the wafer was photolithographically patterned. The substrate was dipped in a buffered hydrofluoric acid solution; simultaneously, the oxide layer on the front side of the wafer was removed for anodic bonding, and the one on the backside of the wafer was patterned as an etch mask of silicon. (**B**) A glass wafer (Pyrex 7740, Sensors Prep Services, 100 µm thickness) was anodically bonded to the silicon wafer. (**C**) Reaction heaters were fabricated on the glass layer by the lift-off of a Ti/Pt (20 nm/100 nm in thickness) layer in an acetone solution. (**D**) A 4 µm-thick oxynitride layer was deposited by a PECVD process for electrical passivation. (**E**) Mixing heaters and temperature sensors, also made with Ti/Pt (20 nm/100 nm in thickness) layers, were formed by a lift-off process. (**F**) An oxynitride layer (1 µm in thickness) was deposited again for electrical passivation. (**G**) The silicon portion under the glass was removed by wet etch using an ethylene-diamine-pyrocatechol solution. Finally, the wafer was diced into individual chips, followed by the etching of the glass layer by a hydrofluoric acid solution (49% concentration). The final membrane thickness combining the glass and the oxynitride layers was approximately 15 µm in total.

3.3.3. Assembly of the Microfluidic Cartridge and the Heating Instrument

When the microfluidic cartridge was placed on the heating instrument, we used mechanical clamps to secure close contact between the two subunits. A mild pressure was applied on the top surface of the microfluidic cartridge to prevent the buckling of the stainless-steel membrane. A thermoelectric cooler (MI1021T, Marlow industries) under the heating instrument was used for fast cooling of the microfluidic cartridge. To effectively cool the chamber while maintaining fast heating at low power, we made a 60 μm air-gap (Figure 3.6) between the thermoelectric cooler and the membrane at the heating instrument.

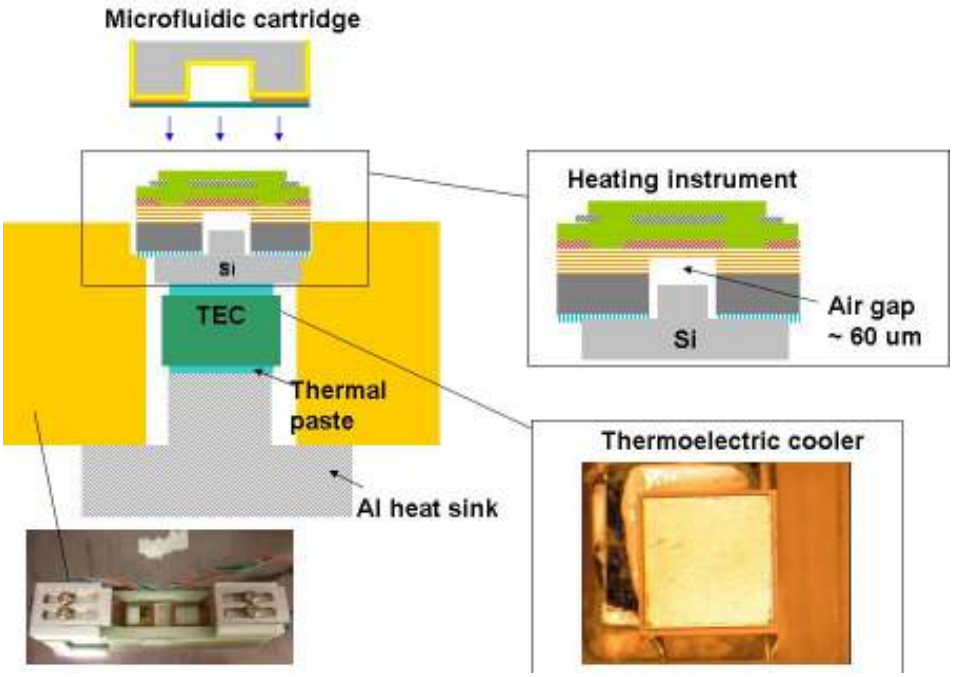

Figure 3.6. Assembly of the microfluidic cartridge and the heating instrument. The 60 μm air gap under the heating instrument plays a critical role in providing sufficient thermal isolation for the microfluidic chamber. The gap size was selected through careful thermal simulation to minimize both the heating power and cooling time of the thermal cycle operation. The Si spacer directly conducts heat from the heating instrument to the thermoelectric cooler.

3.3.4 Temperature Control

The calibration of the resistive-type temperature-sensors was performed with the microfabricated heating-instrument incubated in a convection oven. The resistances of the sensors were measured using a four-point probe technique at varying temperature (Figure 3.7), and the data were recorded using a computer program (LabVIEW 7.1, National instruments). The slope and intercept from a linear fit were used to obtain the temperature-resistance correlation for the temperature sensing. For micromixing, open-loop temperature-control was used. In the single heating (SH) and dual heating (DH) modes, a constant voltage was applied to the heaters using a DC power supply (E3646A,

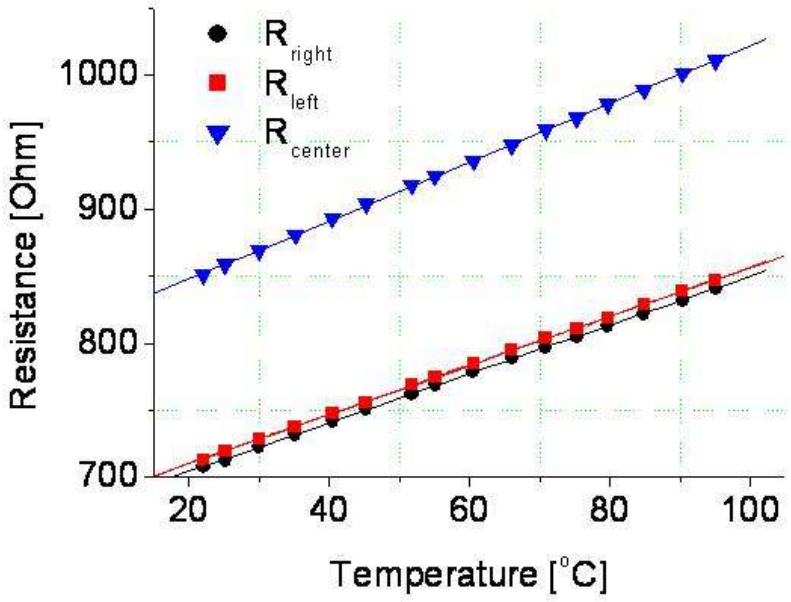

Figure 3.7. Calibration of the restive type temperature sensors. The changes in the resistance of the three temperature sensors were all linear ($R^2 = 0.9999$).

Agilent), whereas, in the alternating heating (AH) mode, square pulses were applied using a function generator (33250A, Agilent) and an op amp (OPA544T, Texas Instrument). In the PCR process, temperature was controlled by varying the voltage of a DC power supply (Model 1760, BK precision) with a LabVIEW program based on a proportional-integral algorithm [62]. The temperature of the thermoelectric cooler was maintained at 17±1°C.

3.3.5. Measurement of Flow Speed and Micromixing

In the measurement of the flow speed at steady-state, we used fluorescent microbeads of 8 μm diameter (35-3, Duke scientific) as flow tracers. We obtained the value of the local flow speed from the length of a particle pathline captured by image analysis software (ImageJ, National Institutes of Health) and its corresponding flight time. The average and the maximum flow speeds were measured for microbeads flowing on the mid plane of the chamber (i.e., the half height of the chamber). Although microbeads on other planes could be measured due to the depth of field of the microscope (±25 μm), the measurement error was estimated to be 6.3% assuming a parabolic velocity profile across the chamber height.

Standard deviation, ($\sigma = \langle (I - \langle I \rangle)^2 \rangle^{1/2}$), was used to quantify the degree of mixing, where I is the normalized intensity of each pixel (Figure 3.8). The grayscale value of each pixel's intensity was processed by using computer software (MATLB, Mathworks). To provide optical access to the vertically placed microfluidic chamber for a stereo

microscope (SZX16, Olympus) equipped with a CCD camera (MP3.3, Qimaging), we used a 45^{o} inclined mirror (Figure 3.7). We used a fluorescein (46980, Sigma-aldrich)

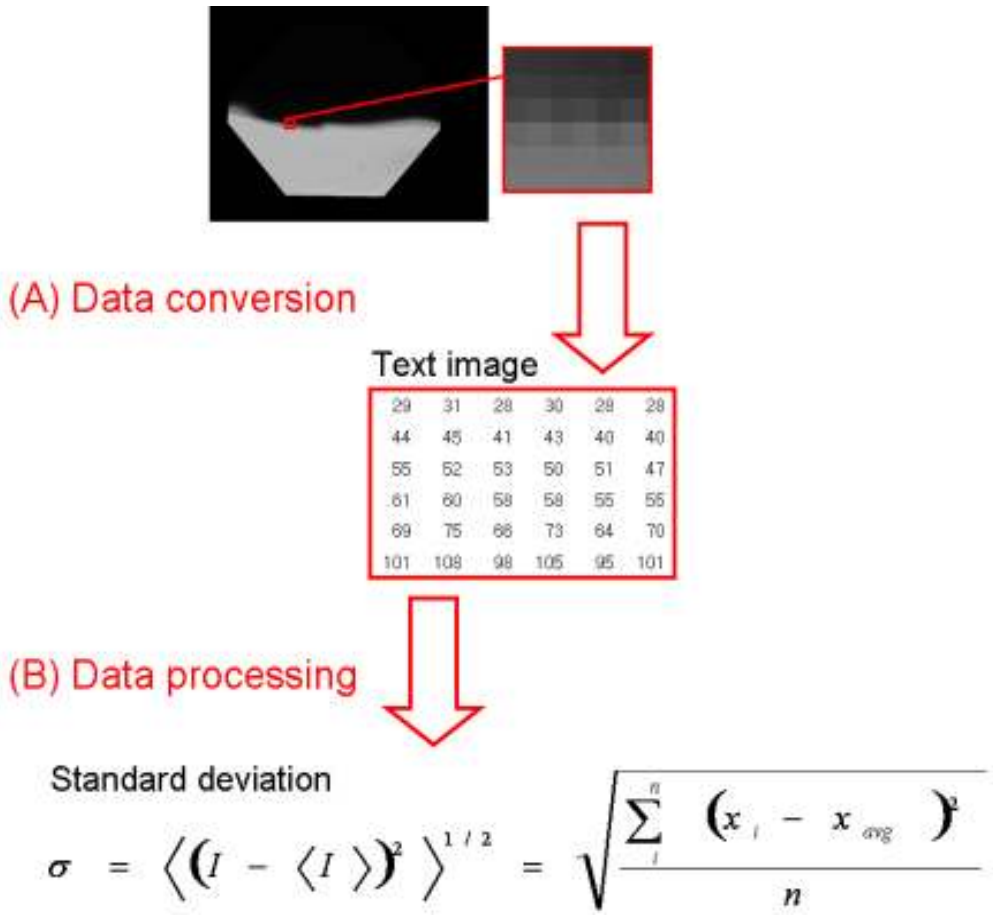

Figure 3.8. Procedure for obtaining standard deviation to quantify degree of mixing. (**A**) A tif image was converted to a text image file using image analysis software (ImageJ, National Institutes of Health). The grayscale values that correspond to the intensity of each pixel range from 0 to 255. (**B**) Data processing was done by using a home-made code in computer software (MATLB, Mathworks). The values in the text image were normalized using a maximum value; thus the normalized values (x_i) range from 0 to 1 for each pixel. Then the standard deviation was calculated using the formula. Here, x_{avg} is the average value over the normalized values and n is the number of data that corresponds to the total number of the pixels.

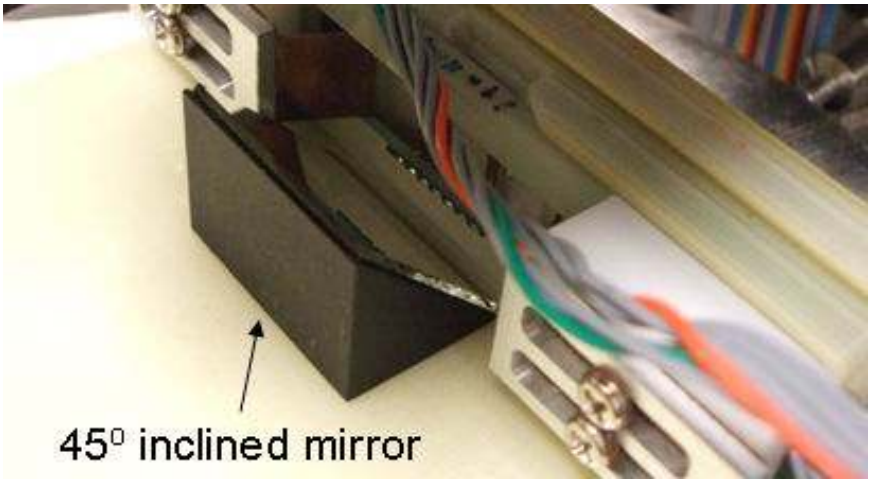

Figure 3.9. Experimental setup for visualizing flows in the vertically placed microfluidic cartridge chamber. To obtain optical access to the vertical chamber using a microscope, we used a 45° inclined mirror that has the microscope-mirror grade.

with low temperature sensitivity [63] to visualize the micromixing process. The solution used in the measurement of flow speed and the micromixing-degree commonly contained sucrose (S1888, Sigma-aldrich) of 10% (w/w) and sodium dodesyl sulfate (L4390, Sigma-aldrich) of 1.8% (w/w). The sucrose was added to increase the solution density up to 1.05 g/cm^3, which allows neutral buoyancy of the suspended fluorescent microbeads at room temperature; the calculated viscosity of the solution resulting from adding sucrose was 1.35 mPa/s at room temperature. The sodium dodesyl sulfate served as a surfactant to help the channel filling and merging processes at the junction of the microchannels.

3.3.6. PCR

A DNA fragment of 690 bp from the influenza viral strain A/LA/1/87 was amplified using the on-chip PCR. [62]. For obtaining the DNA sample, the hemaggultinin gene

(HA1) region of influenza viral RNA was reverse transcribed, amplified, ligated into the pGEM-T vector, and cloned into *E. coli.* The cloned plasmid was used to synthesize RNA *in vitro* with T7 RNA polymerase; then the RNA samples were subject to reverse transcription to produce the final DNA samples that were used for the on-chip PCR. For the micromixing-PCR process, two different solutions were injected in the two inlets, respectively. A 2 ng/μL DNA template in a TE buffer with Tween-20 was injected in one inlet. A reaction mixture of 0.2 mM dNTP, 60 mM Tris-HCl, 15 mM NH_4SO_4, 1.5 mM $MgCl_2$, 0.3 mM primers, and Taq DNA polymerase at 50 units/mL (Invitrogen) was injected in the other inlet. Tween-20 was used to match the surface tension of the two solutions. Mineral oil was used in the two inlets and the outlet for preventing the evaporation of solutions. The forward and reverse primers used here are 5′-GTTTGTTTCTCTGGTACATTCCGC-3′ and 5′-CAACTGTTACCCTTATGATGTGC C-3′, respectively. The thermocycling protocol consisted of a predenaturation process at 94°C for 5 s, then an amplification process following a temperature cycle of 94°C for 5 s, 55 °C for 10 s, and 72 °C for 20 s, and a final elongation process at 72°C for 30 s. We varied the total cycle numbers as 10, 20, and 30. The PCR product in each total cycle was collected in a tube from three PCR runs to compensate for the sample loss during the collecting and dispensing processes. Finally, the reaction sample in each tube was dispensed with a 1.5 μL volume in a single lane of a 1% agarose gel electrophoresis prestained with ethidium bromide.

3.4. Results and Discussion

This chapter demonstrates temperature-programmed natural convection for micromixing and biochemical reaction in a single chamber. For this goal, we show that micromixing using natural convection occurs significantly even at 37^{o}C at the proper configuration of the microheater and the chamber. Then, as a model application, we demonstrate micromixing and subsequent polymerase chain reaction (PCR) for an influenza viral DNA fragment. This process is achieved in a platform of a microfluidic cartridge and a microfabricated heating-instrument with a fast thermal response.

3.4.1. Natural Convection-driven Flows in a Chamber

In microfluidic devices, typical chamber height is in the range of a few tens or hundreds of micrometer. Due to this relatively small size, it has been commonly accepted that natural convection is weak or even negligible in the microfluidic regime. In fact, the pathlines (Figure 3.10A), shown by the trajectories of individual fluorescent particles, indicate that the convective flow is weak and probably of no use for micromixing, where the microfluidic chamber has a height as small as 180 μm, and gravity acts normal to the chamber-plane.

Natural convection is generated only when buoyancy force overcomes the resistance imposed by viscous force. Buoyancy force (F_b) is induced by density gradient and gravity, and strongly dependant on the characteristic length (L) of the chamber as $F_b \sim L^3$.

When a heater is on the chamber-plane, L is the height of the chamber if the chamber-plane is perpendicular to gravity whereas L is the width of the chamber if the chamber-plane is parallel to gravity. Although the typical height of microfluidic chamber is in the

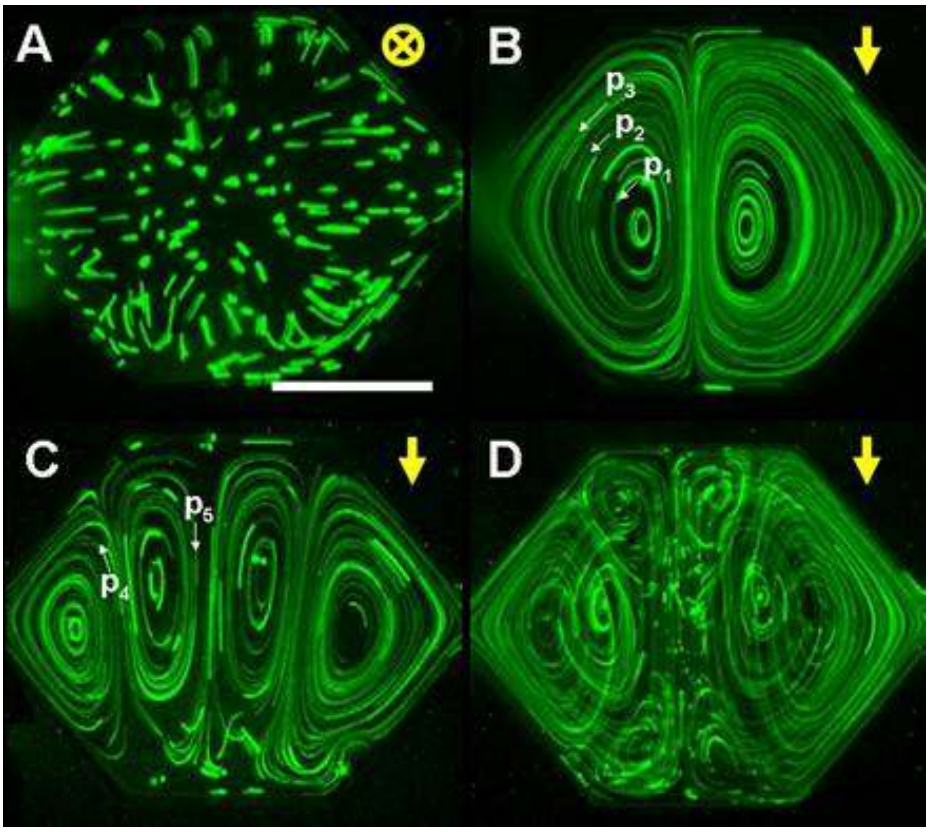

Figure 3.10. Natural convection driven flows in the chamber. (**A** to **D**) Flow trajectories of fluorescent microparticles for time duration of 35 s. Large arrows indicate the gravity direction, and small arrows depict the flow direction of the individual fluorescent particles of 8 μm-diameter. The Single heater is turned on in (A and B) and the dual heater is turned on in (C). Single and dual heaters are alternatingly turned on and off in (D). To see the vertical image of B to D, we used a 45° inclined mirror (Figure 3.9). Scale bar, 1 mm

micrometer scale, the width of the chamber can be more than one millimeter. Following the above simple principle, we can enhance natural convection in the microfluidic device by simply flipping the chamber 90^{o} to make the chamber-plane parallel to gravity. This configuration greatly increases L from 180 μm to ~1.4 mm, thus enhancing F_b almost a thousand orders. As shown in Figure 3.10B, natural convection is significantly enhanced. In this case, the Rayleigh number, which is the ratio of buoyant flow-driving forces to diffusive flow-resisting forces, is calculated to be 2.6×10^3, thus indicating that the process is primarily driven by buoyant force.

The flow pattern in Figure 3.10B was obtained with the single heater (Figure 3.1C) turned on, namely the single heating (SH) mode. The SH mode generated one pair of counter-rotating vortices symmetrically positioned along the chamber center where the single heater was located. The number of vortices increased when we used the dual heater, namely the dual heating (DH) mode. The DH mode generated two pairs of counter-rotating vortices (Figure 3.10C), which were also symmetric along the chamber center. As shown in Fig 3.10B and 3.10C, the pathlines formed nearly closed loops, where the starting and ending points of each loop are only slightly different. When the single and dual heaters were alternatively turned on and off, we could obtain new flow patterns (Figure 3.10D); we refer to this mode as the alternating heating (AH) mode.

The temperature of the chamber was measured using two resistive-type temperature-sensors integrated in the microfabricated heating-instrument. The temperature data reasonably represent the temperature distribution according to our theoretical simulation (Figure 3.3), which indicates that the spatial temperature gradient primarily exists in the

lateral direction and is symmetric about the chamber center. In the SH mode the temperature is high at the center of the chamber, whereas in the DH mode the temperature is low at the same position (Figure 3.11). The flow patterns of the SH and DH modes (Fig. 3.10B and 3.10C) are affected by the temperature gradient: the fluid moves up in the hot temperature regions near the activated heaters, and moves down in the cold regions. Although we found that thermal expansion deflected the membrane

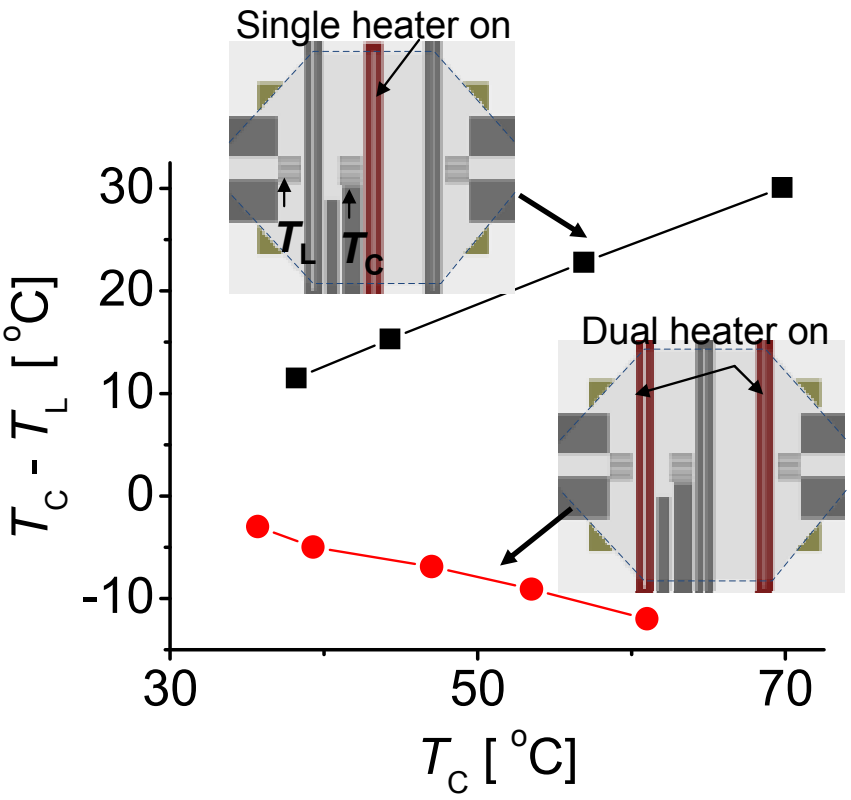

Figure 3.11. Temperature gradient in the chamber. T_C and T_L are the fluid temperatures measured at the temperature sensors of the center and the left of the chamber-region, respectively.

at the bottom of the microfluidic cartridge during the device operation, (Figure 3.12), this deflection did not change the flow patterns in the SH and DH modes because the device was operated without dynamic motion of the membrane and enabled close contact between the microfluidic cartridge and the microfabricated heating-instrument.

To assess the influence of the dynamic deflection of the membrane resulting from the temperature change on the AH mode operation, we have performed an additional experiment using the single heater, where we intentionally apply a very slow single thermal cycle (4 second cooling and 1 second heating). This cycle can be considered to a quasi-static thermal process with a sufficiently long cooling time. This long

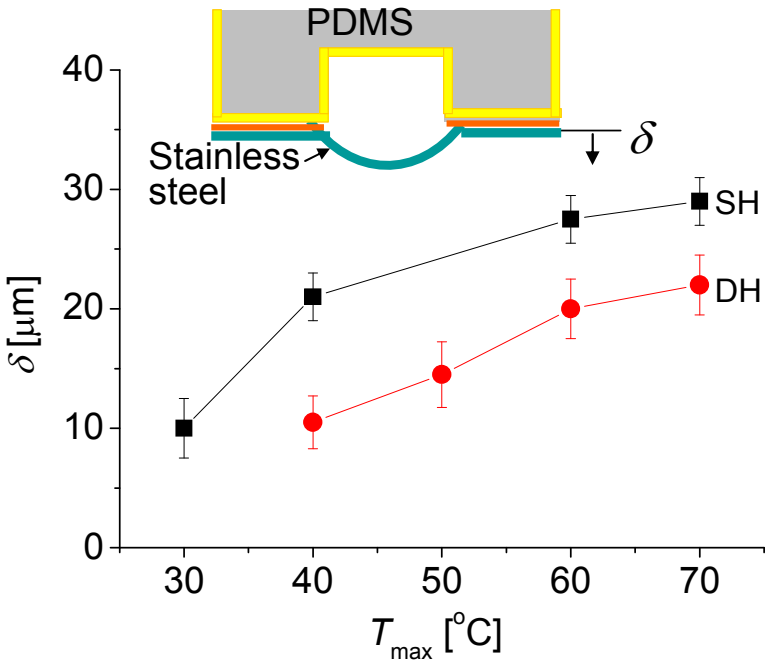

Figure 3.12. Maximum static membrane deflection, δ, due to the thermal expansion. The static deflection was measured by a 3-D surface profiling system (NewView 5000, Zygo).

cooling time enables us to see the maximum drift of micropaticles (Figure 3.13A) until they stop when the membrane motion becomes stationary at the end of the cooling process. The inset of Figure 3.13A shows that a single fluorescent micropaticle drifts laterally during the 4 sec cooling cycle, stops at the highest intensity point at the end of the cycle, and then tends to move upwards upon heating as a result of the motion of the membrane acting like a pump. More specific, the microparticles move ~50 μm laterally at cooling of T_{max} from 60 ^{o}C to room temperature as the membrane moves ~ 27 μm upward (Figure 3.12). We have verified through repeating this cycle that this lateral drift of the microparticles is consistently caused by the membrane movement under the quasi-static thermal condition. It follows that the image distortions resulting from the particle drifts should indicate the existence of the membrane displacement during the thermal cycles. Then, we next obtain a new particle trajectory image when applying a high-speed cycle with a short cooling time. Figure 3.13B shows smaller lateral drifts (< 15 μm) of microparicles when cooling time becomes shorter (0.7 second cooling and 4.3 second heating per cycle with 4 cycles), which suggest a reduction in the membrane motion. At this cooling condition, a change in T_{max} is 25 ^{o}C (cooling from 60 to 35 ^{o}C), which is expected to yield a membrane displacement less than 10 μm from our static measurement in Fig. 3.12. In the AH mode, the movement of the membrane per cycle is expected to even smaller as the change in T_{max} becomes smaller when the single and dual heaters are alternatively turned on. This is verified by the fact that the trajectory image taken for the AH mode (Fig. 3.10D) shows no significant distortions. In any case, the dynamic membrane motion serves favorably as it provides additional driving force for micromixing.

The average flow speeds (Figure 3.14A and 3.14B), which were measured for each single loop (Figure 3.10B and 3.10C), polynomially grow with the temperature. At a given geometry the flow speed (V) is influenced by thermal expansion coefficient (β), temperature gradient (ΔT), and kinematic viscosity (ν) of the solution as $V \propto \beta \Delta T / \nu$ [58]. Increasing the temperature of the chamber causes both ΔT and β to increase but ν to decrease. Thus, the net result of heating the solution is the rapid increase of the flow

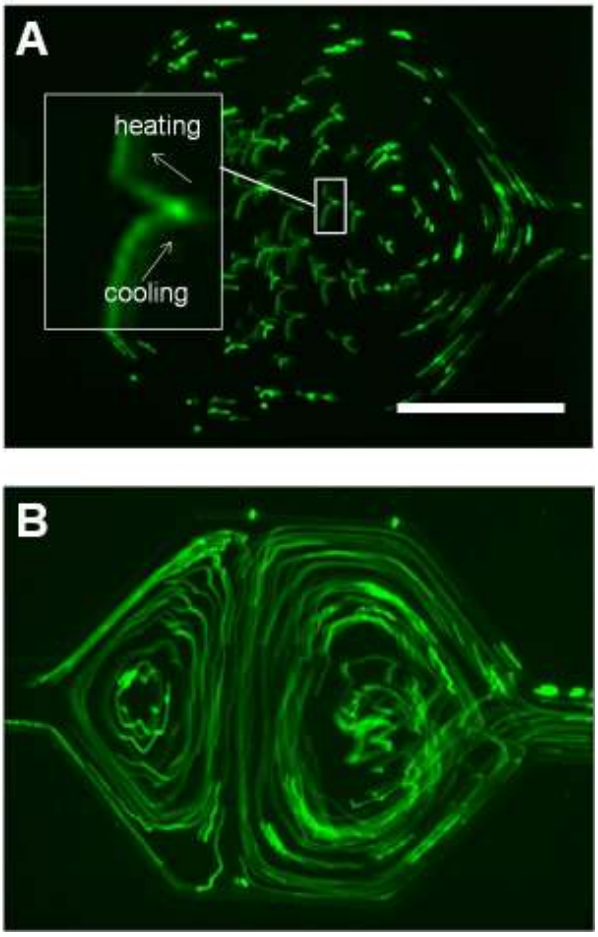

Figure 3.13. Flow trajectories of fluorescent microparticles to show the influence of membrane deflection by the single heater. The maximum temperature of the chamber was ~60 ^{o}C. (**A**) Single cycle of cooling-heating for a time duration of 5 sec. The chamber was cooled for 4 sec and was heated for 1 sec. The inset shows the pathline of a single microparticle. (**B**) Multiple cycles of cooling-heating for time duration of 20 sec. In each cycle, the chamber was cooled for 0.7 sec and was heated for 4.3 sec. Scale bar, 1 mm

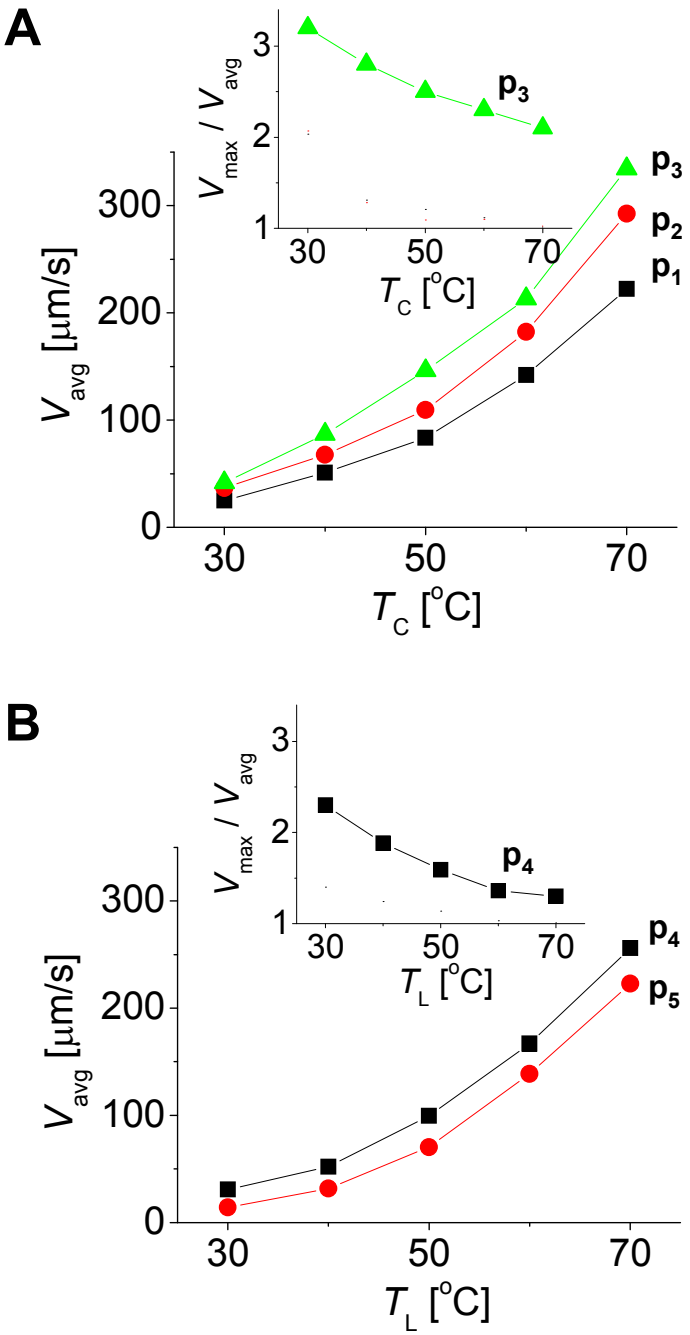

Figure 3.14. Flow speed of the fluorescent microparticles in Fig. 3.8B and 3.8C. The Single heater is turned on in (**A**) and the dual heater is turned on in (**B**). V_{avg} is the flow speed averaged over the individual microparticles in a single loop, whereas V_{max} is the maximum flow speed at the same loop.

speed. To support this trend theoretically, we have normalized the data in Figure 3.14A and 3.14B, and compared it with the following equation in each temperature:

$$V_{\text{avg\_norm}} = \frac{\beta \Delta T / \upsilon}{(\beta \Delta T / \upsilon)_{70\text{oC}}} \tag{3.14}.$$

As shown in Figure 3.15, the measured speed trend is in good agreement with equation (3.14), thus verifying the effect of β, ΔT, and ν on flow speed.

In addition, the flow is accelerated near the heaters, yielding maximum speed near the heating region. The maximum speed at the single loop is several times (1.3 – 3.1) faster than the average speed at the single loop (Figure 3.14A and 3.14B Insets). Additionally, the effect of temperature rise on diffusion was calculated to be minor. Einstein-Stokes equation [64], which depicts the diffusion of spherical particle in a liquid, shows that diffusion coefficient (D) is linearly proportional to temperature (T), i.e. $D \propto T$. Thus, diffusion coefficient changes less than 23% when the temperature increased from 27 to 93 °C (300 to 368 K). Moreover, the diffusion length (L) increases only 11% at this condition because $L \propto D^{1/2}$. A theoretical calculation shows that diffusion is highly influenced by the molecular size rather than the temperature (Figure 3.16).

Both the SH and DH modes can generate vortex flow patterns for mixing. However, with these modes alone, the vortices in each closed loop do not overlap and the flow is relatively fast only in a small region of the chamber near each activated heater. In contrast, mixing can be significantly enhanced when we use the AH mode (Fig. 3.10D): the device operation in the AH mode can overlap the pathlines of different closed loops and increase the fast flow regions by the continuous alternation of the SH and DH modes.

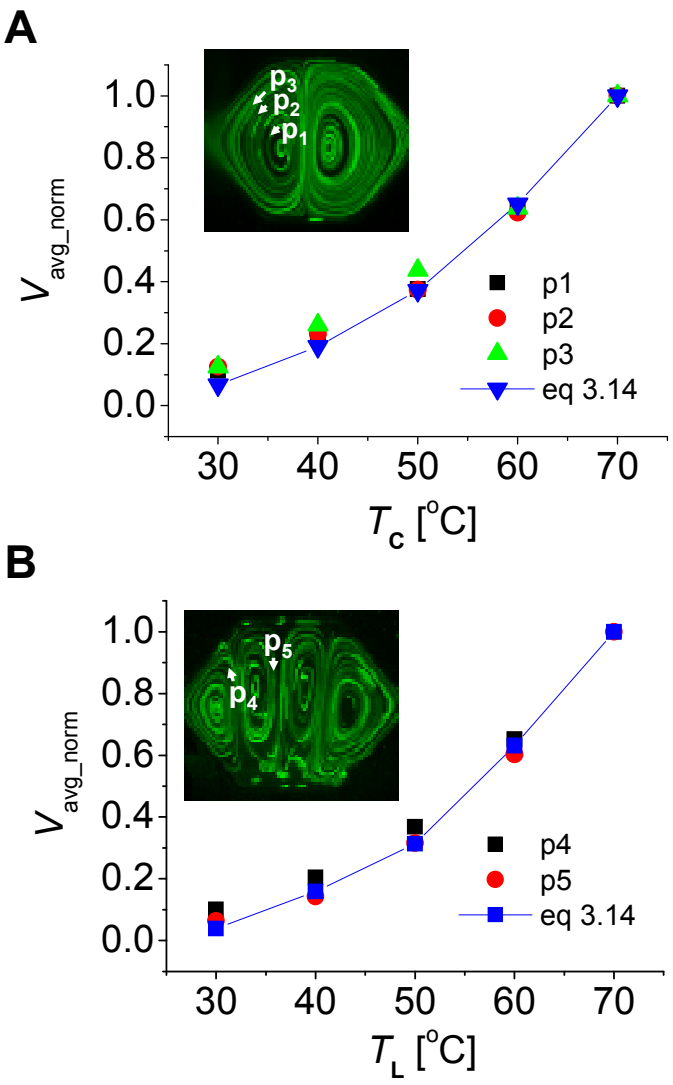

Figure 3.15. Normalized flow speed V_{avg_norm} of the fluorescent microparticles in Fig. 3.14. For the calculation using equation 3.14, we have assumed the solution as pure water.

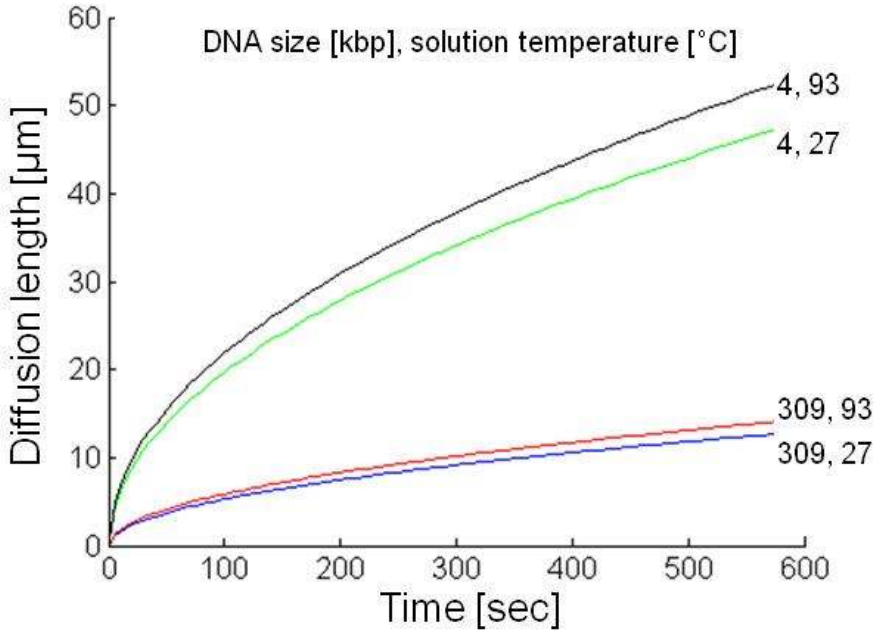

Figure 3.16. Influence of temperature on diffusion. The diffusion coefficients of TOTO-1 stained bacteriophage DNA at 27 °C are measured as 0.14 $\mu m^2/s$ for 309 kbp and 1.94 $\mu m^2/s$ for 4 kbp [65].

In previous studies of flow-generation by natural convection, the flow patterns had only one [66–69] or two [70] vortices, which would be insufficient for micromixing according to results in our following study on micromixing.

3.4.2. Micromixing.

We characterized the micromixing process in the microfluidic chamber using a fluorescent dye. Two solutions were first injected into the two inlets using pipettes, and then their streams filled each channel, merged at the junction, and finally reached the

microfluidic chamber (1 μL, 180 μm-heights) by capillarity. The essential part of the capillarity-based stream control is the merging process at the junction; we previously showed that the merging process can be passively controlled by setting an appropriate aspect-ratio of the microchannels [71].

When the streams reached the outlet, heat was applied for inducing the micromixing. The micrographs in Figure 3.17 show the time evolution of mixing process in each heating mode. When the heaters were turned on, the flows in the SH and DH modes started to move up along the heaters. The flow motion outside the heating region was, however, relatively slow, and individual flows rotated only along specified paths. With this flow behavior, the mixing process was not completed within 36 s. In contrast, micrographs in the AH mode (Figure 3.17) show that the two distinct solutions were greatly homogenized in the same amount of time.

We quantified the degree of mixing as a function of time using the standard deviation, σ. The decrease in the values of σ in Figures 3.18A to 3.18C with time indicates the progression of the micromixing processes. In the SH and DH modes, we applied constant voltages with a step profile; thus the temperatures gradually increased and reached final maximum values (Insets in Figures 3.18A and 3.18C). In the AH mode, we alternatively applied constant voltages to the single and dual heaters. The alternating period of the AH mode was selected based on the flow time for which each fluorescent solution arrives at the top wall of the chamber after the initial stage of heating. As shown in Figure 3.19, the mixing time became faster at higher temperature. However, we found that the mixing using the AH mode at 37^{o}C was even faster than any other cases observed in the SH and

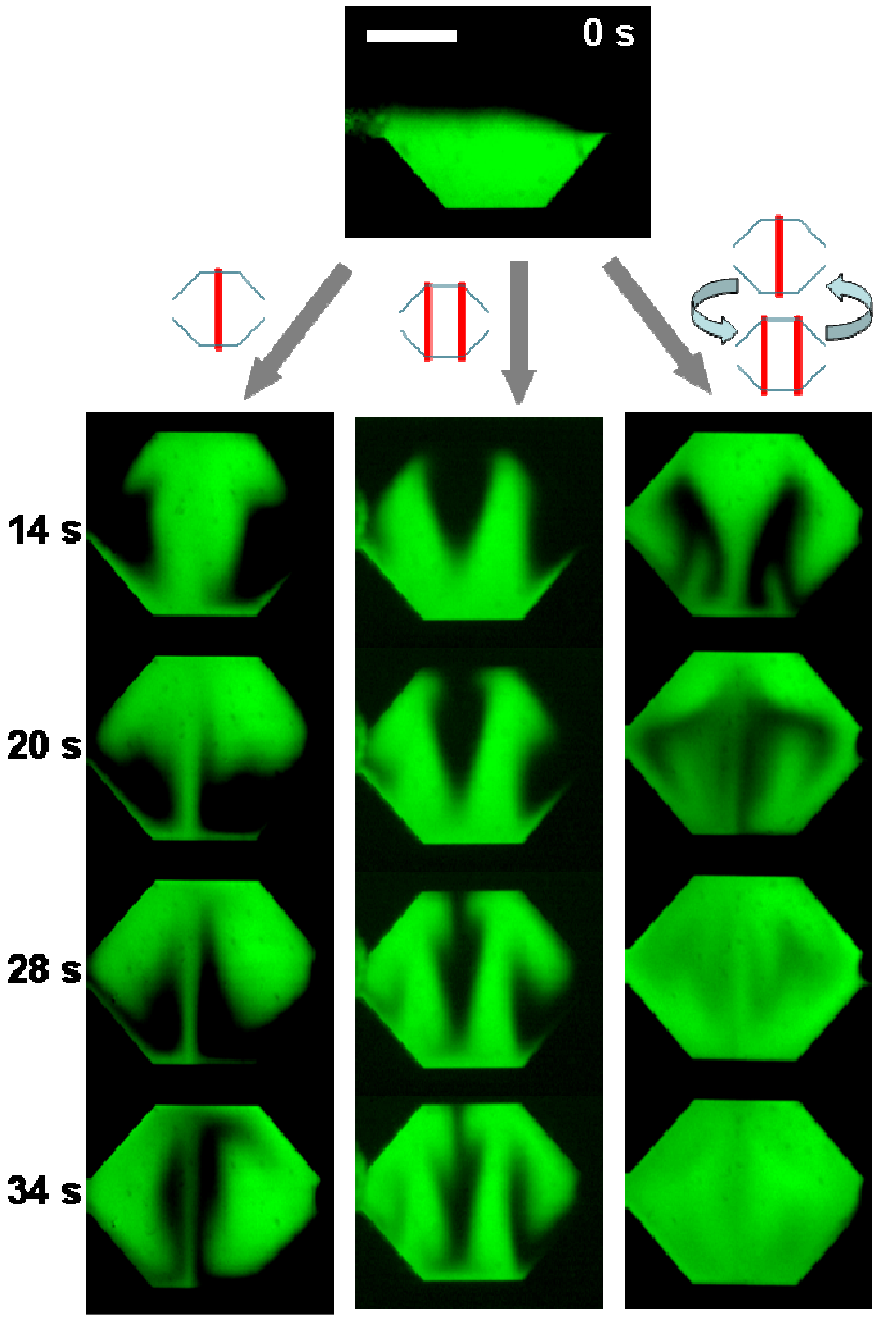

Figure 3.17. Micromixing device performance in different heating modes. (**A**) Time evolution of micromixing in the single heating (SH), dual heating (DH), and alternating heating (AH) modes. The values of T_{max} are 57, 48, and 56°C in SH, DH, and AH modes respectively. Scale bar, 1 mm.

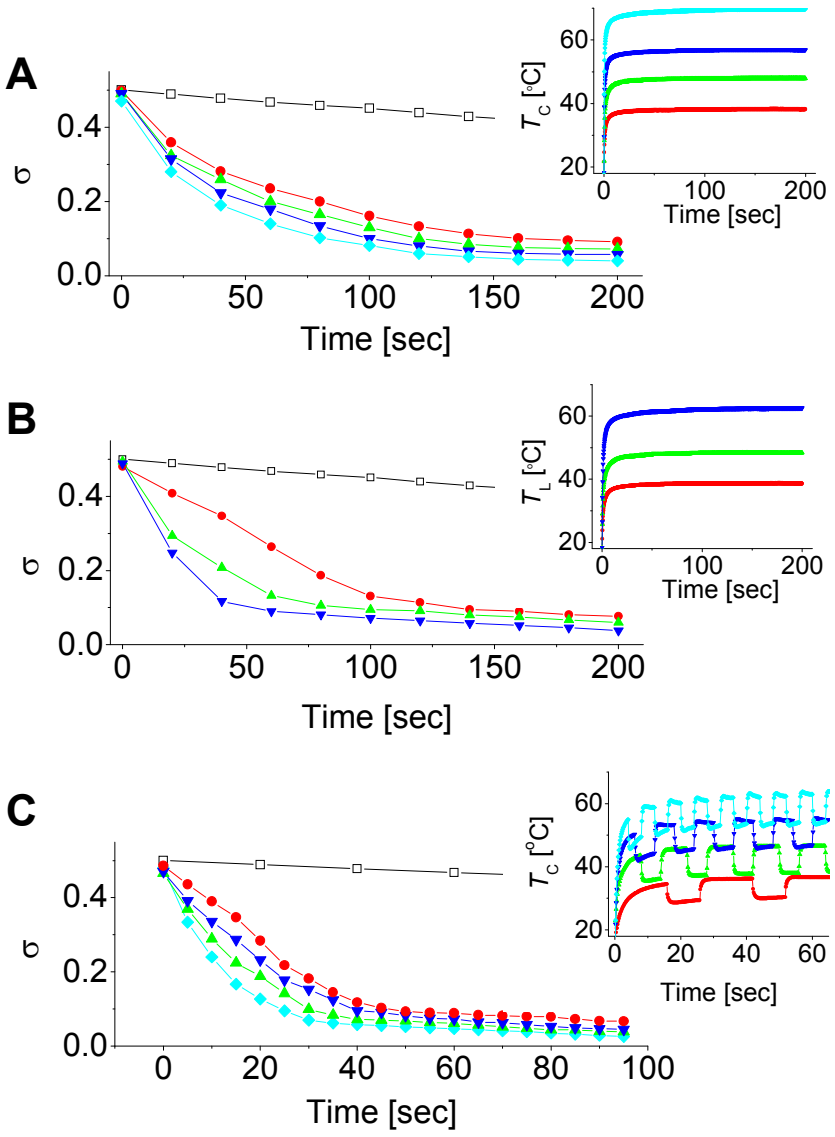

Figure 3.18. Time variation of the standard deviation, σ, from the measurement of fluorescent intensity. Shown are the SH mode in (**A**), the DH mode in (**B**) and the AH mode in (**C**). The unmixed case is σ = 0.5 and the perfectly mixed case is σ = 0. The Insets show the fluid temperatures measured using the temperature sensors in Fig. 3.4 (T_L or T_C) whose line colors correspond to those in the σ vs time plots. For comparison, mixing due to pure microfluidic diffusion is shown with the points (□).

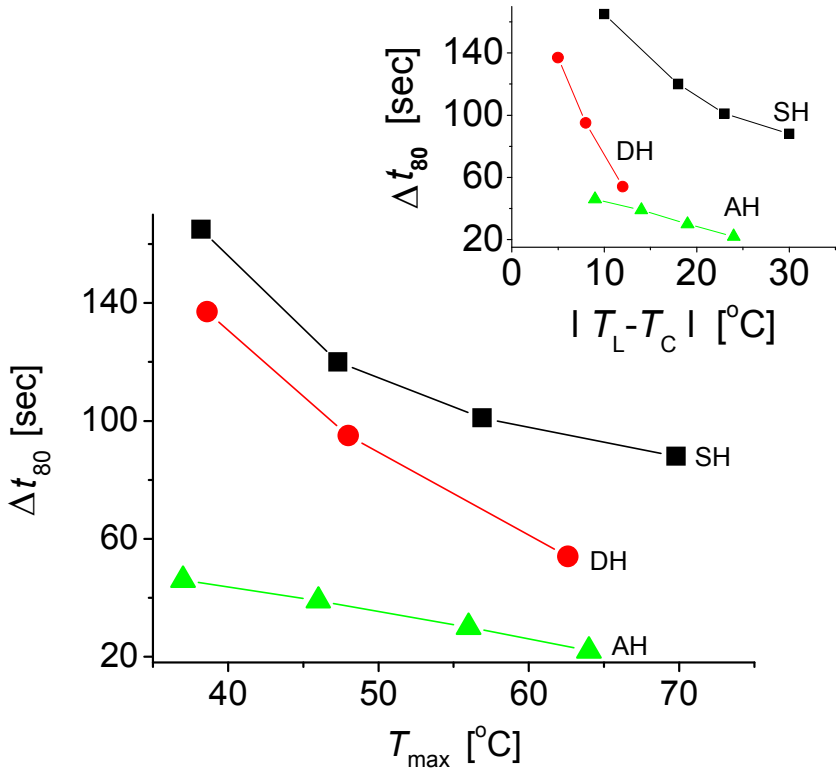

Figure 3.19. Quantitative comparison of mixing performance in the SH, DH, and AH modes. Δt_{80} is the time at which the mixing process is 80% completed, which is determined from the points at $\sigma = 0.1$ in Figure 3.18(A–C), is the time to achieve 80% mixing and T_{max} is the maximum fluid temperature measured by the temperature sensors in Figure 3.11. The inset shows Δt_{80} in each mode with respect to the temperature gradient, $| T_L - T_C |$.

DH modes, thus clearly verifying the efficiency of the AH mode-based operation for micromixing. In the AH mode, a sufficient degree of mixing can be achieved within a few tens of seconds per one microliter volume of solutions. This mixing performance is comparable to the highest performance reported in previous studies (see the Table 1 of reference 72), which took one to several hundreds of seconds per one microliter of solution. It should be noted that these studies still used complex channel geometries or active components that are likely difficult to integrate in microfluidic networks. Even a

few studies demonstrated integration of mixers in microfluidic networks, these micromixers typically faced limited performance with several hundreds or thousands of seconds per one microliter [15, 23, 24].

3.4.3. PCR

To prove the single-chamber micromixing and reaction concept, we finally demonstrated autonomous PCR of a DNA fragment from the influenza viral strain A/LA/1/87, following the sequence of sample transport and micromixing. To ensure the autonomous operation, we pre-programmed the heating instrument with a computer prior to the experiment. After mixing the solutions in the AH mode, the PCR was performed for three different total cycle numbers of 10, 20, and 30 (Figure 3.20B). The heating area for the PCR was 3.7 times larger than the contact area of the chamber, thus making the temperature-distribution uniform such that $T_C - T_L < 2°C$ even at 94°C. Despite the relatively large heating surface, our system still maintained fast thermal response (Figure 3.20B inset). Owing to the use of the stainless-steel membrane (thermal conductivity: 13 W/Km, thickness: 8 μm) as the bottom cover of the microfluidic cartridge, heat conduction is confined only at the chamber region. Also, the thin membrane consisting of a 10 μm-thick Pyrex-oxynitride composite in the microfabricated heating-instrument enables spatially confined heat conduction to the chamber in the microfluidic cartridge, thus enabling fast heating and cooling rates. After the whole PCR process was finished,

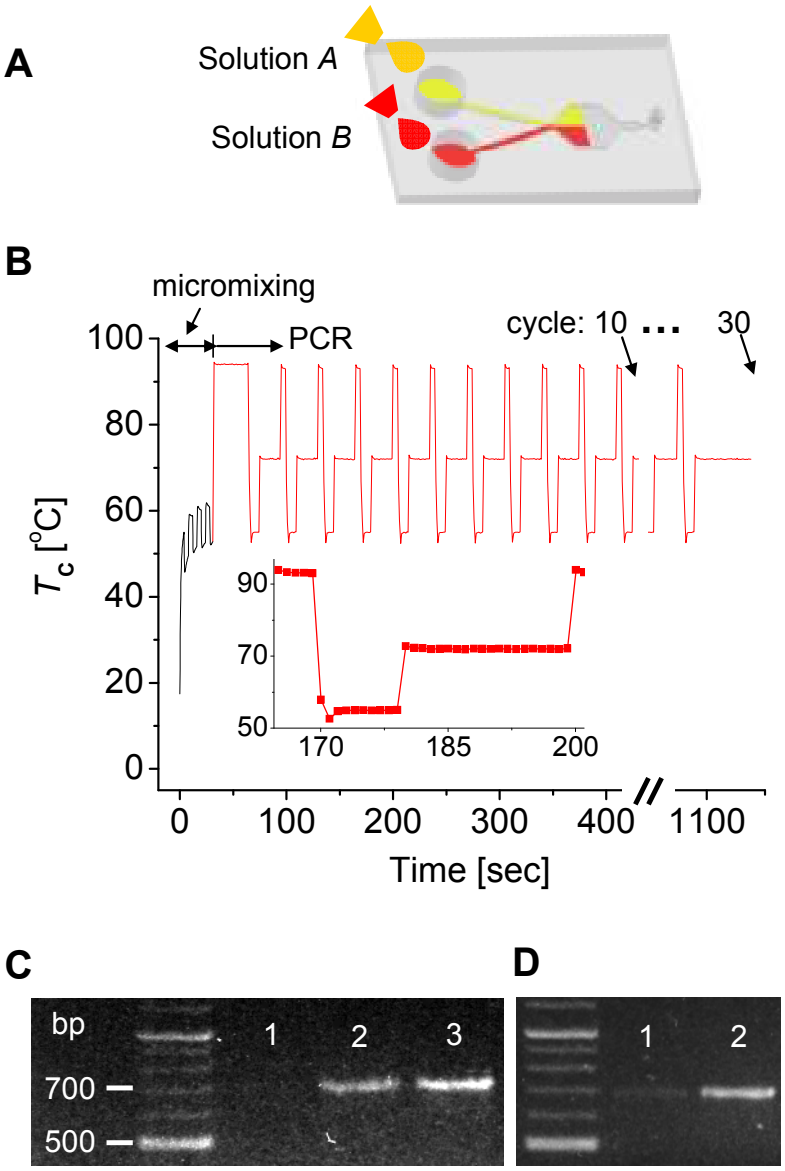

Figure 3.20. Natural convection-driven micromixing and PCR in a single microfluidic chamber. (**A**) Pumpless sample transport by capillarity. Solution A is a DNA template and solution B is a reaction mixture of primer, enzyme, and dNTPs. (B) Time sequence of heating used for the AH mode micromixing and the PCR process. The inset shows a single heat cycle of the PCR process with a time interval of 1 sec between the adjacent data points. PCR-based amplification of a DNA fragment from the influenza viral strain A/LA/1/87 is performed for 10, 20, and 30 cycles. (**C**) Influence of PCR cycles. Lanes 1, 2, and 3 correspond to the amplified PCR products after the microfluidic mixing and the subsequent 10, 20, and 30 PCR cycles, respectively. (**D**) Improvement of PCR by microfluidic mixing. Both lane 1 and lane 2 are the amplified PCR products after the 20 cycle. However, lane 1 is a control without a microfluidic mixing process at AH mode.

the PCR products were extracted and then detected using agarose gel-electrophoresis outside the cartridge. Figure 3.20C shows that the influence of PCR cycles on the signal enhancement of PCR products. Figure 3.20D demonstrates the necessity of our microfluidic mixer for the subsequent PCR process; without a microfluidic mixing process, the signal from the amplified PCR products was much weaker. Both figure 3.20C and 3.20D verify that DNA sample was successfully amplified by our micromixing and PCR process.

3.4.4. Technological Advantages of the System

Our results prove remarkable advantages of the approach taken here for practical use. Our system can achieve both micromixing and PCR in a single chamber without adding any other microfluidic components. The single-chamber micromixing approach is broadly applicable in a wide range of biochemical reactions that require heating processes at $40^{o}C - 135^{o}C$, such as cell lysis [73], DNA hybridization [74], protein digestion [75], and biosynthesis [76] as well as PCR [77]. In conventional microfluidic systems, achieving biochemical reactions normally requires additional heating chambers besides micromixing channels, thereby adding more complexity to the system. Without sacrificing fast thermal response, the heaters and temperature sensors are designed as modular components originally separated from the microfluidic cartridge and integrated on the surface of the microfabricated heating-instrument. Although this type of system enables repeated use of the heating instrument and makes a microfluidic cartridge truly disposable, a previous study [78–80] employing this approach showed relatively slow thermal response due to the large thermal mass of the system, which resulted in lower

heating and cooling rates of 13.4 °C/s and 6.4 °C/s for a 280 nL reaction volume, respectively. In contrast, our system yields a heating rate of 40 °C/s and a cooling rate of 35 °C/s for a 1 μL reactionvolume, thus greatly saving the transient time. For example, our system requires ~60 s transient time for 30 PCR cycles, whereas previous studies [78–80] need > 280 s transient time. Thus our system saves more than 220 s in 30 PCR cycles and, as a result, total PCR reaction time reduces from 1400 s to 1100 s in our PCR application of the 680 bp influenza viral strain A/LA/1/87.

Thermal responses of several studies are summarized in Table 3.1. Because of the difference in the chamber volume among these studies, heating and cooling rates in the table are not the reasonable parameters that allow us to directly compare the thermal responses. Instead, we use the time constant due to the peripheral thermal mass (τ_{peri}) that excludes the effect of the thermal mass of the chamber solution. For the calculation of τ_{peri}, we can decompose the total time constant (τ_{tot}) of each device as follows:

$$\tau_{tot} = \tau_{chamber} + \tau_{peri} = (C_{chamber} + C_{peri})R \tag{3.15}$$

where $\tau_{chamber}$ is the time constant due to the chamber solution, and $C_{chamber}$ and C_{peri} are the thermal mass of the chamber solution and its periphery, respectively. R is the thermal resistance due to the membrane in the chamber. For equation 3.15, we assume heat transfer dominantly occurs through the membrane because thermoelectric cooler is used under the membrane for cooling. With the given data for $C_{chamber}$ and R, we can obtain the value of τ_{peri} from equation 3.15 and the result is shown in Table 3.1. Notably, τ_{peri} is

at least 12 times greater than $\tau_{chamber}$ in any studies, thus showing the importance of minimizing the influence of the peripheral component.

Table 3.1. Summary of studies using heating instrument and cartridge

Reference	Heating & cooling rate [$^{o}C\ s^{-1}$]	Chamber volume [μL]	Total time constant [s]	Time constant due to chamber solution [s]	Time constant due to peripheral thermal mass [s]
Our work	40, 35	1	1.4	5×10^{-4}	1.4
Belgrader *et al* [78]	6, 5	25	13.5	2×10^{-1}	13.3
Liu *et al* [79]	8, 5	38	13.5	1	12.5
Easley *et al* [80]	13, 6	0.3	11.2	3×10^{-1}	10.9

thermal mass. Our study has almost 10 times smaller τ_{peri} than other studies. This result can be attributed to the small thermal resistance of the stainless steel membrane in our study (thickness of 8 μm and thermal conductivity of 14 W/Km), compared to the relatively large thermal resistance of the membranes in other studies (polymers or glass, thickness of 30-700 μm and thermal conductivity of 0.2-2 W/Km). Besides, as membrane becomes thicker, it yields additional thermal mass, thus increasing τ_{peri}; this effect also explains relatively large τ_{peri} in other studies. Therefore, even when the larger chamber volume is used in our system, we expect faster thermal response compared to other studies.

The sample transport in our device is purely induced by capillarity, which eliminates the necessity of pumps for micromixing. In comparison, even the simple passive mixers developed in many of previous studies use pumps, rendering the lab-on-a-chip system-integration difficult with the added complexity of the instrument setting.

CHAPTER IV

Microthermal Modulator for GC×GC Applications

4.1 Concept

Comprehensive two-dimensional gas chromatography (GC×GC) is an analytical technique used to separate and detect the components of complex mixtures of volatile organic compounds [27, 28]. Unlike standard GC, which uses a single column for vapor separation, GC×GC couples a first-dimension column to a relatively short second-dimension column whose retention properties are complementary to those of the first-dimension column. Through a junction-point modulator between the two columns (Figure 4.1A), mixture components separated on the first-dimension column are focused and reinjected as a series of narrow pulses onto the second-dimension column. This results in an increase in peak capacity (i.e., the number of compounds that can be separated in a given analysis) and in sensitivity as a 2-D chromatogram is produced [28].

In this study, we report on the design, fabrication, modeling, and preliminary testing of a µTM (Fig. 4.1B) that incorporates two series-coupled serpentine Pyrex-on-Si microchannels (stages) that are sequentially cooled to trap and focus vapors and then

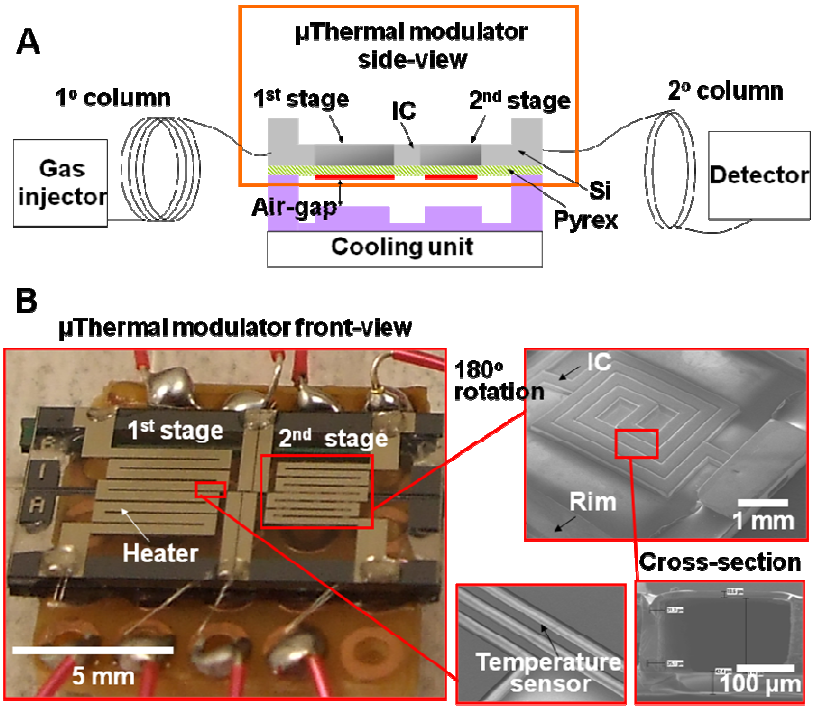

Figure 4.1. Miniaturized thermal modulator (µTM). (**A**) Schematic of GC×GC system incorporating the µTM. Key components of the µTM are two-stage silicon-microchannels, Pyrex membrane, and interconnection channels (ICs). A Si-spacer maintains the air-gap between the µTM and the cooling unit. The cooling unit has a thermoelectric cooler and a fan cooler. The thermoelectric cooler keeps the temperature of the µTM approximately at -55°C when there is no heating in the µTM stages. We vary the size of the Pyrex membrane, the air gap, and the IC to explore the optimal device performance. (**B**) Photographs of µTM. Each stage has serpentine microchannels (250 µm-width and 140 µm-depth) on its back side, on-chip microheaters and temperature sensors on its front side. The microchannel lengths on the first and second stages are 4.2 cm and 2.8 cm, respectively. A rim structure is used to reinforce the mechanical strength of the µTM. (**C**) Control volumes for the lumped thermal model. Each thermal mass includes the Si layer and the corresponding Pyrex membrane area
heated to desorb them.

We adopt two-stage modulation where analytes trapped in the first stage are thermally released into the (cooled) second stage for additional focusing prior to injection into the second-dimension column. In addition, the second stage is not heated until the first stage has cooled to a temperature sufficient for trapping. This alternating heating and cooling of each stage helps to avoid 'breakthrough', whereby sample is lost due to incomplete trapping during thermal transitions, which is a potential problem with single-stage modulator designs [41]. An emphasis is placed on three critical design parameters that govern the heat capacity of the device structure and the rate at which heat energy is transported between stages and from each stage to the environment: (1) the thickness of the Pyrex membrane that seals the silicon microchannels of the μTM; (2) the air gap between the cooling unit and the μTM; and (3) the interconnection channel (IC) that connects the two stages and the rim. We explore the effects of varying these parameters on the device performance using a lumped heat transfer model, where the trade-off between the heating-cooling cycle speed and the power requirement as well as the thermal crosstalk between the two stages are carefully considered. Preliminary results demonstrating the modulation and sensitivity enhancement of a sample mixture of hexane, heptane, and octane vapors are presented.

4.2 Thermal Modeling

Temperature uniformity within a thermal modulator is critical to generate sharp sample plugs, which eventually enhance peak capacity and sensitivity. Also, implementing uniform temperature is important on the thermal analysis because it makes the analysis simple. Here, we firstly explore a method to enhance temperature uniformity using finite element analysis. Then, we perform lumped thermal modeling, which greatly simplifies the thermal analysis, based on the uniform temperature.

4.2.1. Finite Element Analysis for Uniform Temperature

Finite element analysis was also performed to predict the temperature profile within the stage channel at the heating operation. Figure 4.2 shows the results for two different device configurations, which place the heater on either the top side or the bottom side relative to the thermoelectric cooler (TEC) surface. The bottom-side configuration yields significantly uniform temperature profile with a variation $\Delta T < 0.7$ ºC, thus leading to good device reliability and sample concentration performance. Based on this finding, the bottom-side heating configuration is selected for the μTM design.

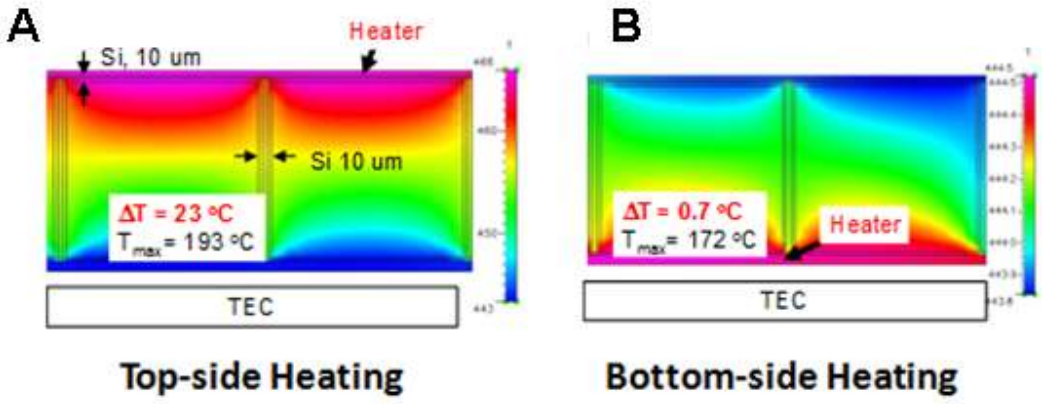

Figure 4.2. Finite element analysis of stage channel temperature profile for (**A**) top-heating configuration and (**B**) bottom-heating configuration.

Thermal conduction through the Pyrex membrane was neglected in the analysis. This conduction through the Pyrex membrane in conjunction with the conduction to the Si spacer was found to be the fundamental sources of temperature gradient inside the μTM channel. To address the problem of a significant temperature gradient inside the μTM channel, we could modify either the design of Si spacer or Pyrex membrane. However, from the device fabrication viewpoint, modifying the Pyrex membrane is difficult; so the modification has been focused on the Si spacer design. Based on the computational simulation of heat transfer shown in Figure 4.3, grooves with a 200 μm height and a 120 μm width to the Si spacer have been introduced. The result of the simulation indicates that these grooves make the temperature inside the μTM channel uniform, yielding a negligible difference between the maximum and minimum temperatures occurring at the center and edge of the μTM chamber, respectively.

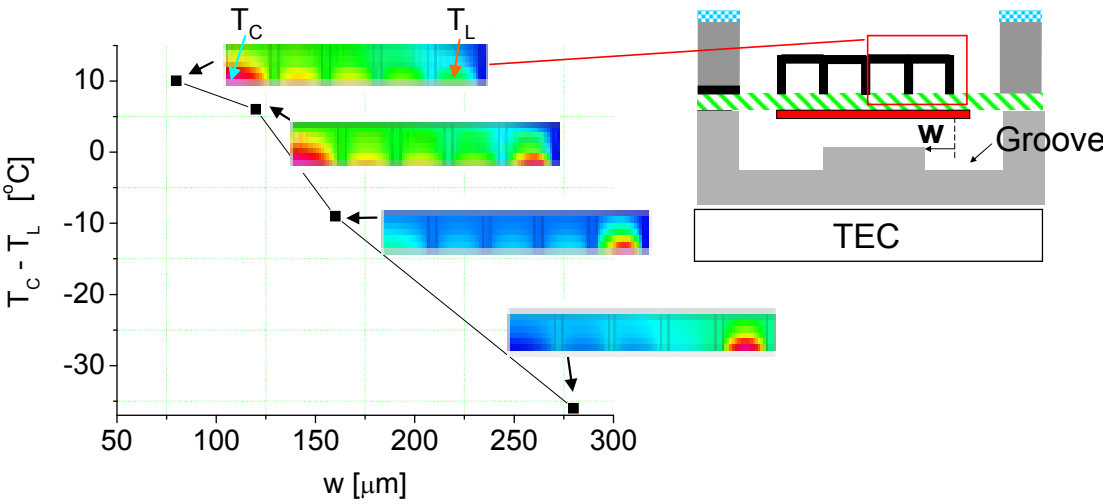

Figure 4.3. Finite element analysis for temperature uniformity using a Si spacer with grooves.

4.2.2. Lumped Thermal Modeling

We developed a series of equations to describe the thermal response of each stage and the thermal crosstalk between the stages. To solve the ordinary differential equations, we used the ode45 solver in MATLAB (The MathWorks, www.mathworks.com). The governing equations were obtained from a balance among energy rates (unit: W), accounting for changes in energy storage and heat transfer due to conduction, natural convection, and radiation. We used the lumped thermal model for each stage and the rim (Figure 4.4), meaning that three control volumes. The energy rates consist of the change of energy storage, conduction, convection, and radiation per unit time. We define the heat transfer as positive when the heat comes into the control volume. The resulting equations are coupled as follows:

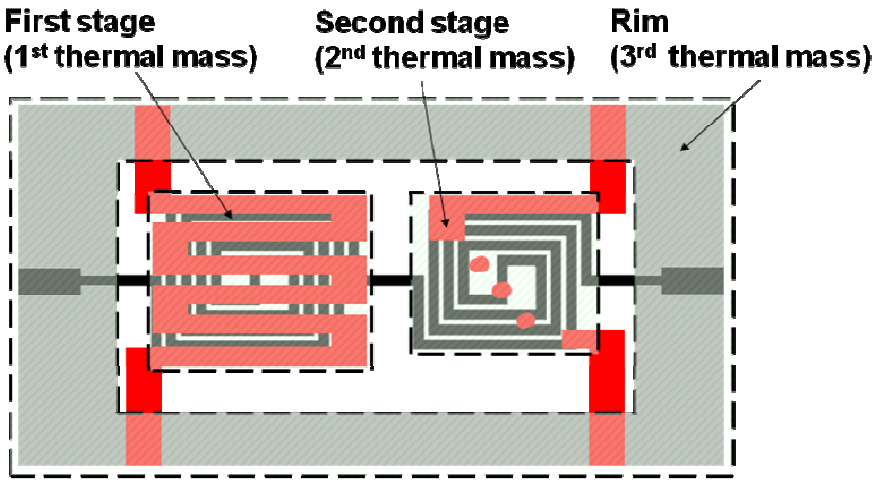

Figure 4.4. Control volumes for the lumped thermal model. Each thermal mass includes the Si layer and the corresponding Pyrex membrane area.

$$\dot{E}_{1\_sys} = \dot{E}_{1-TEC} + \dot{E}_{1-3} + \dot{E}_{1-2} + \dot{E}_{1\_gen} + \dot{E}_{1\_conv} + \dot{E}_{1\_rad} \tag{4.1}$$

$$\dot{E}_{2\_sys} = \dot{E}_{2-TEC} + \dot{E}_{2-3} + \dot{E}_{2-1} + \dot{E}_{2\_gen} + \dot{E}_{2\_conv} + \dot{E}_{2\_rad} \tag{4.2}$$

$$\dot{E}_{3\_sys} = \dot{E}_{3-TEC} + \dot{E}_{3-1} + \dot{E}_{3-2} + \dot{E}_{3\_conv} + \dot{E}_{3\_rad} \tag{4.3}$$

where the numbers (1, 2, and 3) in the subscript correspond to the first stage, the second stage, and the rim, respectively. $\dot{E}_{i\_sys}$ (i = 1, 2, 3) is the rate of energy storage for each thermal mass (the first stage, the second stage, and the rim) and is expressed as follows:

$$\dot{E}_{i\_sys} = (\rho C_p V)_i \frac{dT_i}{dt} \tag{4.4}$$

$$(\rho C_p V)_i = (\rho C_p V)_{Si\_i} + (\rho C_p V)_{Pyrex\_i} \tag{4.5}$$

where ρ, C_p, and V are the density, the specific heat capacity, and the volume of each material (Si and Pyrex), respectively. T_i and t are the temperature of the ith thermal mass and time, respectively. $\dot{E}_{i\text{-}TEC}$ is the conductive heattransfer between the ith thermal mass and the thermoelectric cooler (TEC):

$$\dot{E}_{i\_TEC} = \frac{k_{air} A_{i-TEC}}{L_{air}} (T_i - T_{TEC}) \tag{4.6}$$

where k_{air} is the thermal conductivity of air (0.0294 W m^{-1}K^{-1}). $A_{i\text{-}TEC}$, L_{air} , and T_{TEC} are the facing area of the ith thermal mass to the TEC, the air-gap, and the TEC temperature, respectively. $\dot{E}_{i\text{-}j}$ (i, j = 1, 2, 3, but i ≠ j) is the conductive heat transfer between thermal masses:

$$\dot{E}_{1\text{-}2} = -\frac{k_{Si} A_{IC}}{L_{IC}} (T_1 - T_2) - \frac{k_{Pyrex} A_{1\text{-}2\_Memb}}{L_{IC}} (T_1 - T_2) \tag{4.7}$$

$$\dot{E}_{1\text{-}3} = -\frac{k_{Si} A_{IC}}{L_{IC}} (T_1 - T_3) - \frac{k_{Pyrex} A_{1\text{-}3\_MembIC}}{L_{IC}} (T_1 - T_3) - \frac{2k_{Pyrex} A_{1\text{-}3\_Memb}}{L_{1\text{-}3\_Memb}} (T_1 - T_3) \tag{4.8}$$

$$\dot{E}_{2\text{-}1} = -\dot{E}_{1\text{-}2} \tag{4.9}$$

$$\dot{E}_{2\text{-}3} = -\frac{k_{Si} A_{IC}}{L_{IC}} (T_2 - T_3) - \frac{k_{Pyrex} A_{2\text{-}3\_MembIC}}{L_{IC}} (T_2 - T_3) - \frac{2k_{Pyrex} A_{2\text{-}3\_Memb}}{L_{2\text{-}3\_Memb}} (T_2 - T_3) \tag{4.10}$$

$$\dot{E}_{3\text{-}1} = -\dot{E}_{1\text{-}3} \tag{4.11}$$

$$\dot{E}_{3\text{-}2} = -\dot{E}_{2\text{-}3} \tag{4.12}$$

where k_{Si} and k_{Pyrex} are the thermal conductivity of Si and Pyrex (130 W $m^{-1}K^{-1}$ and 1.4 W $m^{-1}K^{-1}$), respectively. A_{IC} is the cross-sectional area of the Si interconnection channel (IC), and L_{IC} is the length of the IC. $L_{1\text{-}3\_Memb}$ and $L_{2\text{-}3\_Memb}$ are the distances between 1-3 and 2-3, respectively. $A_{1\text{-}2\_Memb}$, $A_{1\text{-}3\_Memb}$, and $A_{2\text{-}3\_Memb}$ are the cross-sectional areas of the Pyrex membrane between thermal mass 1and 2, 1and 3, and 2and 3; however they exclude the areas contacting the ICs. $A_{1\text{-}3\_MembIC}$ and $A_{2\text{-}3\_MembIC}$ are the cross-sectional areas of the Pyrex membrane between thermal masses 13 and 2-3, respetively, that are in contact with the ICs. $\dot{E}_{i\_gen}$ is the heat generation by integrated microheaters:

$$\dot{E}_{i\_gen} = V_i^2 / R_i \tag{4.13}$$

where V_i and R_i are the applied voltage and electrical resistance, respectively, at the i^{th} microheater. $\dot{E}_{i\_conv}$ and $\dot{E}_{i\_rad}$ are the heat transfer by convection and radiation, respectively. We assume natural convection for the $\dot{E}_{i\_conv}$ term and also assume that the μTM is a small convex object in a large-cavity environment for the term $\dot{E}_{i\_rad}$. They are expressed as follows:

$$\dot{E}_{i\_conv} = -hA_{Si\_i}(T_i - T_\infty) \tag{4.14}$$

$$\dot{E}_{i\_rad} = -\sigma_{SB}\varepsilon_r A_{Si\_i}(T_i^4 - T_\infty^4) \tag{4.15}$$

where h, σ_{SB}, and ε_r are the natural convection coefficient (10 W $m^{-2}K^{-1}$), Stephan-Boltzman constant (5.67×10^{-8} W $m^{-2}K^{-4}$) and the emissivity of the radiating Si surface

(0.52), respectively. A_{Si_i} and T_∞ are the area of i^{th} thermal mass on the Si surface and ambient temperature, respectively.

4.3. Materials and Methods

This chapter discusses the fabrication and experimental methods for the designed device. Fabrication processing was done at the Lurie Nanofabrication Facility at University of Michigan. Experimental methods include calibration of resistive-type temperature sensors, stationary phase coating of the μTM, temperature control, and peak modulation conditions.

4.3.1 Microfabrication and Assembly

The fabrication process is summarized in Figure 4.5. The first and second stages of the μTM consist of meander-line boron-doped-Si microchannels 4.2 and 2.8 cm long, respectively, with cross-sectional dimensions of 250 (w) × 140 (h) μm and a wall thickness of 30 μm. The IC has the same cross section and wall thickness, and consists of three segments: two that connect each stage to the rim and one that connects the two stages. The three IC segments had the same length, which was varied from 0.5 mm to 1.5 mm in different device designs. Anodically bonded Pyrex glass, either 40 or 100 μm

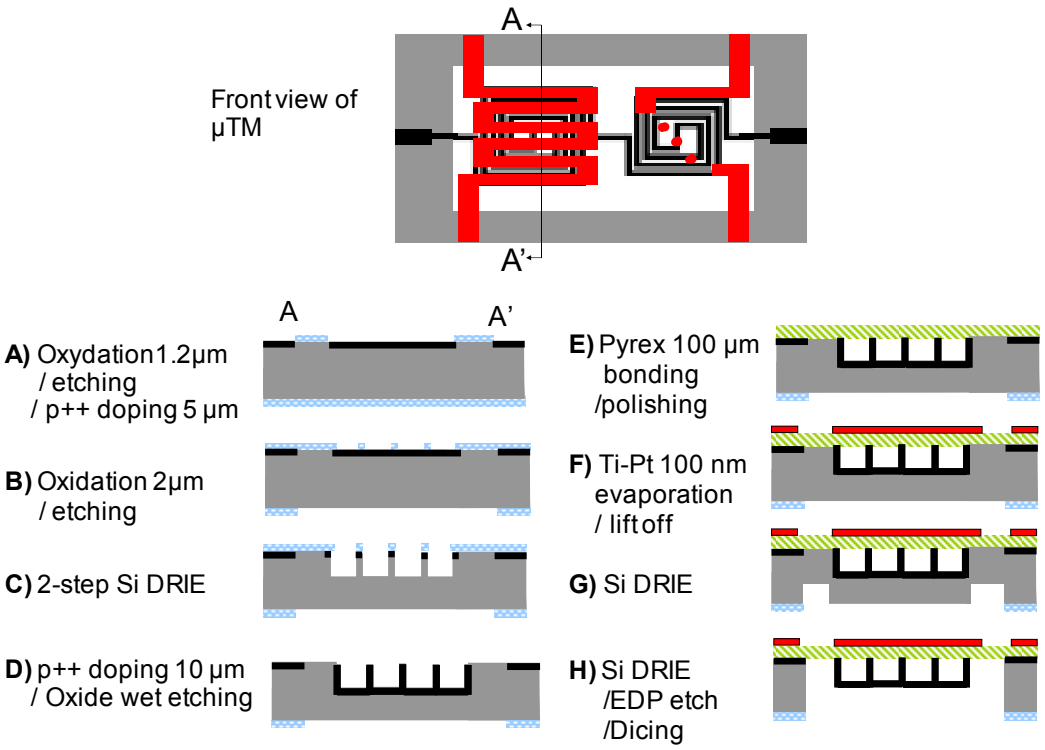

Figure 4.5. Fabrication process flow for the µTM . (**A**) The process was started with a silicon wafer of 4 inches in diameter and 500 µm in thickness. We thermally grew a 1.2-µm-thick oxide layer on the both sides to serve as a diffusion barrier of the boron doping. The backside was covered by photoresist and the frontside was photolithographically patterned to define the microchannels and the oxide was removed by dipping in buffered hydrofluoric acid (BHF). The exposed areas were doped with boron to a depth of 5 microns in a boron diffusion furnace. (**B**) A second thermal oxide layer was grown on both sides of the wafer as a diffusion barrier for the second boron doping. After separate patterning steps on each side of the wafer, the oxide was removed with BHF. (**C**) Microchannels (140 µm-deep and 250 µm-wide) and inlet-outlet ports (400 µm-deep and 400 µm-wide) were formed by two-step Si deep reactive etching (DRIE). (**D**) A second boron doping step was performed to protect the microchannels in the subsequent Si wet-etching process (step **H**) and the frontside oxide was removed (in BHF) in preparation for the anodic bonding process. (**E**) A glass wafer (Pyrex 7740, Sensors Prep Services, 100 µm thickness) was cleaned in sulfuric-acid solution and anodically bonded to the frontside of the wafer. (**F**) Patterned microheaters and temperature sensors (electronbeam evaporated Ti/Pt; 20 nm/100 nm) were then fabricated on the glass layer by a lift-off process in an acetone solution. (**G**) DRIE was used to define the channel areas at the backside of Si wafer. (**H**) The remaining Si around the microchannels was removed by a combination of DRIE and wet-etching with ethylene-diamine-pyrocatechol solution. Finally, the wafer was diced into individual chips.

thick, was used to seal the microchannels. Microheaters and temperature sensors made of

Ti/Pt were patterned on the Pyrex membrane. Microfabricated Si spacers, used to create an air gap (22–63 μm) between the μTM and the top surface of the thermoelectric cooler (SP2394, Marlow industries, www.marlow.com), were precisely aligned with a microscope and bonded with an epoxy adhesive onto the Pyrex membrane; the Si spacers were separately fabricated by a two-step silicon deep reactive ion etching process. Then the μTM was mounted on a printed circuit board and wire bonded for electrical connection.

A thin layer of thermally conductive paste was used to ensure good thermal contact between the Si spacers and the thermoelectric cooler. With a height gauge (Series 192, Mitutoyo, www.mitutoyo.com), the μTM with Si spacers was manually aligned and bonded to the cooling unit. A small axial fan (E1U-N7BCC-03, SundialMicro, www.sundialmicro.com) facilitated heat transfer from the backside of the thermoelectric cooler. Finally, a custom-made chamber was used to seal the μTM.

4.3.2 Stationary-phase Coating of the μTM

Deactivated fused-silica capillaries having 250 μm i.d. and 100 μm i.d. were inserted in the inlet and outlet ports, respectively, of the μTM and secured with high-temperature epoxy (Hysol 1C, Dexter Corp., www.rshughes.com) to form a leak free seal. The internal walls of the μTM microchannels were dynamically coated with polydimethylsiloxane (PDMS, OV-1, Ohio Valley, www.ovsc.com) from a solution (0.10 g/mL in 1:1 pentane/dichloromethane) that also contained a thermally activated cross-linking agent, dicumyl peroxide (1 mg/mL, Aldrich, www.sigmaaldrich.com). Dynamic coating entails applying a positive pressure of nitrogen gas to a reservoir containing the

polymer solution and directing it through the device. Nitrogen flow was maintained for 2 hours after the solution passed through the device to evaporate the solvent. Cross-linking was achieved by temporarily sealing the inlet and outlet ports of the μTM and heating to 180 °C with the integrated heaters. Although the short capillary sections connected to the device are also coated during this process, they do not affect the device performance or the chromatographic separation of the analytes significantly.

4.3.3 Temperature Control

The temperature sensors were calibrated by placing the μTM in a convection oven, which provided a temperature range of -60 to 120 ^{o}C (Figure 4.7). Heating was achieved by applying a square-wave voltage pulse to the microheater on each μTM stage using separate DC power supplies (E3646A, Agilent). A custom-made computer program (C#, Microsoft) controlled the heating operation. Constant power of 40 W (8 A and 5 V) was continuously applied to the thermoelectric cooler. Thus, one stage was maintained at low temperature as the other stage was heated. Dry air or nitrogen was used to prevent moisture condensation on the μTM surface.

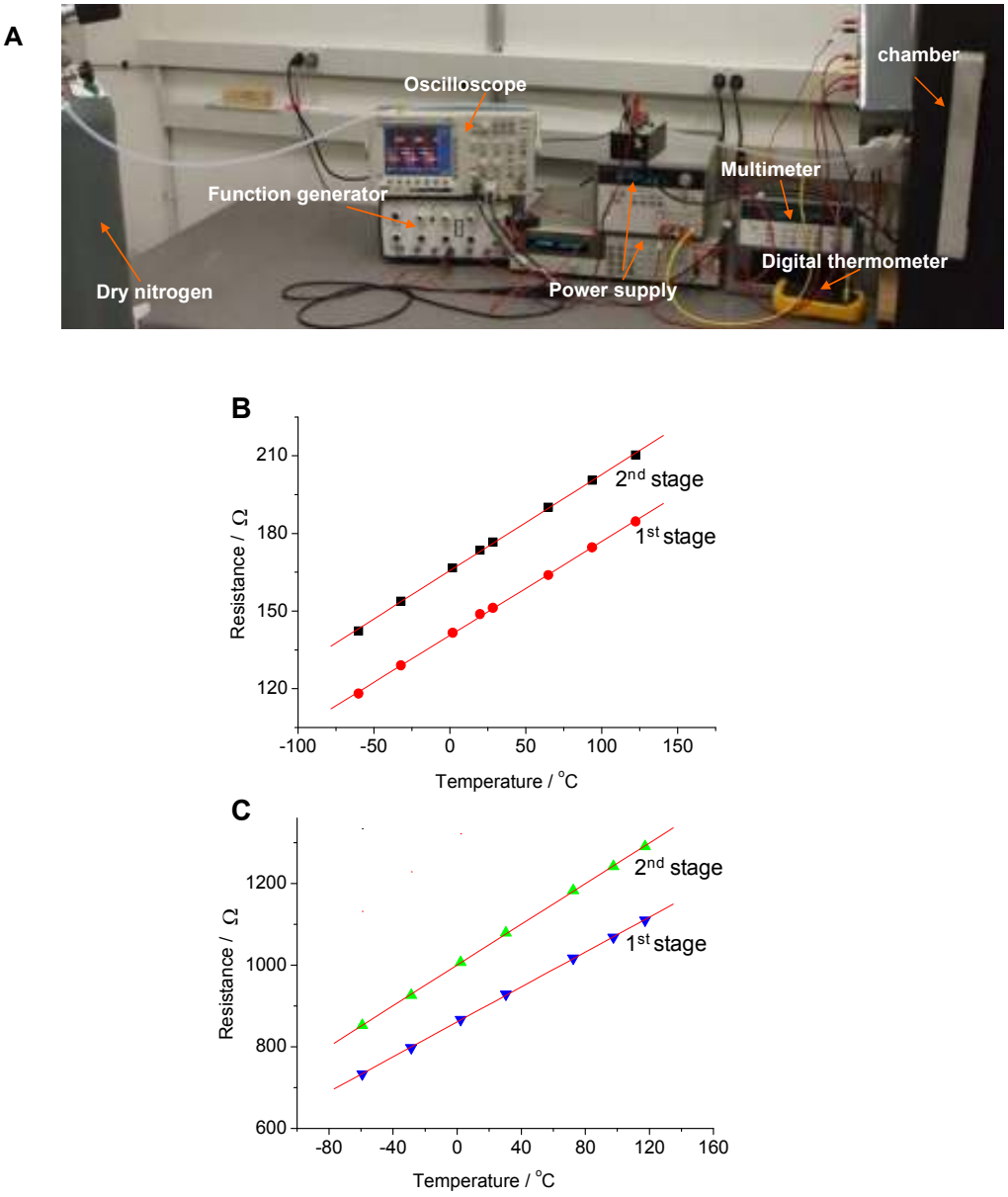

Figure 4.7. Experimental setup and calibration curves. (**A**) Experimental setup for the temperature calibration and thermal measurements. (**B** and **C**) Temperature calibration of microheaters and temperature sensors. Electrical resistances of the microheaters (B) are several times lower than those of the temperature sensors (C). Resistances (R) of the heaters and the temperature sensors are linearly proportional to the temperature (T). That is, $R = a + bT$ where a and b are constants that are determined by the linear curve fitting of each resistor.

4.3.4 Peak Modulation Conditions

The μTM was placed in the oven of a bench-scale GC (7890A, Agilent, Santa Clara, CA) equipped with a split/splitless injector and a flame-ionization detector (FID). A 3-m-long section of a commercial fused-silica capillary column (250 μm i.d.) having a PDMS stationary phase (0.25 μm thickness) was connected to the short section of capillary remaining at the device inlet by means of a press-fit connector. In lieu of a second-dimension column, the outlet of the μTM was connected to the FID with a short length of uncoated, deactivated fused silica capillary (100 μm i.d), also by means of a press-fit connector.

The linear velocity of the He carrier gas was set to 12 cm/s by adjusting the head pressure on the GC inlet and measuring the time required for a sample of methane gas (unretained) to pass through the system. Headspace samples (1 μL) of reagent-grade n-alkanes (Sigma-Aldrich) were injected with a nominal split ratio of 100:1.

Separations were performed with the GC oven set at 30ºC. Modulation was achieved by applying 100-ms voltage pulses to each stage in succession, with a 1-sec delay between first and second stage heating, which raised the temperature of each stage to 250°C. The period of time between modulations was either 5 s or 7 s. The sampling rate of the detector was 500 Hz.

4.4. Results and Discussion

This chapter presents high-thermal speed and low-power operation of the μTM for the application of GC×GC system. For this goal, we predict the performance of the μTM using a lumped thermal model, and compare it with the experimental results. Finally, preliminary results demonstrating the modulation and sensitivity enhancement of a sample mixture of hexane, heptane, and octane vapors are presented.

4.4.1. Energy-change Rates

Figure 4.8 shows time evolution of each energy rate in the first stage based on our model, when its microheater is turned on for 0.15 s at 40 V. The energy-storage-rate term ($\dot{E}_{1\_sys}$) balances with the heat-transfer terms and the sign of each energy-rate term has the following meaning: the sign of the $\dot{E}_{1\_sys}$ value reflects the sign of the first-stage temperature-change with time, because $\dot{E}_{1\_sys}$ is proportional to the temperature-change rate ($\dot{E}_{1\_sys} \propto dT/dt$); the heat-transfer terms take positive values when thermal energy moves into the first stage. The model assumes that the thermoelectric cooler is left on to maintain its temperature at approximately −55 ^{o}C throughout the entire process. $\dot{E}_{1\_gen}$ is initially at its maximum and decreases during the heating process as the electrical resistance of the microheater increases with time (or alternatively with temperature)

while the applied voltage remains constant. So, we define the average heating power as the time integration of $\dot{E}_{1\_gen}$ over the heating time that the applied DC voltage is on

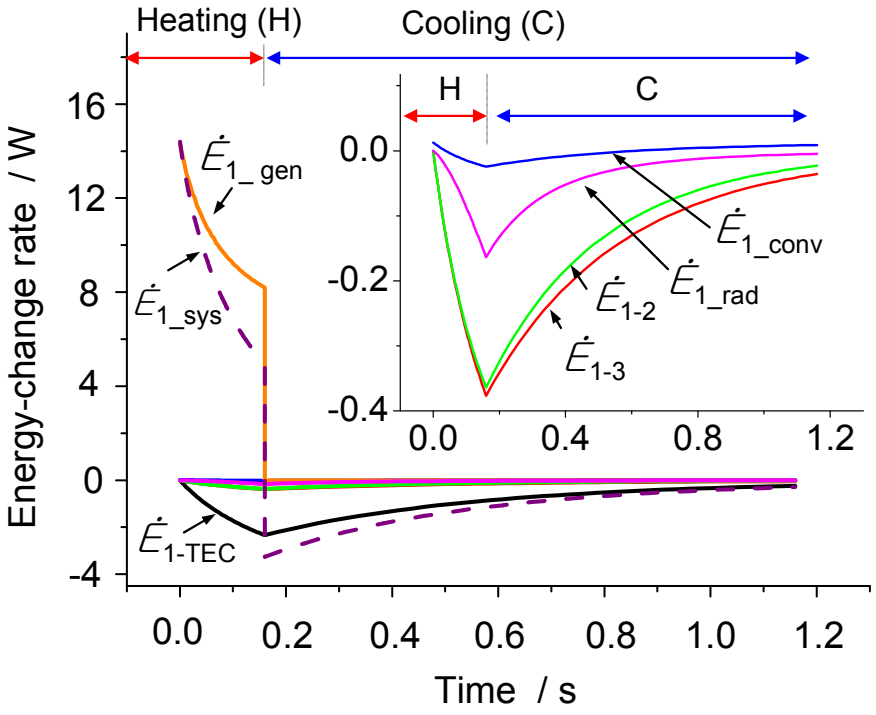

Figure 4.8. Energy-change rates at the μTM first stage. The values are calculated from the energy balance for each subcomponent. The input voltage is a square pulse of 40 V with duration of 150 ms. The air gap, the Pyrex thickness, and the IC length are 38 μm, 100 μm, and 1 mm, respectively. The energy-storage rate of the first stage ($\dot{E}_{1\_sys}$) balances with the other energy-transfer/generation rates. When the heat is generated at the heater of the first stage ($\dot{E}_{1\_gen}$), it is mainly dissipated through the thermoelectric cooler ($\dot{E}_{1\text{-}TEC}$). The inset shows that the heat dissipated through the other paths (conduction to the second stage and to the rim ($\dot{E}_{1\text{-}2}$ and $\dot{E}_{1\text{-}3}$); convection and radiation to the environment ($\dot{E}_{1\_conv}$ and $\dot{E}_{1\_rad}$), respectively) is insignificant.

divided by the time. Notably, $\dot{E}_{1\text{-}TEC}$ is the dominant heat-dissipation term among the heat-transfer terms. As shown in the inset of Figure 4.8, heat conduction through the Pyrex membrane and the ICs ($\dot{E}_{1\text{-}3}$ and $\dot{E}_{1\text{-}2}$) is more important than convection and

radiation ($\dot{E}_{1\_conv}$ and $\dot{E}_{1\_rad}$). The two terms, $\dot{E}_{1\text{-}3}$ and $\dot{E}_{1\text{-}2}$, in conjunction with the heat transfer via the air gap ($\dot{E}_{i\text{-}TEC}$) affect the thermal crosstalk between the two stages. Compared with the other heat-transfer terms that initially have a value of zero, $\dot{E}_{1\_conv}$ and $\dot{E}_{1\_rad}$ have small positive values at the outset because of the difference between the ambient temperature (25 ^{o}C) and the initial temperature of the first stage (–55 ^{o}C). Thus, in convection and radiation, thermal energies initially move into the first stage.

4.4.2 Effect of Pyrex thickness on thermal response

To efficiently trap the eluting vapors and introduce them to the second-dimension column in a narrow band, fast cooling and heating are necessary with low heating and cooling power. We focused on minimizing thermal-response time and heating power. For practical reasons related to microfabrication, we focused on Pyrex-membrane thicknesses of 40 and 100 μm, and compare the experimental data and the theoretical prediction. Initially, the μTM was approximately at -55 ^{o}C by the cooling unit. When a constant voltage was applied for a 150 ms duration, the first stage heated up and reached its maximum temperature; then it cooled down to -55 ^{o}C (Figure 4.9A and 4.9B).

As expected, the device with the thinner Pyrex membrane was raised to a higher temperature for a given applied voltage. It required only 62% of the average power required for the thicker-membrane device (i.e., 6.8 W vs. 11 W) to achieve a temperature of 200 ^{o}C (Figure 4.10). For the experimental data, time evolution of power was directly measured from the applied current and the voltage and, for the theoretical prediction, it

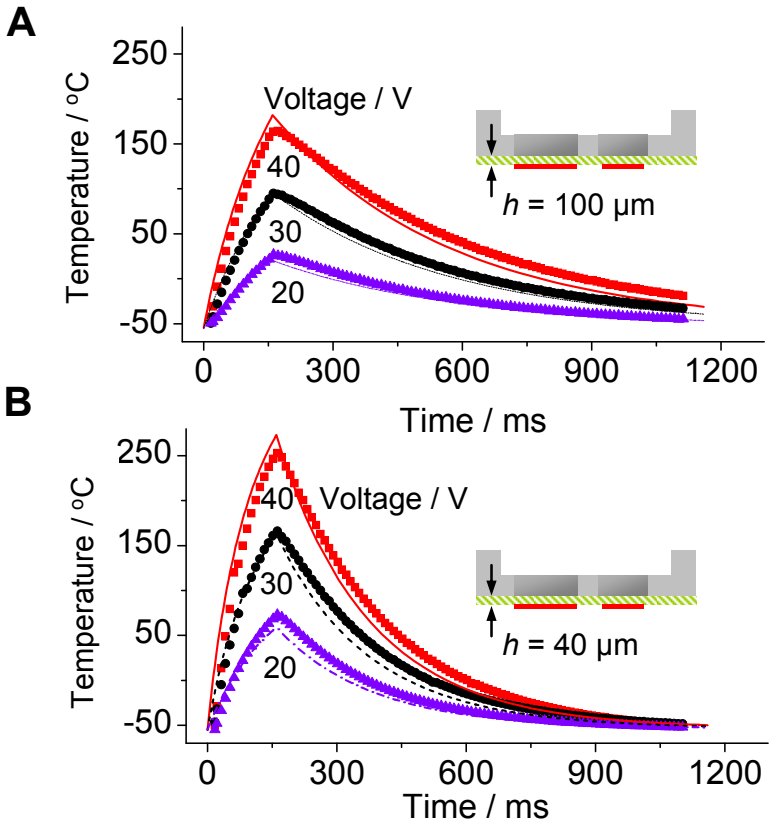

Figure 4.9. Thermal response of the µTM first stage as a function of input voltage-pulse for Pyrex membrane thicknesses, *h,* of (A) 40 µm and (B) 100 µm (points: experimental data, lines: theoretical predictions). The input voltage was a square pulse with duration of 150 ms. The air gap and the IC length are 38 µm and 1 mm, respectively. The thinner (40 µm) Pyrex membrane results in faster cooling and a higher temperature at the same applied voltage.

was calculated from the electrical resistance and the voltage at the microheater. Then, the average heating powers were obtained from the area of heating power curve (e.g. $\dot{E}_{1\_gen}$ curve in Figure 4.8) divided by the duration of the voltage pulse (i.e., 150 ms). The thinner Pyrex membrane also permits a faster cooling response (Fig. 4.9A and 4.9B), with the time constant (τ) for cooling being about half of that for the device with the thicker Pyrex membrane (i.e., τ = 0.24 vs, 0.46 s, Figure 4.10 inset).

The inset of Figure 4.10 shows a linear relationship between τ and the membrane thickness. The τ is proportional to the thermal mass (M_T) and is inversely proportional to the thermal conductance (G_T) by the heat-transfer terms (i.e. $\tau = M_T / G_T$). The Pyrex-

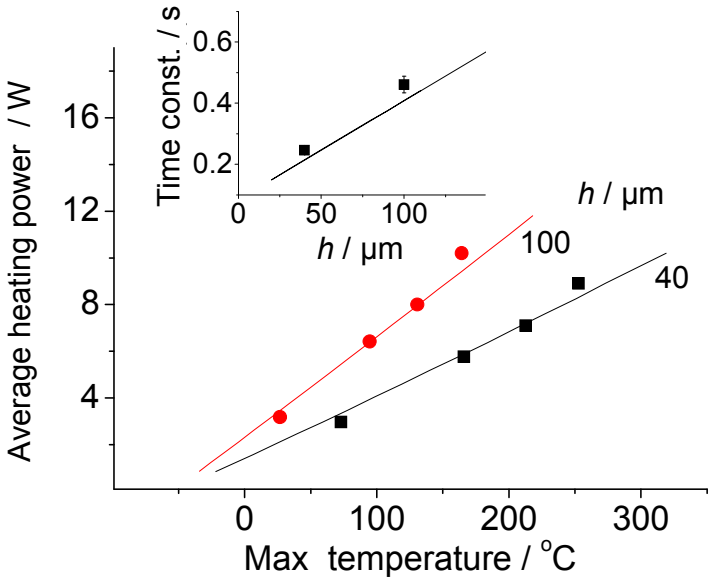

Figure 4.10. Average heating power and its corresponding maximum temperature. The average heating power is defined as the area of the $\dot{E}_{1\_gen}$ curve divided by the duration of the voltage pulse (150 ms). The μTM with the thicker (100 μm) Pyrex membrane requires higher power to achieve the same maximum temperature. The inset shows the time constant of the μTMs as a function of h.

membrane thickness generally affects both M_T and G_T. Even though the values of $\dot{E}_{1\text{-}3}$ and $\dot{E}_{1\text{-}2}$ change with the Pyrex thickness, G_T shows little change because $\dot{E}_{1\text{-TEC}}$, which is only governed by the air-gap size, is the dominant term in the heat transfer (Figure 4.8).

As a result, the change of τ is mainly dependent on M_T. Thus, τ is linearly proportional to the Pyrex thickness.

4.4.3 Effect of air gap on thermal response

We then explored how changing the air-gap thickness affects the heating and cooling responses of the device. Figure 4.11A shows the thermal response of the first stage for two representative air gaps (22 μm and 63 μm) upon applying 35 V to the microheater for 100 ms. Notably, the temperature increase was smaller for the device with the smaller air gap. Accordingly, the power required to reach a maximum temperature of 210 ^{o}C was calculated to be 11.5 W with the smaller air gap and 7.2 W with the larger gap (Figure 4.11B). The inset of Figure 4.11B shows that the theoretical average heating-power required for reaching the same maximum temperature of the first stage (T_{max1}) increases sharply with the decreasing air gap.

On the other hand, the narrower air gap resulted in faster cooling (Figure 4.11A). Figure 4.12 clearly shows variations of τ with the air-gap size for devices with two different Pyrex membrane thicknesses. The change in τ with the air gap is more pronounced for the device with the 100-μm membrane. However, the values of τ tended

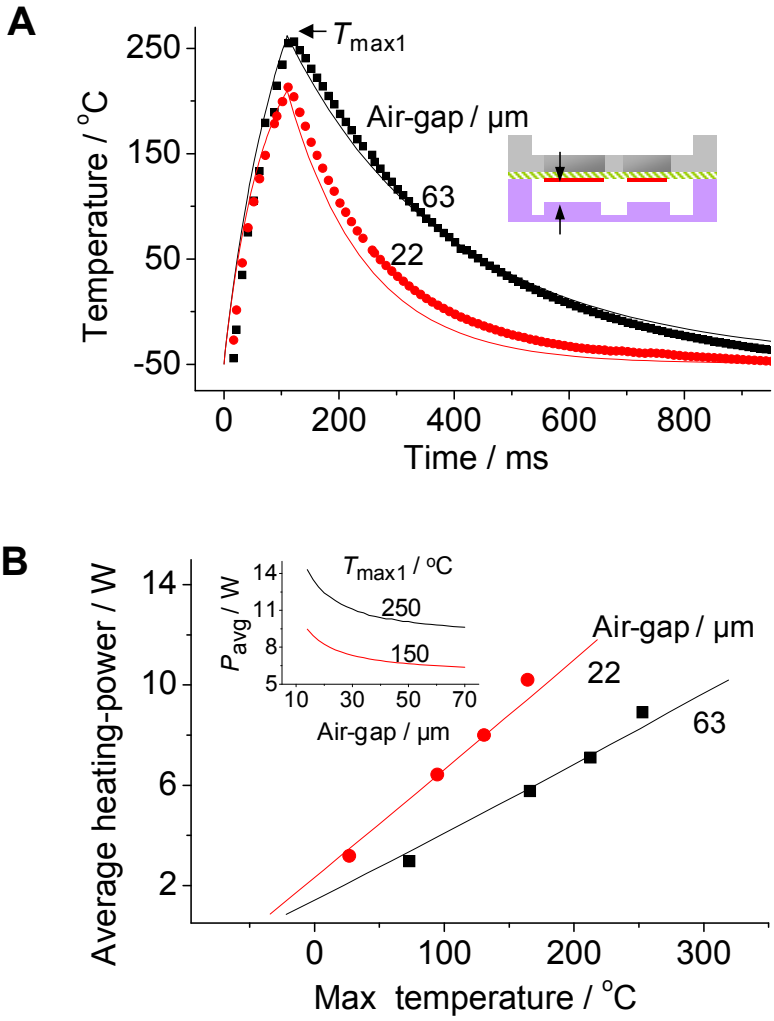

Figure 4.11. Thermal response of the first stage μTM influenced by the air gap (points: experimental data, lines: theoretical predictions). Here, the Pyrex thickness, the IC length, and the duration of the input voltage-pulse are 40 μm, 1 mm, and 100 ms, respectively. (A) Results for different air-gap sizes. The applied voltage peak is fixed at 35 V. The narrower air gap results in lower maximum temperature but faster cooling. (B) Average heating power and its corresponding maximum temperature. The narrower air gap requires higher power for the same maximum temperature. The inset shows a nonlinear relation between the theoretical average heating-power (P_{avg}) and the air gap.

to converge as the air gap became small for the both membrane thicknesses. Figure 4.13 summarizes the values of τ predicted for various combinations of the Pyrex thickness and the air gap. Here, we see that a narrow air gap enhances the cooling speed at the expense of higher heating power. Initially setting the air gap small (down to 22 μm) is a practically viable approach because (1) once we set the system, it is difficult to change the air-gap size while the power can be easily controlled and (2) the power consumption is found to be still at an acceptable level even for the narrow air gap of 22 μm.

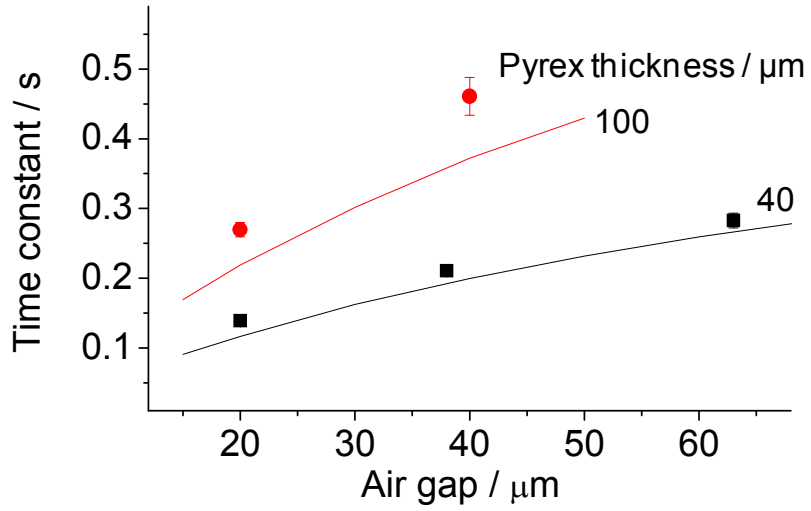

Figure 4.12. Influence of air gap and Pyrex thickness on the time constant. As the air gap becomes narrow, the time constant becomes smaller, i.e., faster thermal response.

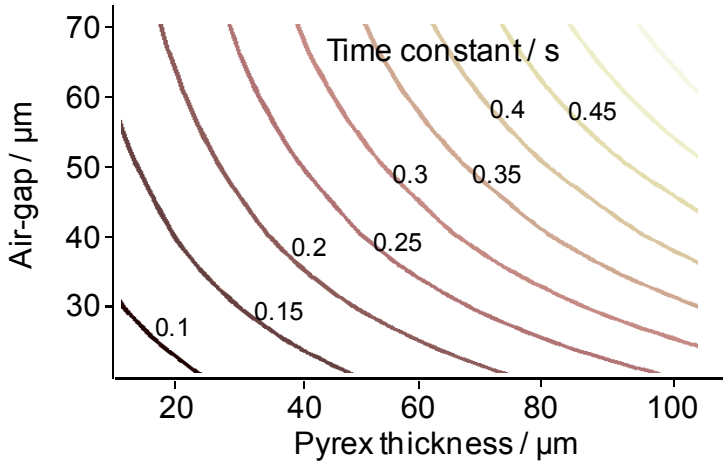

Figure 4.13. Theoretical contour lines of the time constant with respect to the various combinations of the air-gap and the Pyrex-thickness values.

Although τ varies linearly with the Pyrex-membrane thickness (Inset of Figure 4.10), it varies nonlinearly with the air gap (Figure 4.12). This nonlinear relation comes from the relation between the thermal conductance, G_T, and the air gap. The G_T can be thought of as $a / L_{air} + b$, where a and b are constants, because the rate of the heat transfer via the air gap ($\dot{E}_{1\text{-TEC}}$) varies inversely proportional to the air-gap thickness (L_{air}) while the other heat transfer terms are invariant. Thus the result is $\tau \propto 1 / G_T = 1/(a / L_{air} + b)$. Figure 4.12 also shows a steeper slope of the time-constant curve for the larger Pyrex thickness. Because τ is also proportional to M_T, the thicker Pyrex membrane makes the slope of the time-constant curve steeper.

4.4.4 Effect of air gap and IC length on thermal crosstalk

Although the heating of one of the stages inherently influences the temperature at the other stage (Figure 4.14A), this thermal crosstalk should be minimized to independently control the temperatures of the two stages. To achieve this goal, we varied the air gap from 22 to 38 μm and the IC length from 0.5 to 1.5 mm based on theoretical modeling and experimental data indicating that these would provide a reasonable tradeoff between thermal-response speed and heating-power consumption, and would also provide acceptable vapor-modulation performance. Specifically, an air gap > 40 μm yielded a cooling time from 250 to -50 ^{o}C of > 1 s, while an air gap < 20 μm required > 13 W to heat from -55 to 250 ^{o}C (Inset of Figure 4.14B). Also an IC longer than 1.5 mm may result in broader vapor peaks because of the large temperature gradient inside the IC.

As shown in Figure 4.14B, the IC length affects the thermal crosstalk more than the air-gap thickness in these ranges. For a first-stage maximum temperature (T_{max1}) of 200 ^{o}C, the maximum temperature rise of the second stage (ΔT_{max2}) varied from 9 to 11 ^{o}C with the air gap varying from 22 to 38 μm for the IC length fixed at 1.5 mm, whereas ΔT_{max2} changed from 9 to 19 ^{o}C with the IC length varying from 1.5 mm to 0.5 mm with the air gap fixed at 22 μm. We see that the thermal crosstalk, which is defined as $\Delta T_{max2}/\Delta T_{max1} \times 100$ %, was maintained as small as 9.2% (at T_{max1} = 200 ^{o}C) even for the worst case where the IC length and the air gap were 0.5 mm and 38 μm, respectively.

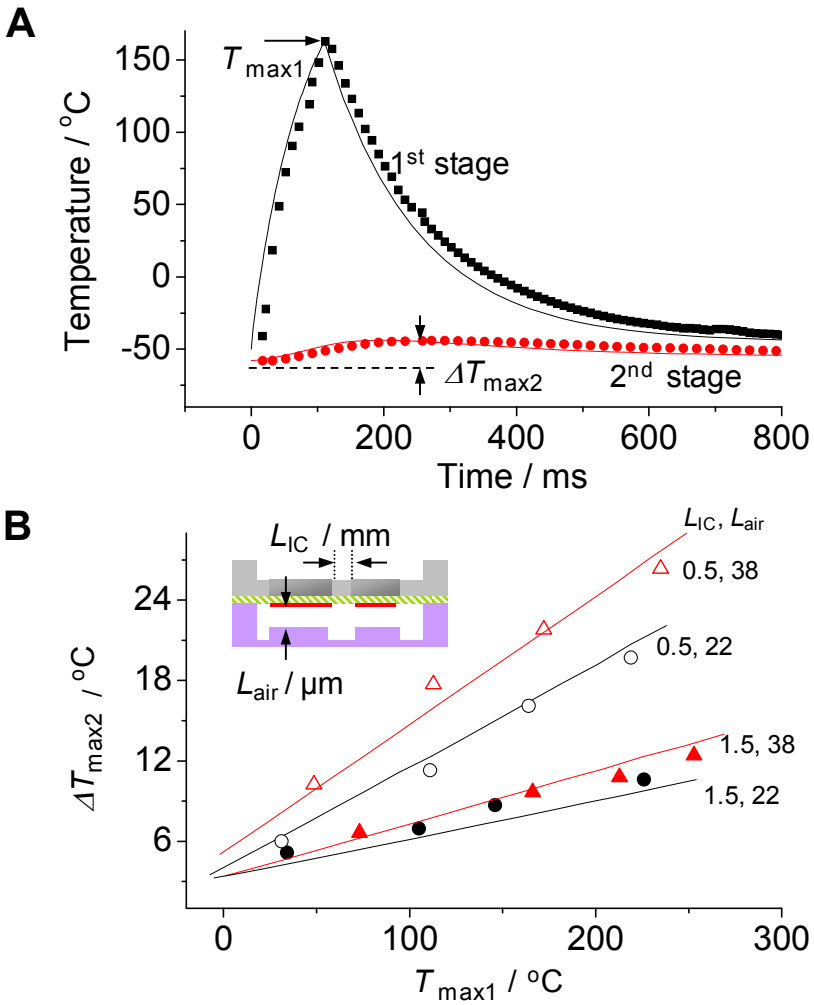

Figure 4.14. Thermal crosstalk between the two μTM stages (points: experimental data, lines: theoretical predictions). The duration of the input voltage-pulse and Pyrex thickness are 100 ms and 40 μm, respectively. (**A**) Temperature rise of the second stage by the heating of the first stage. T_{max1} is the maximum temperature of the first stage, and ΔT_{max2} is the maximum temperature rise of the second stage. The air-gap, the IC length, and the applied voltage-pulse are 22 μm, 1 mm, and 35 V, respectively. (**B**) Influence of air-gap and IC length on ΔT_{max2}.

The dominant effect of the IC length on the thermal crosstalk can be explained by comparing dissipated thermal energies. The energy-storage rate of the second stage ($\dot{E}_{2\_sys}$) balances with the other heat-transfer parameters (Figure 4.15). However, $\dot{E}_{2\text{-}1}$and $\dot{E}_{2\text{-}TEC}$, which are the conductive heat transfer between the two stages via IC and between

the second stage and the thermoelecric cooler via the air gap respectively, are the major contributors to the temperature of the second stage: $\dot{E}_{2\text{-}1}$and $\dot{E}_{2\text{-TEC}}$ affect the temperature rise and the drop, respectively. So we consider only these two terms for our analysis. We estimated the effects of the air gap and the IC length on the maximum temperature rise of the second stage (ΔT_{max2}) by considering dissipated energies rather than energy-change

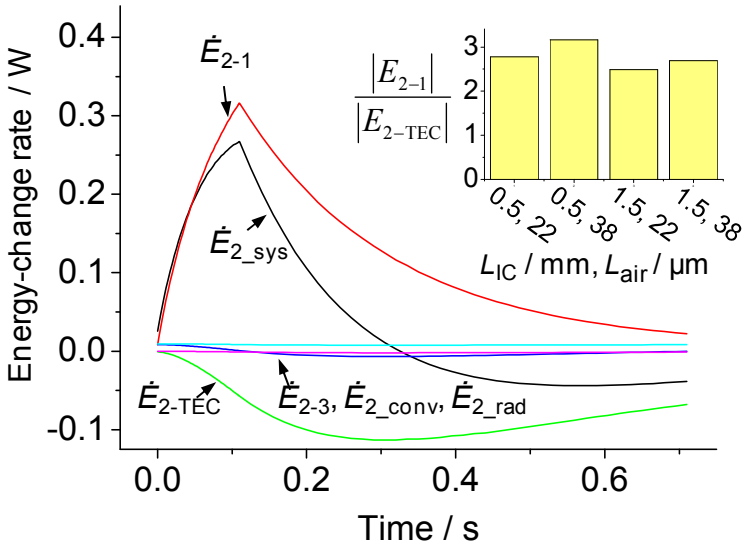

Figure 4.15. Energy-change rates at the second stage by the heating of the first stage. The air gap (L_{air}), the IC length (L_{IC}), and the square voltage-pulse applied to the first stage are 38 μm, 1.5 mm, 40 V with 100 ms duration, respectively. The inset shows the ratio of the energy dissipated through the IC ($E_{2\text{-}1}$) and through the air-gap ($E_{2\text{-TEC}}$) over the time for the temperature rise to reach ΔT_{max2}.

rates, because ΔT_{max2} represents an energy state determined by the thermal history. Thus, we compared the ratio of the two dissipated energies ($E_{2\text{-}1}$, $E_{2\text{-TEC}}$) at ΔT_{max2}. The energies were calculated by integrating the area of $\dot{E}_{2\text{-}1}$ and $\dot{E}_{2\text{-TEC}}$ curves, respectively. Regardless of the values used for the IC length and air gap, the ratio of the two dissipated

energies remain at a value of ~3 (Inset of Figure 4.15), indicating that the IC length dominates the thermal crosstalk.

4.4.5 Peak modulation

Initial tests of μTM operation were successful. A device with a 100-μm-thick Pyrex membrane, 22-μm-thick air gap and 1-mm-long IC was used. The homologous series of alkanes, n-hexane, n-heptane, and n-octane, was used to span a moderate range of volatility (vapor pressures range from 14-140 mmHg at 25 ºC) while retaining symmetric peak shapes with the upstream separation column operated at 30 ºC. n-Hexane was used for single-vapor testing. The modulator was operated in the range of -30 °C to 250 °C. Heating and cooling rates were 3000 °C/s and -570 °C/s, respectively.

Unmodulated, the injected sample of n-hexane, gave a broad, low-intensity peak with a FWHH of 4.1 s. With an identical second injection and modulation period of 5 s, the μTM generated 5 slices of the original n-hexane peak with a FWHH of 0.3 s that retained the profile of the unmodulated peak (Figure 4.16A). Although a shorter modulation period would lead to a greater number of modulated peaks, it is generally considered sufficient to generate 3 slices of each initial (unmodulated) peak passing through a modulator [81]. As is to be expected, there is an increase in the relative intensity from

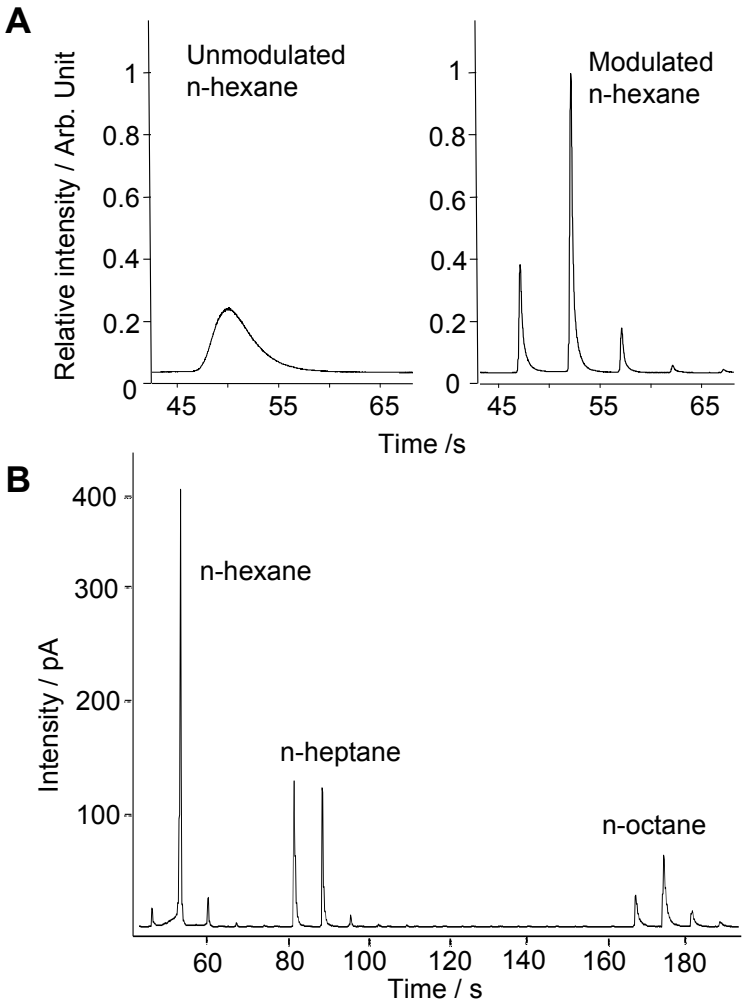

Figure 4.16. Modulation of injected test samples using a μTM with a 22-μm air gap, a 100-μm Pyrex membrane thickness, and a 1-mm IC length. Square voltage-pulses of 40 V and 35 V were applied to the microheaters on the first and second stage, respectively, for 100 ms each at 1 s delay. (**A**) Comparison of unmodulated and modulated FID responses for two separated injections of n-hexane. The modulation period was 5s. There is an enhancement in relative intensity and a reduction in peak width for the modulated peaks. (**B**) Modulated peaks of an injected headspace sample of a mixture of n-hexane, n-heptane, and n-octane vapors, using a modulation period of 7 s. The relative magnitudes of the peaks and their FWHH values reflect the relative volatility of the mixture components.

the unmodulated to the modulated peaks. The expected resolution enhancement is reflected in the decrease in the FWHH value; narrower peaks are more easily resolved by the second dimension column in a GC×GC system. This, in turn, increases the overall

peak capacity. The decrease in FWHH values can be seen by the fact that the 5 modulated slices elute in the same amount of time as the 1 unmodulated peak. Here, an approximately 5-fold peak enhancement is achieved for the maximum peak among the 5 slices. Of course, the maximum signal and FWHH values will be affected by the modulation period, heating and cooling rates, and velocity of the carrier gas through the modulator. The results shown here serve to illustrate that initial testing shows the μTM is operating as expected.

Figure 4.16B shows the chromatogram of the alkane mixture with a 7 s modulation period. As in Figure 6A, there was a 1s delay between heating the two μTM stages. The relative magnitudes of the signals are qualitatively consistent with the headspace concentration of each component, which is a function of their vapor pressures, and the FWHH values of 0.26, 0.37, and 0.70 s, for n-hexane, n-heptane, and n-octane, respectively, also reflect the relative volatility of the components. Although there is some evidence of breakthrough for n-hexane, as indicated by the apparent increase in the baseline at the base of the largest modulated peak, it is clear that the μTM is effectively focusing and desorbing all three mixture components. Breakthrough of less volatile compounds can be reduced or eliminated by reducing the modulation period, increasing the stage length, or reducing the injected sample mass [82]. These issues are a matter of optimizing the device design and the operating conditions relevant to a particular analysis. With the μTM employed for these tests, cooling from 250 to -20 ^{o}C requires ~0.9 s, which limits the minimum modulation period and the delay between heating the stages to no less than 1s. Reducing this period any further would increase the extent of breakthrough observed for the more volatile compounds in a mixture. This limitation is

due largely to the relatively thick Pyrex-membrane used in this device. Designs with thinner membranes should reduce this problem and allow for more rapid temperature cycling.

CHAPTER V

Conclusions and Future Works

5.1 Summary of Thesis

The research in this thesis developed two thermal MEMS devices for (1) microfluidic mixing and (2) gas chromatographic thermal modulation. In our microfluidic mixing study, the micromixer using natural convection successfully enabled microfluidic mixing and biochemical reaction in a single chamber. In our gas chromatographic thermal modulation study, the MEMS thermal modulator successfully modulated several vapor species at low power for heating and no coolants for cooling. A summary of all the presented achievementsis given in the following sections.

5.1.1. Micromixer for Microfluidic Networks

One of the goals achieved through this research is the development of a scheme for efficient micromixing using natural convection. We have demonstrated for the first time

the utility of natural convection– a phenomenon that has been widely believed to be weak or even negligible in the microfluidic regime – for micromising. The process is achieved by alternatively activating micro integrated heaters of different modes in a proper gravitational direction. Our study shows that natural convection can induce micromixing at a rate as high as a few tens of seconds per microliter even at a low fluidic temperature of ~ 37 °C.

The second goal was to achieve micromixing and biochemical reaction in a single microfluidic chamber with the aim to simplify the structure of microfluidic networks. With computer-programmed operation of the heaters, we have achieved autonomous on-chip PCR for a DNA sample from the influenza viral strain A/LA/1/87. Our approach holds great promise for a wide variety of microfludic applications involving thermally induced chemical and biochemical reactions. Our single-chamber scheme would be suited for system integration of microfluidic components involving all of sample preparation, reaction, and detection processes without adding complexity.

5.1.2. Microthermal Modulator for GC×GC

In our gas chromatographic thermal modulation study, the first objective was to implement a MEMS thermal modulator that requires low power for heating and no coolants for cooling, without sacrificing the speed of thermal response. We have developed and tested a MEMS-based μTM, designed for use in comprehensive two-dimensional separations of complex mixtures of volatile organic compounds. Two significant advances over the existing TMs include (1) fast thermal response at a low heating power (~10 W), where the power is two orders of magnitude smaller than that of

the conventional benchtop TMs, and (2) elimination of cryogenic consumables for cooling. These unique features constitute significant advantages over current TM techniques. Also, the thermal crosstalk between the two stages was negligible (< 9%), thereby enabling independent control of their temperatures. Furthermore, a lumped thermal model provided predictions in remarkably good agreement with the experimental results. The model predicted the temperatures of each stage and included all heat transfer modes of the μTM system. As a result, the model enabled quantitative analysis on the thermal response and thermal crosstalk of each stage as the Pyrex-membrane thickness, the air gap, and the IC length were varied. Although we confined this thermal model for the analysis of the μTM, the model could be applied to any thermal systems when the thermal mass and heat transfer terms are properly considered.

The second objective was to demonstrate the modulation of the mass transport of organic vapor species carried by a convective flow of an inert gas using the MEMS thermal modulator. We demonstrated preliminary modulation of hexane, heptane, and octane using the μTM. For heptane vapor, an approximately 5-fold peak enhancement was achieved.

5.2 Future Research and Applications

The continued work on the natural convection-driven micromixer and the μTM will have prominent impact on several research fields. Potential future work using the micromixer includes (1) development of an integrated DNA analysis system that requires cell lysis, DNA microarray, as well as PCR, and (2) application of the technology for biosynthesis. Future work can branch off from our μTM study towards three directions: (1) design improvement for faster thermal response, (2) in-depth study of the volatile organic compound separation using our μTM and (3) integration of our μTM into a micro gas chromatography system.

5.2.1. Micromixer for Microfluidic Networks

One of the promising applications using the natural convection-driven microfluidic flow is heat-mediated cell-lysis. Heat-mediated cell-lysis is a method for DNA extraction [83, 84] and is required for many biotechnological methods such as Southern blotting [85] and PCR. However, due to the large thermal mass in conventional samples, a long incubation time (>10 minutes, 90–100 °C) is typically required for efficient DNA extraction from cells suspended in a centrifuge tube. To speed up the process, microfluidic technologies have been employed. Previous studies show that microfluidic systems enable the cell-lysis process to be completed within several minutes with smaller sample volume.. Although the devices perform the lysis process in a fast manner, they make the microfluidic system complex because the devices use an electrical (Figure 5.1)

or a mechanical lysis approach that require additional pumps and electrodes in microfluidic channels, or nanostructured filter [86, 87].

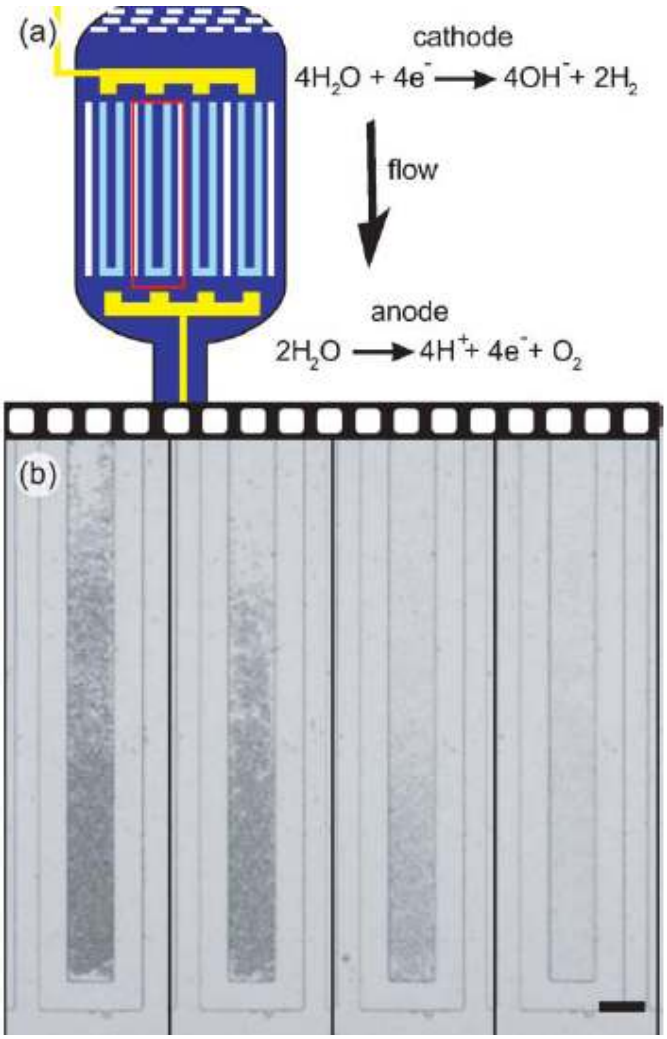

Figure 5.1. Characterization of electrochemical cell lysis. (**a**) Schematic of electrochemical lysis via hydroxide generation at the cathode upstream of cell traps. The sample is premixed outside the microfluidic chamber. (**b**) Images taken from video of cells being electrochemically lysed in the region outlined in red in (a). Applied voltage is 3 V. Scale bar is 150 μm [86].

Integrated heat-mediated cell-lysis would be a desirable function in microfluidic networks, especially where heating is used both for micromixing and for cell lysis.

Because mixing of the cell solution, buffer, and chemical reagents is prerequisite for cell lysis, natural convection-driven micromixer enables mixing and cell lysis in a single chamber, thereby simplifying microfluidic networks.

Another possible application of the natural convection-driven mixer is a DNA microarray. A DNA microarray is an analytical tool in molecular biology to measure changes in expression levels, to detect single nucleotide polymorphisms (SNPs), and to genotype or resequence mutant genomes [88]. In DNA microarrays, DNA hybridization is an essential part, where single strand DNA pairs with the complementary strand by hydrogen bonding (Figure 5.2). So the binding force increases as two stands pair perfectly. The mismatched strands separate each other at above a certain temperature (thermal stringency) [89].

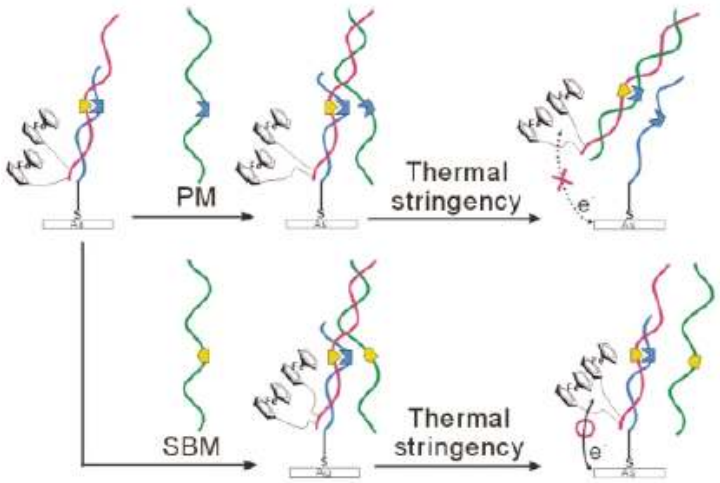

Figure 5.2. Schematic diagrams of electrochemical detection for single base mismatch (SBM) DNA by competitive hybridization reaction [89].

The hybridization rate strongly depends on mass transfer in the bulk solution. However, in conventional microarrays, hybridization relies solely on diffusion and, thus,

is a slow process that typically requires 6-20 h to complete the process. This long hybridization time greatly limits the throughput of sample analyses. Thus, various methods have been developed to accelerate the hybridization process, including DNA migration enhancement by direct electric field [90, 91], dynamic DNA hybridization using paramagnetic beads [92], cavitation microstreaming [93], and the use of a microporous three-dimensional biochip through which the hybridization solution is pumped continuously [94].

These methods commonly use micromixing technique to accelerate hybridization kinetics and to improve uniformity of the hybridization. For example of the cavitation microstreaming for the enhancement of DNA hybridization (Figure 5.3), the method resulted in up to 5-fold hybridization fluorescent signal-enhancement with significantly improved signal uniformity, as compared to the results obtained in conventional diffusion-based biochips for a given time (2 h).

However, besides the micromixing, the temperature of the hybridization chamber is maintained in the range of 45 – 50 °C to separate mismatched strand from the probe DNA [89 – 93]. In the previous studies for hybridization enhancement, the chamber needs two different means for micromixing and for heating, thus making the system more complex. In contrast, we could use natural convection to simultaneously achieve micromixing and hybridization in a microfluidic chamber. This scheme would greatly simplify the microfluidic network design, eliminating many microfluidic chambers and channels.

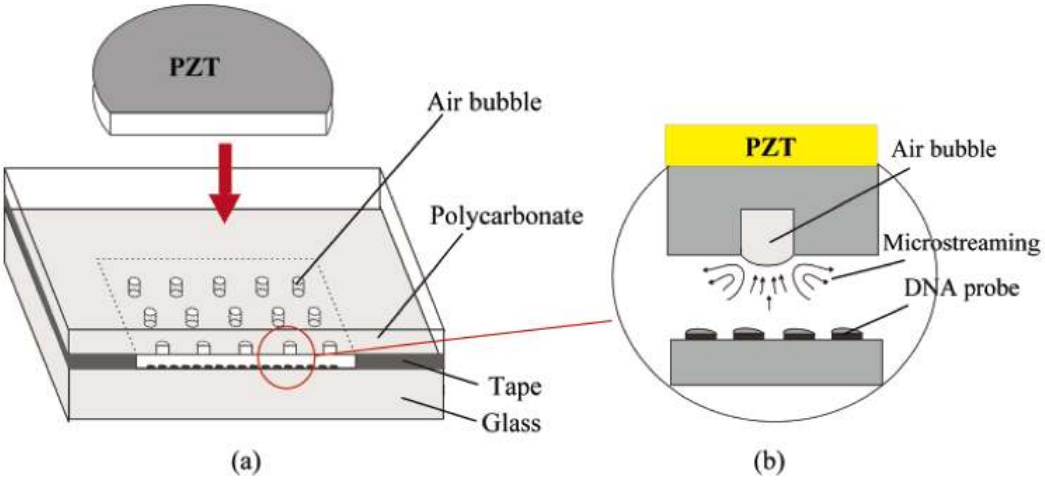

Figure 5.3. Schematic showing a number of air pockets in the top layer of the DNA biochip chamber: (**a**) overview and (**b**) side view [93].

Biosynthesis would be another potential application of the natural convection-driven micromixing. For example, consider the production of radioactively labeled molecules used in positron emission tomography (PET) for cancer detection. Microfluidic device can dramatically accelerate the development of many new molecular imaging probes for PET. To demonstrate the utility of a microfluidic device, one imaging probe for PET, 2-deoxy-2-[^{18}F]fluoro-D-glucose, was synthesized by the device [76]. The device used five sequential processes involving [18F]fluoride concentration, water evaporation, radiofluorination, solvent exchange, and hydrolytic deprotection (Figure 5.4). Since these process require both mixing and chemical reactions in the temperature range of 60 – 120 °C, our natural convection-driven mixer may play an essential role in simplifying the complex architecture of the device.

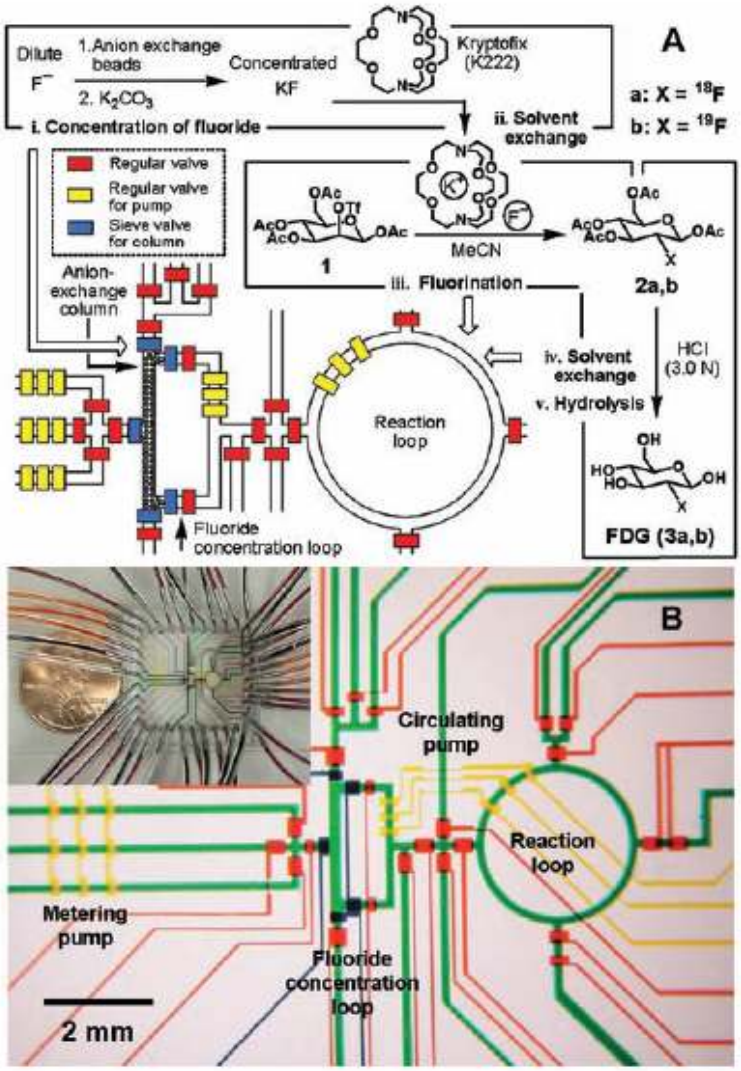

Figure 5.4. (**A**) Schematic representation of chemical reaction circuit used in production of 2-deoxy-2-fluoro-D-glucose (FDG). Five sequential processes are shown. (**B**) Optical micrograph of the central area of the circuit. The various channels have been loaded with food dyes to help visualize the different components of the microfluidic chip;d colors are as in (A), plus green for fluidic channels [76].

5.2.2. Microthermal Modulator for GC× GC

The current μTM suffers from relatively slow cooling response due to the thick Pyrex membrane (~ 100 μm). Theoretical analysis showed the thermal response can be greatly improved as the Pyrex thickness becomes thinner. During the Pyrex thinning-process by polishing, the Pyrex layer, however, breaks easily because grooves on the process Si-wafer cannot support the pressure on it from the polishing pad (Figure 5.5A). Alternatively, we could use a sacrificial Si wafer for the polishing process (Figure 5.5B). The sacrificial wafer supports the Pyrex wafer during the polishing, so the breakage problem could be avoided. However, another issue may arise from the two-step anodic bonding process with a single Pyrex wafer. The potential problem is that the mobility of sodium ions, which significantly affects the bonding strength, may be reduced after the

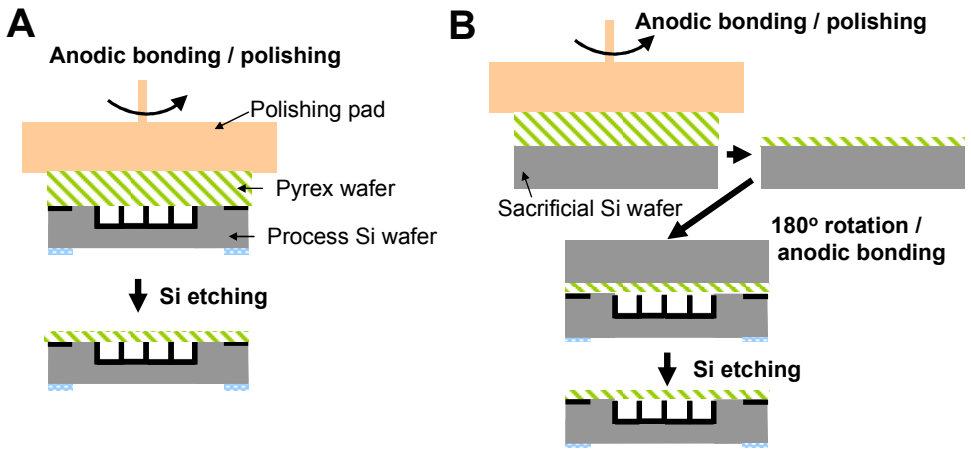

Figure 5.5. Polishing process to thin down Pyrex layer. (**A**) Current process. Because polishing pad applies pressure on Pyrex layer that has grooves, such groove region easily breaks during polishing process. (**B**) Proposed process.

first anodic bonding because of the high bonding temperature. As a result, the second anodic bonding between the Pyrex and the process Si-wafer would be prevented. So a future study remains to be performed to achieve an anodic bonding process that yields sufficient bonding strength at appropriate temperature.

Another problem in the μTM design is Si spacer (Figure 5.6A and 5.6B). Because Si has high thermal conductivity (140 W/ Km), generated heat in rim heater is directly transferred to TEC, resulting in the temperature rise of TEC. This temperature rise should be prevented to trap the analytes having low boiling point. As a way to address

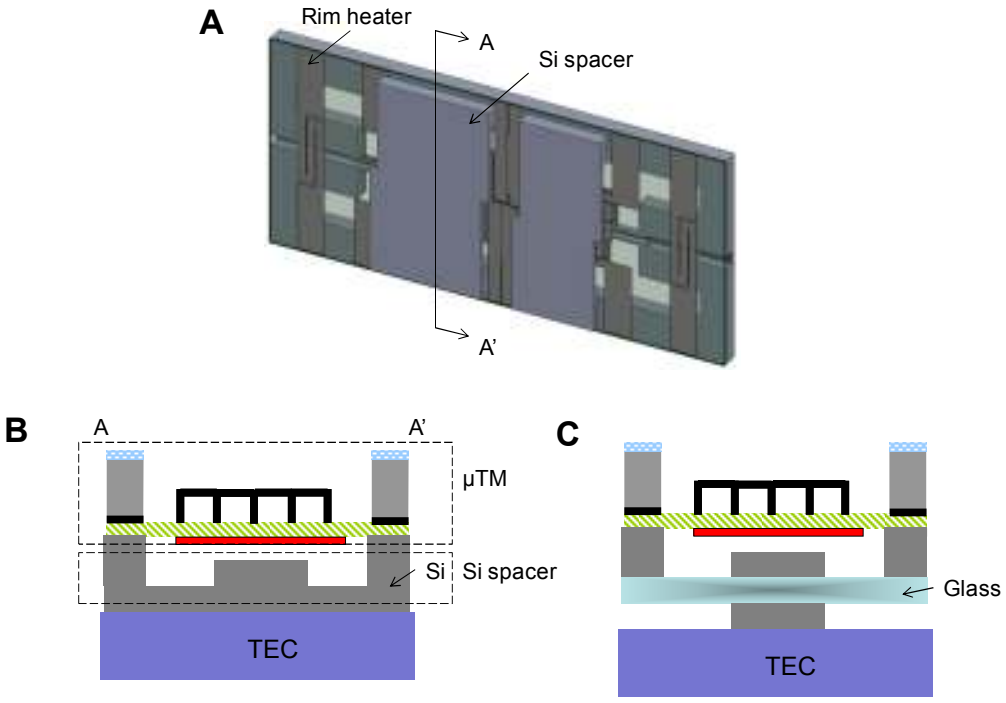

Figure 5.6. Spacer design for air gap. (**A**) Microthermal modulator (μTM) with Si spacer. (**B**) Current design of spacer. In this design, generated heat in the rim heater (Figure 5.6A) is dominantly transferred to TEC through Si spacer because of high thermal conductivity of Si material (140 W/Km). (**C**) Proposed design of spacer. Heat transfer from the rim heater to TEC is greatly suppressed because of low thermal conductivity of glass (~2 W/Km).

this issue, glass layer could be used as the spacer (Figure 5.6C). Because of the low thermal conductivity (~ 2 W/ Km) of the glass, high thermal isolation between the rim heater and the TEC can be achieved.

Currently, power consumption in cooling the TEC is relatively higher (40 W) than that in heating the μTM (~10 W). One way to reduce the power consumption in TEC is minimizing the dead zone of TEC where the area is not used for cooling the μTM. Effective area of the μTM where the cooling is necessary is ~ 4×8 mm^2, whereas the cooing area of the current TEC is 6.4×10.9 mm^2. Because cooling area of TEC is highly related to power consumption of TEC, there is a room for great power reduction in cooling. Table 3 shows that we can save 38 W by reducing the cooling area of TEC at the expense of small decrease in maximum temperature-gradient (ΔT_{max}) that TEC can generate between its top and bottom surfaces.

Table 5.1. Cooling performance of TECs and their cooing areas.

Model*	ΔT_{max} (Vacuum)	Required power	Cooling area
SP2394 (current TEC)	127 ^oC	45 W	6.4×10.9 mm^2
NL4012T	114 ^oC	7 W	4.1×7.9 mm^2

*www.marlow.com

Using our μTM integrated in a conventional benchtop GC setup, our future work will study in depth the device's performance in separating volatile organic compounds. The important parameters that affect the vapor peaks are (1) the flow velocity of the carrier gas; (2) the thermal modulation phase, which is defined as the relative position of the

modulation events with respect to the unmodulated peak (Figure 5.7) and is typically given in terms of angle degree (e.g. 180° is out of phase, and 0° or 360° is in phase); and

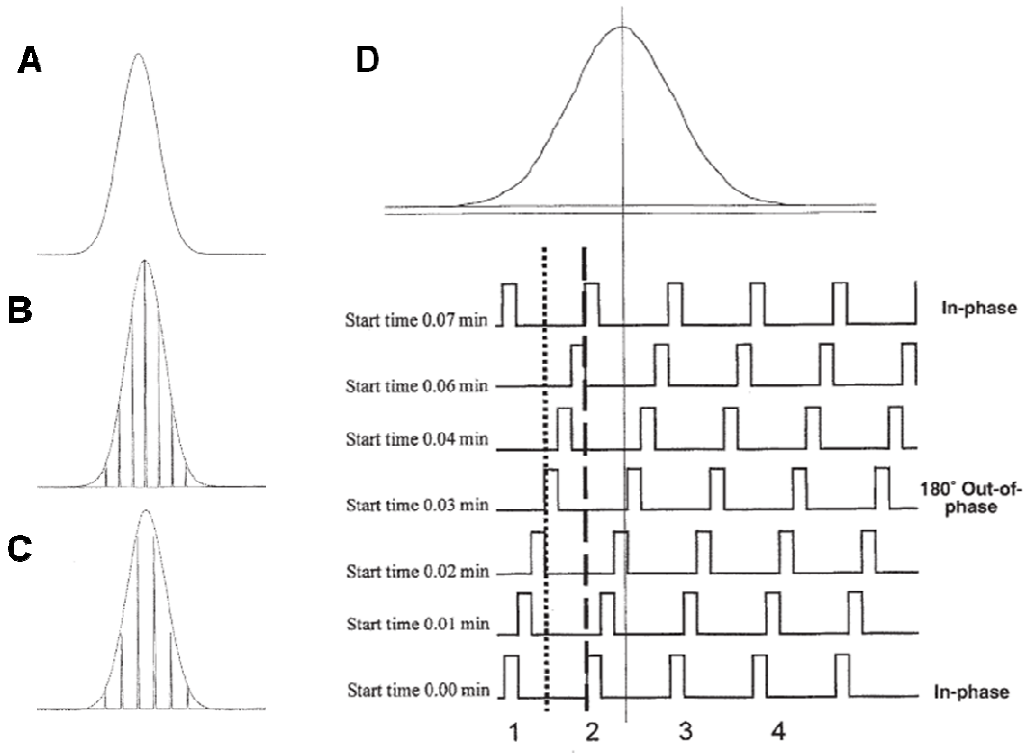

Figure 5.7. Correlation of phase of modulation and peak elution. (**A**) A normal nonmodulated GC peak, (**B**) in-phase modulated GC peaks, (**C**) 180° out-of-phase modulated GC peaks in GC×GC, and (**D**) Modulation signals from thermal modulators. Square pulse means heating signal and flat base line means cooling signal. A delay of 0.03 min results in a 180° out-of-phase modulation case with the 0.03-min delay exactly midway between pulses 1 and 2 in the original modulation (dotted line), and a 0.06-min delay gives a result that is in-phase with the original modulation (dashed line). The vertical line shows that the central zone of the peak is exactly captured in the third modulation and thus this will give an in-phase result equivalent to Figure 5.6B [95] .

(3) the modulation period, which is defined as the periodic time including the heating and cooling cycle times of the modulator. Firstly, we should study the influence of the flow velocity of the carrier gas on the modulated/unmodulated peaks. The flow velocity of the carrier gas needs to be set at the optimal value that generates the maximum peak capacity

(i.e. the minimum width of the unmodulated peak at half height) from Golay plot. So we need to optimize the flow velocity for practical operation of the μTM.

Another subject that we need to explore is the correlation between the modulation phase and the period. Although the modulation phase is hard to control for the multiple analytes because the elution time and the unmodulated peak-width vary with each analyte, it is possible to intentionally regulate the phase for a single analyte. For a single analyte, when the modulation period is long (i.e. the number of modulation of an unmodulated peak is small), the peak enhancement should greatly vary with respect to the modulation phase. The effect is expected to be minor as the modulation period becomes short. Our future work will study this effect for a wide range of organic vapors. In conjunction with the peak enhancement, we can also check other parameters such as the cumulative area and the full-width-at-half-height (FWHH). To make the peak narrower, we can make the round corners; Radadia *et al.* [96] showed 1.4 times narrower peak at FWHH using a rounded channel wall, compared to a rectangular channel. We may also make the peak narrower by minimizing the spatial temperature gradient in the μTM.

Demonstrating a fully integrated micro GC×GC system with the μTM would be another goal. For this goal, a complete GC×GC microsystem consisting of the two microcolumns, the μTM, a commercial thermoelectric cooler, four transfer-line heaters, and associated electronics need to be fabricated and assembled (Figure 5.8). The system holds considerable promise for a wide range of applications, including homeland security, environmental monitoring, health care (analysis of breath biomarkers), and the analysis of extraterrestrial atmospheres [97].

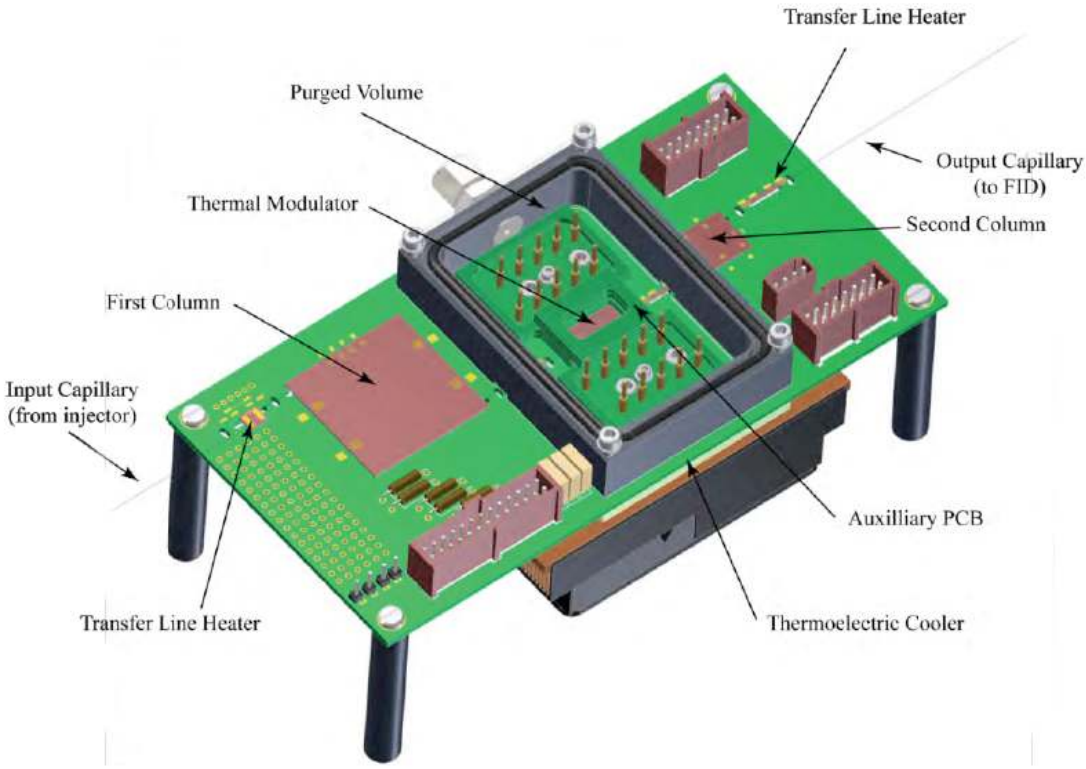

Figure 5.8. Primary components of the micro GC×GC system [97].

Appendix I

Microfluidic Mixer Fabrication: Heating Instrument

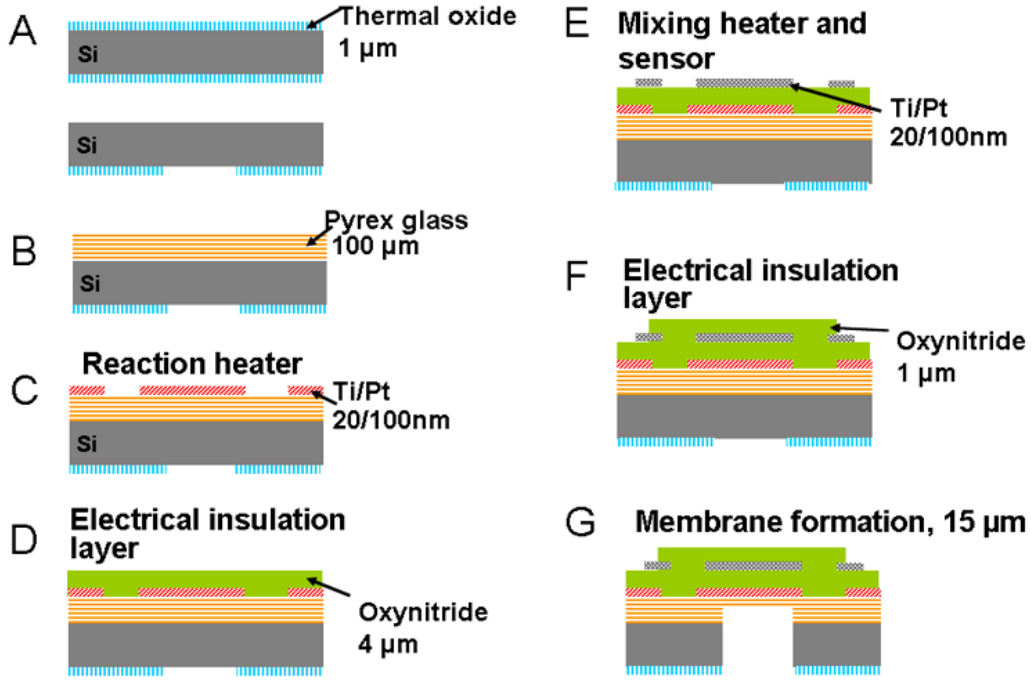

Figure I. Fabrication steps for the Heating Instrument.

A.1) Prefurnace Clean (Prefurnace Clean Bench)

Organic Clean (H_2O : NH_4OH : H_2O_2 = 2 : 1 : 1): 90°C, 10 min

DI Water Rinse: 2 min

HF (100:1) Dip: 30 sec

DI Water Rinse: 2 min

Ionic Clean (H_2O: HCl : H_2O_2 = 2 : 1 : 1): 90°C, 10 min

DI Water Rinse: 15 min

Spin Rinse and Dray: until resistivity reaches 15.1 Ω/cm^2

A.2) Thermal Oxidation – EDP etching mask (A4 Furnace)

Recipe: DWDA1

Parameter Table: OXIDIZE

Temperature: 1100°C

Dry: 5 min, Wet: 3 hour 20 min, Dry: 5 min, N_2 Aneal: 5 min

Thickness: 1 μm

A.3) Photoresist Patterning – Oxide etching

Photoresist: PR 1827, ~2.7 μm

Spin on Backside: 500 rpm, 4 s + 4000 rpm, 30 s

Soft Bake on Hotplate: 110°C, 1 min 10 s

Cool Down in Ambient: >5 min

Exposure (MA6 Mask Aligner): 11 s

Development (MF-319): ~1 min

DI Water Rinse: 3 min

Descum in March Asher: O2, 80 W, 250 mT, 1 min

A.4) Oxide Patterning (Acid Wet Bench)

BHF Dip: ~10 min

A.5) Photoresist Removal (Organic Wet Bench)

PRS-2000 Soak: >10 min

DI Water Rinse: 5 min

Spin Rinse Dry

B.1) Si and Pyrex Wafer Cleaning

Piranha Clean (H2SO4 : H2O2 = 1 : 1): 10 min

DI Water Rinse: 5 min

Dry on Hotplate

B.2) Pyrex bonding to Si wafer (SB6E)

Pyrex thickness: 100 μm

Recipe: sungjin_anodic

C.1) Photoresist Patterning –Ti/Pt Lift-off

Photoresist: AZ 5214E, ~1.7 μm

Spin: 500 rpm, 4 s + 4000 rpm, 30 s

Soft Bake on Hotplate: 110°C, 1 min 30 s

Cool Down in Ambient: >5 min

Exposure (MA6 Mask Aligner): 0.5 s

Hard Bake on Hotplate: 115°C, 2 min

Flood Exposure (MA6 Mask Aligner): 15 s

Development (MF-300): ~1 min

DI Water Rinse: 3 min

Descum in March Asher: O2, 80 W, 250 mT, 1 min

C.2) Ti/Pt deposition (EnerJet Evaporator)

Thickness: 10/100 nm

C.3) Ti/Pt Lift –off

Soak in Aceton for 10 min

DI Water Rinse: 3 min

D.1) Oxynitride depotision for Electrical Insultation (GSI PECVD)

Recipe: Oxynitride 200

Thickness: 4 μm

E.1) Photoresist Patterning –Ti/Pt Lift-off

Photoresist: AZ 5214E, ~1.7 μm

Spin: 500 rpm, 4 s + 4000 rpm, 30 s

Soft Bake on Hotplate: 110°C, 1 min 30 s

Cool Down in Ambient: >5 min

Exposure (MA6 Mask Aligner): 0.5 s

Hard Bake on Hotplate: 115°C, 2 min

Flood Exposure (MA6 Mask Aligner): 15 s

Development (MF-300): ~1 min

DI Water Rinse: 3 min

Descum in March Asher: O2, 80 W, 250 mT, 1 min

E.2) Ti/Pt deposition (EnerJet Evaporator)

Thickness: 10/100 nm

E.3) Ti/Pt Lift –off

Soak in Aceton for 10 min

DI Water Rinse: 3 min

F.1) Oxynitride depotision for Electrical Insultation (GSI PECVD)

Recipe: Oxynitride 200

Thickness: 1 μm

F.2) Photoresist Patterning for Electrical Pads

Photoresist: PR 1827, ~2.7 μm

Spin on Backside: 500 rpm, 4 s + 4000 rpm, 30 s

Soft Bake on Hotplate: 110°C, 1 min 10 s

Cool Down in Ambient: >5 min

Exposure (MA6 Mask Aligner): 11 s

Development (MF-319): ~1 min

DI Water Rinse: 3 min

Descum in March Asher: O2, 80 W, 250 mT, 1 min

F.3) Oxide Patterning (Acid Wet Bench)

HF Dip: ~2 min

G.1) EDP Wet Etching (Using Wafer Holder from www.ammt.com)

DI water: Catechol: Pyrazine: Ethylenediamene

= 432 mL: 432 g: 8.1 g: 1.35 L

Temperature: 110°C, Etching Time: ~ 8 hour

DI Water Rinse: 10 min @ 80°C

G.2) Wafer Dicing

Dicing with MA 1006 Dicing Saw: Blade 42525

G.3) Thinning of Pyrex Membrane (Acid Wet Bench)

HF Dispensing to membrane: ~ 11 min

DI Water Rinse: 10 min

Appendix II

Microfluidic Mixer Fabrication: Microfluidic Cartridge

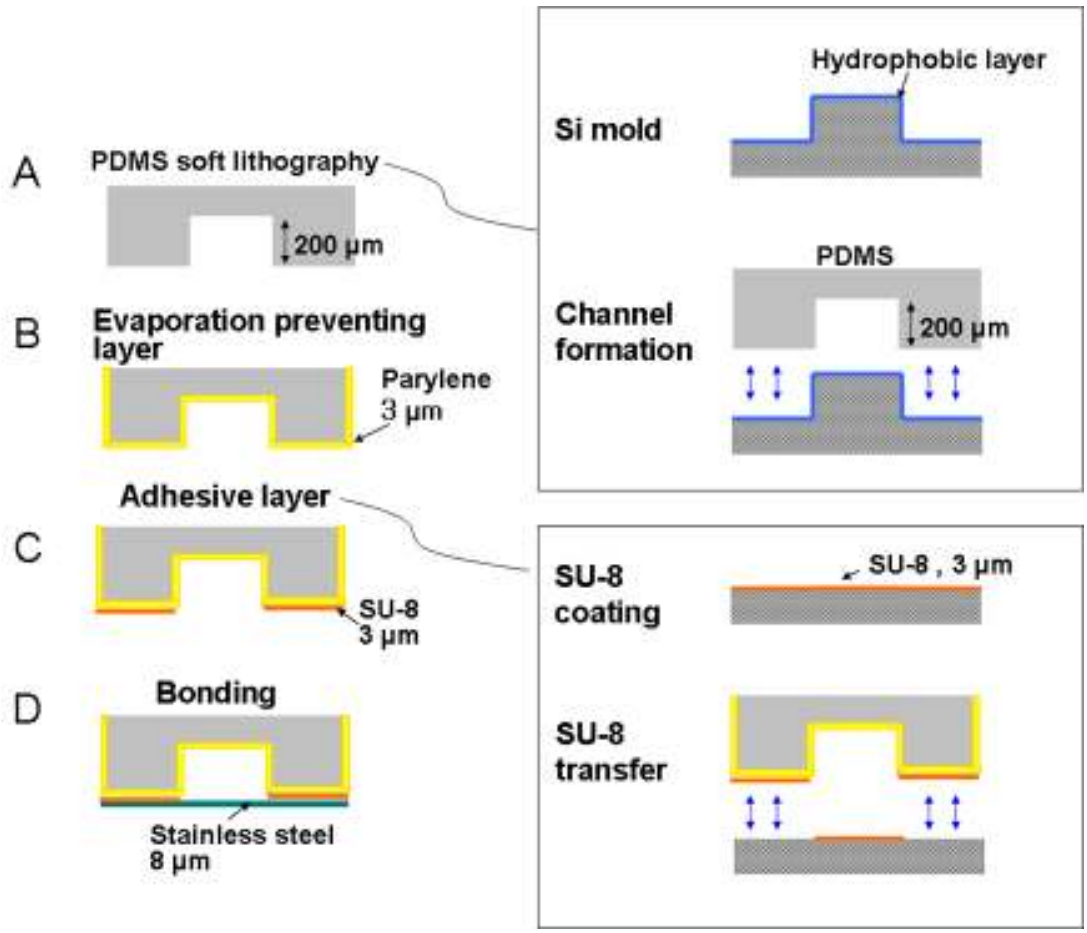

Figure I I. Fabrication steps for the Microfluidic Cartridge.

A.1) Si Wafer Clean

Piranha Clean (H2SO4 : H2O2 = 1 : 1): 10 min

DI Water Rinse: 5 min

Spin Rinse Dry

A.2) Photoresist Patterning

Photoresist: AZ 9260, ~8 µm

Spin on Frontside: 500 rpm, 4 s + 3000 rpm, 30 s

Soft Bake on Hotplate: 110°C, 3 min 30 s

Cool Down in Ambient: >5 min

Exposure (MA6 Mask Aligner): 28 s

Development (AZ400: DI = 1:3): ~ 4 min

DI Water Rinse: 3 min

A.3) Frontside DRIE – Mold patterning

DRIE in STS ICP Machine: Recipe TYC-HR2,

Target depth: 200 μm, Etching time: ~100 min

A.4) Photoresist Removal (Organic Wet Bench)

PRS-2000 Soak: >10 min

DI Water Rinse: 5 min

Spin Rinse Dry

A.5) Hydrophobic surface coating

Recipe: TUNGY2 (STS DRIE)

Baking on Hotplate: 120°C, 5 min; 150°C, 30 min

A.7) Softlithography

PDMS Precursor Mixing: Sylgard 184 (Base : Curing Agent = 10 : 1)

Degas in Desiccator: 30 min

Place Wafer Containing Microfluidic Channel Mold in Petri Dish

Pour PDMS Over Mold, ~4 mm thick

Degas in Desiccator: 30 min

Cure PDMS at Room Temperature, 2 days

Peel PDMS from Si Mold

A.8) Inlets/Outlet Fabrication

Cut Holes Through PDMS Using Biopsy Punch

B.1) Parylene Deposition (PDS2010)

Thickness: ~2 μm

C.1) SU-8 Bonding

Photoresist: SU-8 5

Spin on Si Wafer: 500 rpm, 5 s + 5000 rpm, 30 s

PDMS contact printing on SU-8 5

D.1) PDMS + Stainless Steel (8 μm) bonding

Manual bonding

Baking on Hoplate: 80°C, 2 min

UV Exposure: 5 sec (MA6 Aligner)

Post Exposure Baking: 80°C, 2 min

Appendix III

Microthermal Modulator Fabrication

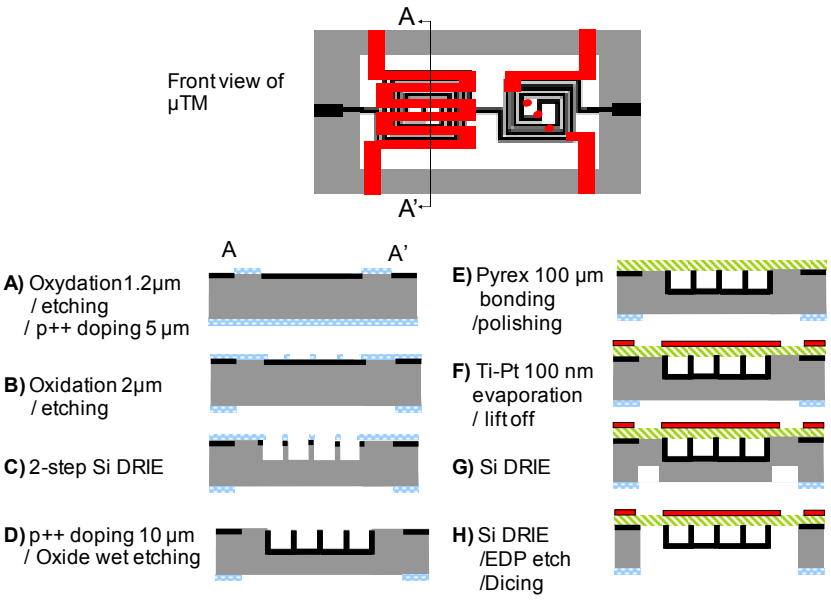

Figure I I I. Fabrication steps for the Microthermal Modulator.

A.1) Prefurnace Clean (Prefurnace Clean Bench)

100 Si wafer, thickness 400–450 µm

Organic Clean (H_2O : NH_4OH : H_2O_2 = 2 : 1 : 1): 90°C, 10 min

DI Water Rinse: 2 min

HF (100:1) Dip: 30 sec

DI Water Rinse: 2 min

Ionic Clean (H_2O: HCl : H_2O_2 = 2 : 1 : 1): 90°C, 10 min

DI Water Rinse: 15 min

Spin Rinse and Dray: until resistivity reaches 15.1 Ω/cm^2

A.2) Thermal Oxidation – Boron Diffusion Barrier (A4 Furnace)

Recipe: DWDA1

Parameter Table: OXIDIZE

Temperature: 1100°C

Dry: 5 min, Wet: 3 hour 20 min, Dry: 5 min, N_2 Aneal: 5 min

Thickness: 1 μm

A.3) Photoresist Patterning – Oxide etching

Photoresist: PR 1827, ~2.7 μm

Spin: 500 rpm, 4 s + 4000 rpm, 30 s

Soft Bake on Hotplate: 110°C, 1 min 10 s

Cool Down in Ambient: >5 min

Exposure (MA6 Mask Aligner): 11 s

Development (MF-319): ~1 min

DI Water Rinse: 3 min

Descum in March Asher: O2, 80 W, 250 mT, 1 min

A.4) Oxide Patterning (Acid Wet Bench)

BHF Dip: ~10 min

A.5) Photoresist Removal (Organic Wet Bench)

PRS-2000 Soak: >10 min

DI Water Rinse: 5 min

Spin Rinse Dry

A.6) Prefurnace Clean (Prefurnace Clean Bench)

Organic Clean (H_2O : NH_4OH : H_2O_2 = 2 : 1 : 1): 90°C, 15 min

DI Water Rinse: 2 min

HF (100:1) Dip: 30 sec

DI Water Rinse: 2 min

Ionic Clean (H_2O: HCl : H_2O_2 = 2 : 1 : 1): 90°C, 15 min

DI Water Rinse: 15 min

Spin Rinse and Dray: until resistivity reaches 15.1 Ω/cm^2

A.7) Shallow Boron Doping (A2 Furnace)

Recipe: BDEP99

Parameter Table:BORON99

Dep Time: 45 min, Dilution Time: 30 min, Temperature: 1175°C

A.8) Oxide Removal (Acid Wet Bench)

BHF Dip: ~20 min

A.9) Frontside Photoresist Patterning – Height regulation for Pyrex bonding

Photoresist: PR 1827, ~2.7 μm

Spin: 500 rpm, 4 s + 4000 rpm, 30 s

Soft Bake on Hotplate: 110°C, 1 min 10 s

Cool Down in Ambient: >5 min

Exposure (MA6 Mask Aligner): 11 s

Development (MF-319): ~1 min

DI Water Rinse: 3 min

A.10) Si Patterning (Trion Oracle)

Recipe: Si_etch

Target depth: 150 nm, Etch Time: ~ 2 min

A.11) Photoresist Removal (Organic Wet Bench)

PRS-2000 Soak: >10 min

DI Water Rinse: 5 min

Spin Rinse Dry

B.1) Prefurnace Clean (Prefurnace Clean Bench)

Organic Clean (H_2O : NH_4OH : H_2O_2 = 2 : 1 : 1): 90°C, 15 min

DI Water Rinse: 2 min

HF (100:1) Dip: 30 sec

DI Water Rinse: 2 min

Ionic Clean (H_2O: HCl : H_2O_2 = 2 : 1 : 1): 90°C, 15 min

DI Water Rinse: 15 min

Spin Rinse and Dray: until resistivity reaches 15.1 Ω/cm^2

B.2) Thermal Oxidation (A4 Furnace)

Recipe: DWDA1

Parameter Table: OXIDIZE

Temperature: 1100°C

Dry: 5 min, Wet: 12 hour, Dry: 5 min, N_2 Aneal: 5 min

Thickness: 2.1 μm

B.3) Photoresist Patterning – Frontside Oxide etching and Backside Protection

Photoresist: PR 1827, ~2.7 μm

Spin on Frontside: 500 rpm, 4 s + 4000 rpm, 30 s

Soft Bake on Hotplate: 110°C, 1 min 10 s

Cool Down in Ambient: >5 min

Exposure (MA6 Mask Aligner): 11 s

Development (MF-319): ~1 min

DI Water Rinse: 3 min

Descum in March Asher: O2, 80 W, 250 mT, 1 min

Photoresist: PR AZ5214E, ~2 μm

Spin on Backside: 500 rpm, 4 s + 1500 rpm, 30 s

Soft Bake in oven: 110°C, 10 min

B.4) Oxide Patterning (Acid Wet Bench)

BHF Dip: ~21 min

B.5) Photoresist Removal (Organic Wet Bench)

PRS-2000 Soak: >10 min

DI Water Rinse: 5 min

Spin Rinse Dry

B.6) Photoresist Patterning – Backside Oxide etching and Frontside Protection

Photoresist: PR 1827, ~2.7 μm

Spin on Backside: 500 rpm, 4 s + 4000 rpm, 30 s

Soft Bake on Hotplate: 110°C, 1 min 10 s

Cool Down in Ambient: >5 min

Exposure (MA6 Mask Aligner): 11 s

Development (MF-319): ~1 min

DI Water Rinse: 3 min

Descum in March Asher: O2, 80 W, 250 mT, 1 min

Photoresist: PR AZ5214E, ~2 μm

Spin on Frontside: 500 rpm, 4 s + 1500 rpm, 30 s

Soft Bake in oven: 110°C, 10 min

B.7) Oxide Patterning

BHF Dip: ~21 min

B.8) Photoresist Removal

PRS-2000 Soak: >10 min

DI Water Rinse: 5 min

Spin Rinse Dry

C.1) Photoresist Patterning – Inlet and Outlet Ports

Photoresist: AZ 9260, ~8 μm

Spin on Frontside: 500 rpm, 4 s + 3000 rpm, 30 s

Soft Bake on Hotplate: 110°C, 3 min 30 s

Cool Down in Ambient: >5 min

Exposure (MA6 Mask Aligner): 28 s

Development (AZ400: DI = 1:3): ~ 4 min

DI Water Rinse: 3 min

C.2) Frontside DRIE – Inlet and Outlet Ports

DRIE in STS ICP Machine: Recipe TYC-HR2,

Target depth: 250 μm, Etching time: ~100 min

C.3) Photoresist Removal

PRS-2000 Soak: >10 min

DI Water Rinse: 5 min

Spin Rinse Dry

C.4) Frontside DRIE – Channels

DRIE in STS ICP Machine: Recipe TYC-HR2,

Target depth: 150 μm, Etching time: ~60 min

D.1) Prefurnace Clean (Prefurnace Clean Bench)

Organic Clean (H_2O : NH_4OH : H_2O_2 = 2 : 1 : 1): 90°C, 10 min

DI Water Rinse: 2 min

HF (100:1) Dip: 30 sec

DI Water Rinse: 2 min

Ionic Clean (H_2O: HCl : H_2O_2 = 2 : 1 : 1): 90°C, 10 min

DI Water Rinse: 15 min

Spin Rinse and Dray: until resistivity reaches 15.1 Ω/cm^2

D.2) Deep Boron Doping (A2 Furnace)

Recipe: BDEP99

Parameter Table: BORON99

Dep Time: 45 min, Dilution Time: 5 hour, Temperature: 1175°C

D.3) Boron Drive-in (A4 Furnace)

Recipe: N2ANL/OX

Parameter Table: N2ANL/OX

Set Time: 10 min, ANL Time: 5 hour, Temperature: 1175°C,

Dry: 5 min, Wet: 30 min, Dry: 5 min, Temperature: 1000°C

D.4) Photoresist Patterning – Backside Boroslicate Glass Removal

Photoresist: PR 1827, ~2.7 μm

Spin on Backside: 500 rpm, 4 s + 4000 rpm, 30 s

Soft Bake on Hotplate: 110°C, 1 min 10 s

Cool Down in Ambient: >5 min

Exposure (MA6 Mask Aligner): 11 s

Development (MF-319): ~1 min

DI Water Rinse: 3 min

Descum in March Asher: O2, 80 W, 250 mT, 1 min

D.5) Front-side Oxide and Backside Boroslicate Glass Removal (Acid Wet Bench)

BHF Dip: ~40 min

D.6) Photoresist Removal (Organic Wet Bench)

PRS-2000 Soak: >10 min

DI Water Rinse: 5 min

Spin Rinse Dry

D.7) Oxynitride depotision for DRIE mask (GSI PECVD)

Recipe: Oxynitride 400

Thickness: 4 μm

D.8) Photoresist Patterning

Photoresist: PR 1827, ~2.7 μm

Spin on Backside: 500 rpm, 4 s + 4000 rpm, 30 s

Soft Bake on Hotplate: 110°C, 1 min 10 s

Cool Down in Ambient: >5 min

Exposure (MA6 Mask Aligner): 11 s

Development (MF-319): ~1 min

DI Water Rinse: 3 min

D.9) Oxynitride etching (Acid Wet Bench)

BHF Dip: ~1 min

E.1) Si and Pyrex Wafer Cleaning

Piranha Clean (H2SO4 : H2O2 = 1 : 1): 10 min

DI Water Rinse: 5 min

Dry on Hotplate

E.2) Pyrex bonding to Si wafer (SB6E)

Recipe: sungjin_anodic400

E.3) Polishing (optional)

Pyrex thickness: 100 to 30 μm

F.1) Cr deposition (EnerJet Evaporator)

Thickness: 20 nm

F.2) Photoresist Patterning – Cr Patterning and Ti/Pt Lift-off

Photoresist: AZ 5214E, ~1.7 μm

Spin: 500 rpm, 4 s + 4000 rpm, 30 s

Soft Bake on Hotplate: 110°C, 1 min 30 s

Cool Down in Ambient: >5 min

Exposure (MA6 Mask Aligner): 0.5 s

Hard Bake on Hotplate: 115°C, 2 min

Flood Exposure (MA6 Mask Aligner): 15 s

Development (MF-300): ~40 sec

DI Water Rinse: 3 min

F.3) Cr etching

Dip in Cr Etchant for ~ 20 sec

DI Water Rinse: 3 min

F.3) Ti/Pt deposition (EnerJet Evaporator)

Thickness: 10/100 nm

F.4) Ti/Pt Lift –off

Soak in Aceton for 10 min

DI Water Rinse: 3 min

G.1) Photoresist Patterning

Photoresist: AZ 9260, ~8 μm

Spin: 500 rpm, 4 s + 3000 rpm, 30 s

Soft Bake on Hotplate: 110°C, 3 min 30 s

Cool Down in Ambient: >5 min

Exposure (MA6 Mask Aligner): 28 s

Development (AZ400: DI = 1:3): ~ 2 min

DI Water Rinse: 3 min

G.2) Backside DRIE – Defining Membrane

DRIE in STS ICP Machine: Recipe TYC-HR2,

Target depth: 170 μm, Etching time: ~120 min

G.3) Photoresist Removal

PRS-2000 Soak: >10 min

DI Water Rinse: 5 min

H.1) Backside DRIE – Defining Membrane

DRIE in STS ICP Machine: Recipe TYC-TH2,

Target depth: 200 μm, Etching time: ~50 min

H.2) EDP Wet Etching (Using Wafer Holder from www.ammt.com)

DI water: Catechol: Pyrazine: Ethylenediamene

= 432 mL: 432 g: 8.1 g: 1.35 L

Temperature: 110°C, Time: ~ 60 min

DI Water Rinse: 10 min @ 80°C

H.3) Wafer Dicing

Dicing with MA 1006 Dicing Saw: Blade 42525

REFERENCES

[1] D. L. DeVoe, "Thermal issues in MEMS and microscale systems," *IEEE Tranctions on Components and Packaging Technologies*, vol. 25, pp. 576-584, 2003.

[2] F. P. Incropera and D. P. Dewit, "Introduction to Heat Transfer," 4th ed, New York, Wiley, 2002

[3] M. A. Northrup, M. T. Ching, R. M. White, and R. T. Watson, "DNAamplification with a microfabricated reaction chamber," *in Proc. IEEE Int. Conf. Solid-State Sensors Actuators (Transducers'93)*, 1993, pp. 924–926.

[4] P. Belgrader, W. Benett, D. Hadley, G. Long, R. Mariella, F. Milanovich, S. Nasarabadi, W. Nelson, J. Richards, and P. Stratton, "Rapid pathogen detection using a microchip PCR array Instrument," *Clinical Chemistry*, vol. 44, pp. 2191-2194, 1998.

[5] L. C. Waters, S. C. Jacobson, N. Kroutchinina, J. Khandurina, R. S. Foote, and J. M. Ramsey, "Multiple sample PCR amplification and electrophoretic analysis on a microchip," *Analytical Chemistry*, vol. 70, pp. 5172-5176, 1998.

[6] Y. Huang, E. L. Mather, J. L. Bell, and M. Madou, "MEMS-based sample preparation for molecular diagnostics," *Analytical and Bioanalytical Chemistry*, vol. 372, pp. 49-65, 2002.

[7] T. Gorecki, J. Harynuk, and O. Panic, "The evolution of comprehensive two-dimensional gas chromatography (GC x GC)," *Journal of Separation Science*, vol. 27, pp. 359-379, 2004.

[8] B. H. Weigl and P. Yager, "Microfluidics - Microfluidic diffusion-based separation and detection," *Science*, vol. 283, pp. 346-347, 1999.

[9] N. T. Nguyen and Z. G. Wu, "Micromixers - a review," *Journal of Micromechanics and Microengineering*, vol. 15, pp. R1-R16, 2005.

[10] F. G. Bessoth, A. J. deMello, and A. Manz, "Microstructure for efficient continuous flow mixing," *Analytical Communications*, vol. 36, pp. 213-215, 1999.

[11] N. Schwesinger, T. Frank and H. Wurmus, "A modular microfluid system with an integrated micromixer," *Journal of Micromechanics and Microengineering*, , vol. 6, pp. 99–102, 1996

[12] J. Branebjerg, P. Gravesen, J. P. Krog and C. R. Nielsen, "Fast mixing by lamination," *MEMS '96, An Investigation of Micro Structures, Sensors, Actuators, Machines, and Systems*, San Diego, CA, USA, pp.11–15, 1996.

[13] U. D. Larsen, J. Branebjerg and G. Blankenstein, "Fast mixing by parallel multilayer lamination," *Proceedings of the 2nd International Symposium on Miniaturized Total Analysis Systems*, Basel, Switzerland, pp. 228-230, 1996.

[14] R. Miyake, T. S. J. Lammerink, M. Ewenspoek and J. H. J. Fluitman, "Micro mixer with fast diffusion," *MEMS '93, An Investigation of Micro Structures, Sensors, Actuators, Machines and Systems*, Fort Lauderdale, FL, USA, pp. 7–10, 1993.

[15] A. D. Stroock, S. K. W. Dertinger, A. Ajdari, I. Mezic, H. A. Stone, and G. M. Whitesides, "Chaotic mixer for microchannels," *Science,* vol. 295, pp. 647-651, 2002.

[16] R. H. Liu, M. A. Stremler, K. V. Sharp, M. G. Olsen, J. G. Santiago, R. J. Adrian, H. Aref, and D. J. Beebe, "Passive mixing in a three-dimensional serpentine microchannel," *Journal of Microelectromechanical Systems,* vol. 9, pp. 190-197, 2000.

[17] Y. K. Lee, J. Deval, P. Tabeling and C. M. Ho, "Chaotic mixing in electrokinetically and pressure driven micro flows," *The 14th IEEE Workshop on MEMS*, Interlaken, Switzerland, pp. 483-486, 2001.

[18] J. Fowler, H. Moon and C. J. Kim, "Enhancement of mixing by dropletbased microfluidics," *The 15th IEEE Workshop on MEMS*, Las Vegas, Nevada, USA, pp. 20–24, 2002.

[19] R. H. Liu, J. N. Yang, M. Z. Pindera, M. Athavale, and P. Grodzinski, "Bubble-induced acoustic micromixing," *Lab on a Chip,* vol. 2, pp. 151-157, 2002.

[20] M. H. Oddy, J. G. Santiago, and J. C. Mikkelsen, "Electrokinetic instability micromixing," *Analytical Chemistry,* vol. 73, pp. 5822-5832, 2001.

[21] A. P. Sudarsan and V. M. Ugaz, "Multivortex micromixing," *Proceedings of the National Academy of Sciences of the United States of America,* vol. 103, pp. 7228-7233, 2006.

[22] G. H. Seong and R. M. Crooks, "Efficient mixing and reactions within microfluidic channels using microbead-supported catalysts," *Journal of the American Chemical Society,* vol. 124, pp. 13360-13361, 2002.

[23] P. Mitchell, "Microfluidics - downsizing large-scale biology," *Nature Biotechnology,* vol. 19, pp. 717-721, 2001.

[24] J. W. Hong, V. Studer, G. Hang, W. F. Anderson, S. R. Quake, " A nanoliter-scale nucleic acid processor with parallel architecture," *Nature Biotechnology,* vol. 22, pp. 435-439, 2004.

[25] W. Gu, X. Y. Zhu, N. Futai, B. S. Cho, S. Takayama, "Computerized microfluidic cell culture using elastomeric channels and Braille displays," *Proceedings of the National Academy of Sciences of the United States of America*, vol. 101, pp.15861-15866, 2004.

[26] J. Liu, B. A. Williams, R. M. Gwirtz, B. J. Wold, S. Quake, " Enhanced Signals and Fast Nucleic Acid Hybridization By Microfluidic Chaotic Mixing," *Angewante Chemie International Edition*, vol. 45, pp. 3618-3623, 2006.

[27] T. Gorecki, J. Harynuk, and O. Panic, "The evolution of comprehensive two-dimensional gas chromatography (GC x GC)," *Journal of Separation Science,* vol. 27, pp. 359-379, 2004.

[28] J. Dalluge, J. Beens, and U. A. T. Brinkman, "Comprehensive two-dimensional gas chromatography: a powerful and versatile analytical tool," *Journal of Chromatography A,* vol. 1000, pp. 69-108, 2003.

[29] J.C. Giddings, "Two-dimensional separations: concept and promise," *Analytical Chemistry*, vol. 6, pp. 1258A–1270A, 1984.

[30] C. A. Bruckner, B. J. Prazen and R. E. Synovec, *Analytical Chemistry*, vol. 70, pp. 2796–2804, 1998.

[31] J. V. Seeley, F. Kramp and C. J. Hicks, *Analytical Chemistry*, vol. 72, pp. 4346–4352, 2000.

[32] Z. Y. Liu and J. B. Phillips, "Comprehensive 2-Dimensional Gas-Chromatography Using an on-Column Thermal Modulator Interface," *Journal of Chromatographic Science,* vol. 29, pp. 227-231, 1991.

[33] E. B. Ledford, J. B. Phillips, J. Z. Xu, R. B. Gaines, and J. Blomberg, "Ordered chromatograms: A powerful methodology in gas chromatography," *American Laboratory,* vol. 28, pp. 22, 1996.

[34] J. B. Phillips, R. B. Gaines, J. Blomberg, F. W. M. van der Wielen, J. M. Dimandja, V. Green, J. Granger, D. Patterson, L. Racovalis, H. J. de Geus, J. de Boer, P. Haglund, J. Lipsky, V. Sinha, and E. B. Ledford, "A robust thermal modulator for comprehensive two-dimensional gas chromatography," *Hrc-Journal of High Resolution Chromatography,* vol. 22, pp. 3-10, 1999.

[35] R. M. Kinghorn and P. J. Marriott, "Comprehensive two-dimensional gas chromatography using a modulating cryogenic trap," *Hrc-Journal of High Resolution Chromatography,* vol. 21, pp. 620-622, 1998.

[36] P. J. Marriott and R. M. Kinghorn, "Longitudinally modulated cryogenic system. A generally applicable approach to solute trapping and mobilization in gas chromatography," *Analytical Chemistry,* vol. 69, pp. 2582-2588, 1997.

[37] T. Hyotylainen, M. Kallio, K. Hartonen, M. Jussila, S. Palonen, and M. L. Riekkola, "Modulator design two-dimensional for comprehensive gas chromatography:

Quantitative analysis of polyaromatic hydrocarbons and polychlorinated biphenyls," *Analytical Chemistry,* vol. 74, pp. 4441-4446, 2002.

[38] E. B. Ledford and C. Billesbach, "Jet-cooled thermal modulator for comprehensive multidimensional gas chromatography," *Hrc-Journal of High Resolution Chromatography,* vol. 23, pp. 202-204, 2000.

[39] J. Beens, J. Dalluge, M. Adahchour, R. J. J. Vreuls, and U. A. T. Brinkman, "Moving cryogenic modulator for the comprehensive two-dimensional gas chromatography (GC x GC) of surface water contaminants," *Journal of Microcolumn Separations,* vol. 13, pp. 134-140, 2001.

[40] J. Beens, M. Adahchour, R. J. J. Vreuls, K. van Altena, and U. A. T. Brinkman, "Simple, non-moving modulation interface for comprehensive two-dimensional gas chromatography," *Journal of Chromatography A,* vol. 919, pp. 127-132, 2001.

[41] M. Libardoni, J. H. Waite and R. Sacks, "Electrically heated, air-cooled thermal modulator and at-column heating for comprehensive two-dimensional gas chromatography,"*Analytical Chemistry*, vol. 77, pp. 2786–2794, 2005.

[42] S. C. Terry, J. H. Jerman and J. B. Angell, "Gas-chromatographic air analyzer fabricated on a silicon-wafer," *IEEE Transactions on Electron Devices*, vol. 26, pp. 1880–1886, 1979.

[43] A. de Mello, "On-chip chromatography: the last twenty years," *Lab on a Chip*, vol. 2, 48N–54N, 2002.

[44] C.-J. Lu, W. H. Steinecker, W.-C. Tian, M. C. Oborny, J. M. Nichols, M. Agah, J. A. Potkay, H. K. L. Chan, J. Driscoll, R. D. Sacks, K. D. Wise, S. W. Pang and E. T. Zellers, "First-generation hybrid MEMS gas chromatograph," *Lab on a Chip*, vol 5, 1123–1131, 2005.

[45] P. R. Lewis, P. Manginell, D. R. Adkins, R. J. Kottenstette, D. R. Wheeler, S. S. Sokolowski, D. E. Trudell, J. E. Byrnes, M. Okandan, J. M. Bauer, R. G. Manley, C.

Frye-Mason, " Recent advancements in the gas-phase MicroChemLab," *IEEE Sensors Journal.*, vol 6, pp. 784–795, 2006.

[46] E. T. Zellers, S. M. Reidy, R. A. Veeneman, R. Gordenker, W. H. Steinecker, G. R. Lambertus, H. Kim, J. A. Potkay, M. P. Rowe, Q. Zhong, C. Avery, H. K. L. Chan, R. D. Sacks, K. Najafi, K. D. Wise, "An integrated micro-analytical system for complex vapor mixtures," in *Proceedings of the Transducers'07*, Lyon, France, June 10–15, 2007, pp. 10–14.

[47] S. Zampolli, I. Elmi, F. Mancarella, P. Betti, E. Dalcanale, G. C. Cardinali and M. Severi, "Real-time monitoring of sub-ppb concentrations of aromatic volatiles with a MEMS-enabled miniaturized gas-chromatograph," *Sensors and Actuators B*, vol. 141, pp. 322–328, 2009.

[48] G. Lambertus, A. Elstro, K. Sensenig, J. Potkay, M. Agah, S. Scheuering, K. Wise, F. Dorman and R. Sacks, " Design, Fabrication, and Evaluation of Microfabricated Columns for Gas Chromatography,"*Analytical Chemistry*, vol. 76, pp. 2629–2637, 2004.

[49] G. Serrano, S. M. Reidy, E. T. Zellers, "Assessing the reliability of wall-coated microfabricated gas chromatographic separation columns," *Sensors and Actuators B*, vol. 141, pp. 217–226, 2009.

[50] A. D. Radadia, R. I. Masel, M. A. Shannon, J. P. Jerrell and K. R. Cadwallader, " Micromachined GC Columns for Fast Separation of Organophosphonate and Organosulfur Compounds ," *Analytical Chemistry*, vol. 80, pp. 4087–4094, 2008.

[51] M. Agah, J. A. Potkay, G. Lambertus, R. Sacks and K.D. Wise, "High-performance temperature-programmed microfabricated gas chromatography columns," *Journal of Microelectromechcal Systems*, vol. 14, pp. 1039–1050, 2005.

[52] S. Reidy, G. Lambertus, J. Reece and R. Sacks, "High-Performance, Static-Coated Silicon Microfabricated Columns for Gas Chromatography," *Analytical Chemistry*, vol. 78, pp. 2623–2630, 2006.

[53] S. Reidy, D. George, M. Agah and R. Sacks, "Temperature-Programmed GC Using Silicon Microfabricated Columns with Integrated Heaters and Temperature Sensors," *Analytical Chemistry*, vol. 79, pp. 2911–2917, 2007.

[54] B. H. Bae, J. Yeom, A. D. Radadia, R. I. Masel, M. A. Shannon, "Fully-Integrated MEMS Preconcentrator for Rapid Gas Sampling "in *Proceedings of the Transducers'07*, Lyon, France, June 10–15, 2007, pp. 1497–1500.

[55] J. J. Whiting, C. S. Fix, J. M. Anderson, A. W. Staton, R. P. Manginell, D. R. Wheeler, E. B. Myers, M. L. Roukes, and R.J. Simonson, "High-speed two-diensional gas chromatography using microfabricated GC columns combined with nanoelectromechanical mass sensors," in *Proceedings of the Transducers'09*, Denver, USA, June 21–25, 2009, pp. 1666–1669.

[56] S. -J. Kim, F. Wang, M. A. Burns, and K. Kurabayashi, "Temperature-Programmed Natural Convection for Micromixing and Biochemical Reaction in a Single Microfluidic Chamber," *Analytical Chemistry,* vol. 81, pp. 4510-4516, 2010.

[57] A. Bejan, "Convection Heat Transfer," 2nd ed, New York, Wiley.

[58] J. Imberger, "Natural-Convection in a Shallow Cavity with Differentially Heated End Walls: 3. Experimental Results," *Journal of Fluid Mechanics,* vol. 65, pp. 247-260, 1974

[59] D. C. Duffy, J. C. McDonald, O. J. A. Schueller, and G. M. Whitesides, "Rapid prototyping of microfluidic systems in poly(dimethylsiloxane)," *Analytical Chemistry,* vol. 70, pp. 4974-4984, 1998.

[60] Y. S. Shin, K. Cho, S. H. Lim, S. Chung, S. J. Park, C. Chung, D. C. Han, and J. K. Chang, "PDMS-based micro PCR chip with parylene coating," *Journal of Micromechanics and Microengineering,* vol. 13, pp. 768-774, 2003.

[61] H. K. Wu, B. Huang, and R. N. Zare, "Construction of microfluidic chips using polydimethylsiloxane for adhesive bonding," *Lab on a Chip,* vol. 5, pp. 1393-1398, 2005.

[62] F. Wang, M. Yang, and M. A. Burns, "Microfabricated valveless devices for thermal bioreactions based on diffusion-limited evaporation," *Lab on a Chip,* vol. 8, pp. 88-97, 2008.

[63] W. N. Vreeland and L. E. Locascio, "Using bioinspired thermally triggered liposomes for high-efficiency mixing and reagent delivery in microfluidic devices," *Analytical Chemistry,* vol. 75, pp. 6906-6911, 2003.

[64] U. M. B. Marconi, A. Puglisi, L. Rondoni, and A. Vulpiani "Fluctuation-Dissipation: Response Theory in Statistical Physics," *Physics Reports*, vol. 461, pp. 111-195, 2008.

[65] D. E. Smith, T. T. Perkins, and S. Chu, "Dynamical Scaling of DNA Diffusion Coefficients," *Macromolecules*, vol. 29 , pp 1372–1373, 1996.

[66] M. Krishnan, V. M. Ugaz, and M. A. Burns, "PCR in a Rayleigh-Benard convection cell," *Science,* vol. 298, pp. 793-793, Oct 25 2002.

[67] E. K. Wheeler, W. Benett, P. Stratton, J. Richards, A. Chen, A. Christian, K. D. Ness, J. Ortega, L. G. Li, T. H. Weisgraber, K. Goodson, and F. Milanovich, "Convectively driven polymerase chain reaction thermal cycler," *Analytical Chemistry,* vol. 76, pp. 4011-4016, Jul 15 2004.

[68] N. Krishnan, N. Agrawal, M. A. Burns, and V. M. Ugaz, "Reactions and fluidics in miniaturized natural convection systems," *Analytical Chemistry,* vol. 76, pp. 6254-6265, Nov 1 2004.

[69] N. Agrawal, Y. A. Hassan, and V. M. Ugaz, "A pocket-sized convective PCR thermocycler," *Angewandte Chemie-International Edition,* vol. 46, pp. 4316-4319, 2007.

[70] D. Braun, N. L. Goddard, and A. Libchaber, "Exponential DNA replication by laminar convection," *Physical Review Letters,* vol. 91, pp. 158103, 2003.

[71] S. -J. Kim, Y. T. Lim, H. S. Yang, Y. B. Shin, K. Kim, D. S. Lee, S. H. Park, and Y. T. Kim, "Passive microfluidic control of two merging streams by capillarity and relative flow resistance," *Analytical Chemistry,* vol. 77, pp. 6494-6499, Oct 1 2005.

[72] J. den Toonder, F. Bos, D. Broer, L. Filippini, M. Gillies, J. de Goede, T. Mol, M. Reijme, W. Talen, H. Wilderbeek, V. Khatavkar, and P. Anderson, "Artificial cilia for active micro-fluidic mixing," *Lab on a Chip,* vol. 8, pp. 533-541, 2008.

[73] X. L. Li, H. L. Jin, Z. F. Wu, S. Rayner, and B. Wang, "A continuous process to extract plasmid DNA based on alkaline lysis," *Nature Protocols,* vol. 3, pp. 176-180, 2008.

[74] K. Kim, H. S. Yang, S. H. Park, D. S. Lee, S. J. Kim, Y. T. Lim, and Y. T. Kim, "Washing-free electrochemical DNA detection using double-stranded probes and competitive hybridization reaction," *Chemical Communications,* pp. 1466-1467, 2004.

[75] O. A. Turapov, G. V. Mukamolova, A. R. Bottrill, and M. K. Pangburn, "Digestion of native proteins for proteomics using a thermocycler," *Analytical Chemistry,* vol. 80, pp. 6093-6099, 2008.

[76] C. C. Lee, G. Sui, A. Elizarov, C. J. Shu, Y. S. Shin, A. N. Dooley, J. Huang, A. Daridon, P. Wyatt, D. Stout, H. C. Kolb, O. N. Witte, N. Satyamurthy,; J. R. Heath, M. E. Phelps, S. R. Quake, H. R. Tseng, "Multistep Synthesis of a Radiolabeled Imaging Probe Using Integrated Microfluidics," *Science*, vol. 310, pp. 1793-1796, 2005.

[77] M. A. Burns, B. N. Johnson, S. N. Brahmasandra, K. Handique, J. R. Webster, M. Krishnan, T. S. Sammarco, P. M. Man, D. Jones, D. Heldsinger, C. H. Mastrangelo, and D. T. Burke, "An integrated nanoliter DNA analysis device," *Science,* vol. 282, pp. 484-487, 1998.

[78] P. Belgrader, S. Young, B. Yuan, M. Primeau, L. A. Christel, F. Pourahmadi, and M. A. Northrup, "A battery-powered notebook thermal cycler for rapid multiplex real time PCR analysis," *Analytical Chemistry,* vol. 73, pp. 286-289, 2001.

[79] Y. J. Liu, C. B. Rauch, R. L. Stevens, R. Lenigk, J. N. Yang, D. B. Rhine, and P. Grodzinski, "DNA amplification and hybridization assays in integrated plastic monolithic devices," *Analytical Chemistry,* vol. 74, pp. 3063-3070, 2002.

[80] C. J. Easley, J. M. Karlinsey, and J. P. Landers, "On-chip pressure injection for integration of infrared-mediated DNA amplification with electrophoretic separation," *Lab on a Chip,* vol. 6, pp. 601-610, 2006.

[81] R. E. Murphy, M. R. Schure, and J. P. Foley, "Effect of sampling rate on resolution in comprehensive two-dimensional liquid chromatography," *Analytical Chemistry*, vol. 70, pp. 1585–1594,1998.

[82] M. Libardoni, J. H. Waite and R. Sacks, "Electrically heated, air-cooled thermal modulator and at-column heating for comprehensive two-Dimensional gas chromatography,"*Analytical Chemistry*, vol. 77, pp. 2786–2794, 2005.

[83] J. Membrillo-Hernandez, A. Nunez-de la Mora, T. del Rio-Albrechtsen, R. Camacho-Carranza and M. C. Gomez-Eichelmann, " Thermally-induced cell lysis in Escherichia coli K12," *Journal of Basic Microbiology*, vol. 35, pp. 41–46, 1995.

[84] D. S. Holmes and M. Quigley, "A rapid boiling method for the preparation of bacterial plasmids," *Analytical Biochemistry*, vol. 114, pp. 193–197, 1981.

[85] E. M. Southern, "Detection of specific sequences among DNA fragments separated by gel electrophoresis," *Journal of Molecular Biology*, vol. pp. 98, 503–517, 1975.

[86] J. T. Nevill, R. Cooper, M. Dueck, D. N. Breslauer and L. P. Lee, "Integrated microfluidic cell culture and lysis on a chip," *Lab on a Chip*, vol. 7, pp. 1689–1695, 2007.

[87] D. Di Carlo, K.-H. Jeong and L. P. Lee, "Reagentless mechanical cell lysis by nanoscale barbs in microchannels for sample preparation," *Lab on a Chip*, vol. 3, pp. 287–291, 2003.

[88] P. O. Brown and D. Botstein "Exploring the new world of the genome with DNA microarrays," *Nature Genetics*, vol. 21, pp. 33–37, 1999.

[89] K. Kim, H. S. Yang, S. H. Park, D. S. Lee, S.-J. Kim, Y. T. Lim, and Y. T. Kim, "Washing-free electrochemical DNA detection using double-stranded probes and competitive hybridization reaction," *Chemical Communications*, pp. 1466–1467, 2004.

[90] R. G. Sosnowski, E. Tu, W. F. Butler, J. P. O'Connell and M. J. Heller, “Rapid Determination of single base mismatch mutations in DNA hybrids by direct electric field

control ," *Proceedings of the National Academy of Sciences of the United States of America*, vol. 94, pp. 1119–1123, 1997.

[91] C. F. Edman, D. E. Raymond, D. J. Wu, E. Tu, R. G. Sosnowski, W. F. Butler, M. Nerenberg, and M. J. Heller, "Electric field directed nucleic acid hybridization on microchips," *Nucleic Acids Research*, vol. 25, pp. 4907–4914, 1997.

[92] Z. H. Fan, S. Mangru, R. Granzow, P. Heaney, W. Ho, Q. Dong, and R. Kumar, "Dynamic DNA hybridization on a chip using paramagnetic beads," *Analytical Chemistry*, vol. 71, pp. 4851–4859, 1999.

[93] R. H. Liu, R. Lenigk, R. L. Druyor-Sanchez, J. Yang, and P. Grodzinski, " Hybridization Enhancement Using Cavitation Microstreaming," *Analytical Chemistry*, vol. 75 , pp 1911–1917, 2003.

[94] B. J. Cheek, A. B. Steel, M. P. Torres, Y. Yu, H. Yang, "Chemiluminescence detection for hybridization assays on the flow-thru chip, a three-dimensional microchannel biochip," *Analytical Chemistry*, vol. 73, pp. 5777–5783, 2001.

[95] R.C.Y. Ong and P.J. Marriott, "A review of basic concepts in comprehensive two-dimensional gas chromatography," *Journal of Chromatographic Science*, vol. 40, 276–291, 2002.

[96] A. D. Radadia, R. D. Morgan, R. I. Masel, and M.A. Shannon, "Partially Buried Microcolumns for Micro Gas Analyzers, *Analytical Chemistry*, vol. 81, 3471–3477, 2009

[97] K. D. Wise, "Comprehensive Two-Dimensional Gas Chromatography (GCxGC) using Microfabricated Columns," Final project report on NASA Grant #NNG06GA89G, Feb 2010.